No major increase in erosion rates in Central Himalayas during the late Cenozoic, revealed by ^{10}Be in the newly dated Valmiki Siwalik section.

Authors:

Sebastien Jean Paul Lenard[1]*, Jérôme Lavé[1]**, Julien Charreau[1], Christian France-Lanord[1], Irene Schimmelpfennig[2], Ananta Gajurel[3], Rahul Kumar Kaushal[4], Florian Saillard[1†], Raphaël Pik[1], Guillaume Morin[1], Georges Aumaître[2], Karim Keddadouche[2], Zaidi Fawzi[2], Laetitia Leanni[2]

Affiliations:

[1]Université de Lorraine, CNRS, CRPG, F-54000 Nancy

[2]Université Aix-Marseille, CNRS-IRD-Collège de France, UM 34 CEREGE, Technopôle de l'Environnement Arbois-Méditerranée, Aix-en-Provence, France

[3]Department of Geology, Tribhuvan University, Kathmandu, Nepal

[4]Indian Institute of Technology Gandhinagar (IITGN), Gandhinagar, Gujarat, 382355, India

Correspondence to:

*sebastien.lenard@gmail.com

**jlave@crpg.cnrs-nancy.fr

[†]deceased

Abstract

The Glaciations impacted erosion during the Late Cenozoic but no consensus has emerged whether they led to increased erosion rates globally. In the Himalayas, recent work used past sediment concentrations of the terrestrial cosmogenic nuclide (TCN) ^{10}Be and demonstrated that erosion rates have not permanently increased in the Himalayas. However, for the Quaternary, the published sedimentary records suffer from provenance uncertainties which prevent to elaborate on the causes of steady erosion rates. Here, we document the new, 4,000-m thick Valmiki Section (VS) to address this question. In the remote Valmiki Tiger Reserve, the VS consists of Siwalik sediment deposited in the Himalayan foreland basin by the Narayani River, a major river of Central Himalayas. To quantify past Himalayan erosion rates from TCN ^{10}Be measurements, we determine: (1) the magnetostratigraphic deposition age model, (2) provenance using major elements and Sr-Nd isotopes, and (3) the recent cosmic exposure related to Siwalik exhumation using TCN ^{36}Cl measurement in feldspar. The VS records Himalayan erosion from 7.5 to 1.25 Ma. Our ^{10}Be results confirm steady erosion rates, close to modern values, 1.4-2.3 mm/y, with a brief increase by 35% at 2 Ma, possibly due to sustained glacial erosion of the high peaks as suggested by the geochemical signature. The Narayani Catchment may be more sensitive to the onset of the Glaciations because of larger glacial cover (presently ~10%) than elsewhere in the Himalayas. Despite this sensitivity, our results support that over long timescales, rather than climate, tectonics control Himalayan erosion.

1. Introduction.

Climate evolves globally and considerably throughout the late Cenozoic. With a start at any location on Earth during the Middle Cenozoic (10-20 Ma), temperatures gradually drop to the point that ice sheets grew in the Northern Hemisphere at 2.6 Ma, with intense glaciations after 0.8 Ma (Lisiecki and Raymo, 2005; Cramer et al., 2011; Herbert et al., 2016). Precipitation also substantially evolves. In Asia and elsewhere, the overall amount of precipitation decreases, with increasingly contrasted wet and dry seasons (Quade et al., 1989; Caves Rugenstein and Chamberlain, 2018). Concurrently with the onset of the Quaternary and glacial-interglacial cycles at ca. 2.6 Ma, climate becomes unstable in the Northern Hemisphere and oscillates between cold and warm stages (Cerling et al., 1997; Edwards et al., 2010).

Researchers conjectured a global increase in erosion rates during the late Cenozoic, after 10 Ma, using compiled sedimentary budgets and in-situ thermochronology (Zhang et al., 2001; Herman et al., 2013) – in this study, we use erosion as a synonym of denudation. They proposed that such an increase was substantial in mid-latitude mountain ranges and they related this possible increase to a larger extent of areas subject to glacial and periglacial erosion, or to some processes increasing erosion rates when

glacial/interglacial climatic conditions rapidly alternate (Molnar, 2004). But so far, no consensus has emerged. The amplitude or even the existence of a global increase in erosion rates remains debated. Distinct approaches led to opposite conclusions (Schumer and Jerolmack, 2009; Willenbring and von Blanckenburg, 2010; Herman et al., 2013). The Himalayas are an emblematic orogen and a major contributor to terrestrial sediment fluxes (Milliman and Farnsworth, 2011). Unraveling how erosion rates evolve in the Himalayas during the Late Cenozoic brings insight to the controversy.

As for the global scale, published work on the erosion rate evolution in the Himalayas during the Late Cenozoic remains disputed whatever the methodological approach. At the scale of the mountain range, sedimentation rates yield opposite conclusions. (Métivier et al., 1999) compiled 1-D drilled core logs and seismic data in the deposits of the Bengal Fan and the Indus Fan and concluded that sediment accumulation rates increased by a factor five to ten. On the opposite, (Clift, 2006) compiled seismic data in the South China Sea and in the Indus Fan, and reported sedimentation rates during the Quaternary similar to or lower than Miocene rates. In-situ thermochronology using multiple chronometers points to similarly conflicting interpretations in Central Himalayas – the central part of the E-W oriented Himalayan arc, by opposition to the western and eastern parts. Locally in the geographic High Himalayas, the region where relief is the highest, studies infer an increase in erosion rates by a factor two to five since 4 Ma (Huntington et al., 2006; Blythe et al., 2007; Herman et al., 2013). But at the scale of Central Himalayas, 1-D and 3-D inversions of thermochronologic data (Thiede and Ehlers, 2013; Herman et al., 2010) suggest steady erosion rates since 10 Ma. Contrastingly, thermochronology suggests a different evolution of erosion rates outside of Central Himalayas, with a decrease in erosion rates in Bhutanese Himalayas (Thiede and Ehlers, 2013; Adams et al., 2015).

Researchers also applied detrital thermochronology on ancient Himalayan sediment in the Siwalik Hills at the front of the Himalayas (van der Beek et al., 2006; Bernet et al., 2006) and in the Bengal Fan in the Indian Ocean (Harrison et al., 1993; Huyghe et al., 2021). Their results point to steady erosion rates since the Middle Miocene, either averaged at the catchment scale in Central Himalayas or at the scale of Central and East Himalayas, respectively. But detrital thermochronology averages erosion rates over timescales of several million years, with smoothing and offsetting of rapid changes. Problematically, the sediment collected in these studies at the front of the Himalayas did not record the Quaternary erosion of the High Himalayas, because of sediment provenance shifts at 3 Ma (Charreau et al., 2021).

An alternative, independent approach to reconstruct the evolution of erosion rates is to determine catchment-averaged paleoerosion rates from in-situ ^{10}Be terrestrial cosmogenic nuclide (TCN) concentrations in the quartz fraction of ancient river sediment sand (Charreau et al., 2011; Puchol et al., 2017; Mandal et al., 2021). TCN in modern river sand average erosion rates across the contributing

catchment area (Brown et al., 1995). When measured in ancient sediment, TCN similarly allow determining the averaged past erosion rates of the contributing catchment at deposition time, called paleoerosion rates (Charreau et al., 2011; Puchol et al., 2017; Schaller et al., 2002). This approach averages erosion rates over ~1 ka timescales for the High Himalayas, much shorter than thermochronology.

We previously applied this approach on the turbidites of the distal archives of the Middle Bengal Fan (Lenard et al., 2020). The ^{10}Be paleoconcentrations from that work are steady on average and are incompatible with a permanent increase in erosion rates in the Himalayas since 6 Ma. However, major variations of sediment provenance affect that distal record, as shown by the Sr and Nd isotopic signature of sediment which fluctuates between the western (Ganga Catchment) and eastern (Brahmaputra Catchment) parts of the contributing catchment. The variations reflect tectonic variations in the Brahmaputra Catchment (Najman et al., 2016) or variable mixing of sediment from the Ganga and Brahmaputra Rivers within the submarine fan (Lenard et al., 2020). Provenance fluctuations make it difficult to interpret the lack of response of the Himalayan erosion to the late Cenozoic global climatic change. Studying more proximal records, along the Himalayan frontal range, will help confirm or infirm this stability of erosion rates during the late Cenozoic.

We also previously applied the TCN approach at the front of the Himalayas. We collected molasses of the proximal archives of the Surai Section in the Siwaliks, in the western part of Central Himalayas (Charreau et al., 2021) (Fig. 1). The ^{10}Be paleoconcentrations from that work, averaged at Himalayan catchment-scale, are similar for the Pliocene to modern river sand concentrations. However, sediment provenance shifts from the Karnali Catchment draining the High Himalayas, to a local, frontal catchment, at 3 Ma. Other researchers also applied this approach in the Yamuna Section in West Himalayas but observe a similar shift of provenance (Mandal et al., 2021). Provenance shifts observed in the published sections at the Himalayan front prevent reconstructing the evolution of erosion rates during the Quaternary, the period of intense climatic changes.

In this study, we overcome the limitations of the Surai Section and the Yamuna Section. We document a new, 4,000-m-thick sedimentary section at the front of the Himalayas to reconstruct the paleoerosion rates of the High Himalayas over the late Cenozoic throughout the Quaternary. We name this section the Valmiki Section. The Valmiki Section extends across the frontal Himalayan relief of the Siwalik Hills in the north Bihar region of India, south of Central Nepal. It gives access to the erosion products of Central Himalayas (Fig. 1). We present this work in the following way. After introducing the Himalayan and Valmiki setting (§ 2.), we describe the methodological approach (§ 3.) and consider the corrective terms for calculating paleoerosion rates (§ 3.6-8.). We describe this new, formerly

undocumented, section (§ 4.1.) and present our magnetostratigraphic dating results (§ 4.2.). We determine the depositional setting, weathering, and sediment provenance using our sedimentologic observations and our measurements of major elements and Sr-Nd isotopes on regularly-spaced samples (§ 4.3.). We present our TCN ^{10}Be concentration results obtained on the same samples (§ 4.4.1.). We reconstruct the paleoerosion rates of the Narayani Catchment (Central Nepal) (§ 4.4.4.). For this step, we determine exposure to cosmic rays during floodplain transfer using a published sediment floodplain transport model (§ 4.4.2.). We also determine recent exposure due to Siwalik exhumation using a new simple model of valley incision that we validate by our ^{36}Cl measurement on feldspar (§ 4.4.3.). Finally, we discuss (§ 5.) the contribution of our new paleoerosion rate results to understand the response of the Himalayas to the late Cenozoic and Quaternary climatic changes.

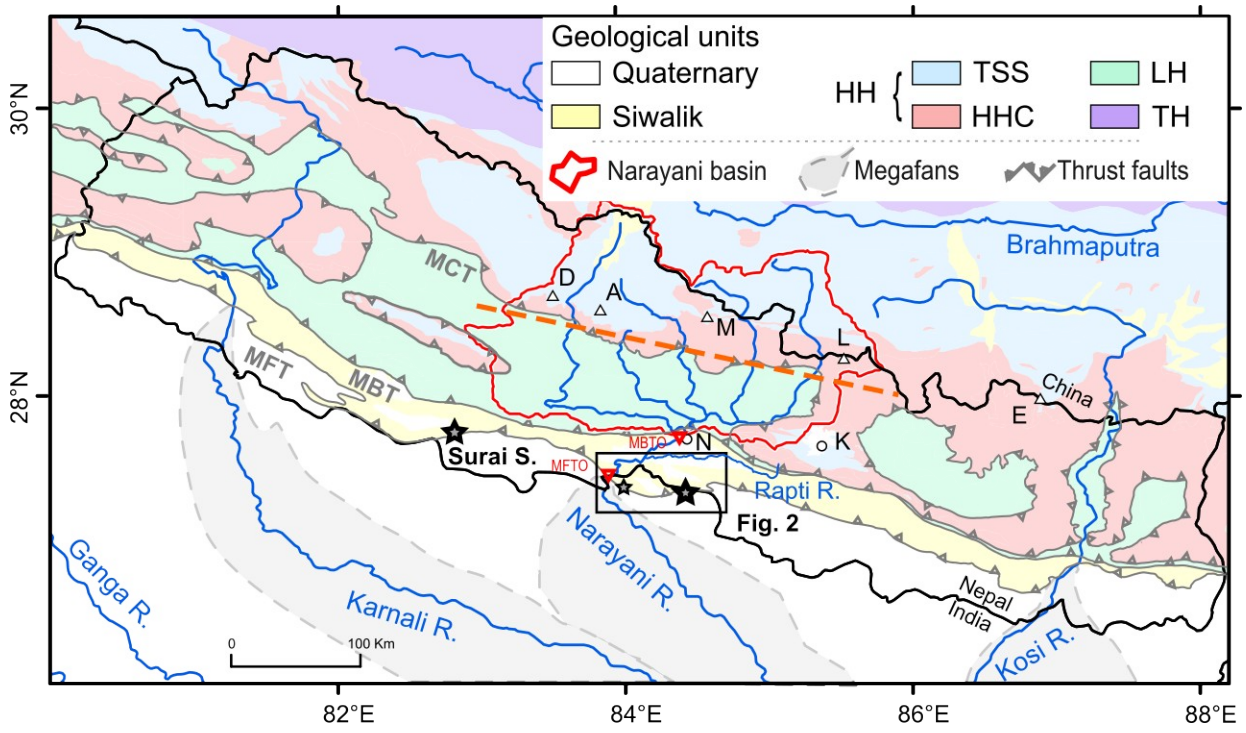

Fig. 1. Map of Nepal in the Central Himalayas. *Geology.* Main Himalayan geological units (Colchen et al., 1986): Quaternary: Ganga plain, Siwalik: folded Cenozoic deposits, LH: Lesser Himalaya, HHC: High Himalayan Crystalline, TSS: Tethyan Sedimentary Series. The High Himalayas (HH) groups the HHC and the TSS, which are intruded by granitic plutons such as the Manaslu. Major Himalayan thrusts: MFT = Main Frontal Thrust, MBT = Main Boundary Thrust, and MCT = Main Central Thrust. *Geomorphology.* The Karnali River, the Narayani River with its red-contoured drainage basin, and the Kosi River drain the Himalayas in Nepal. These rivers

transport huge amounts of sediments out of the range and build large alluvial fans or megafans in the Ganga plain. Red triangles point down indicate the Narayani MBT outlet (MBTO), at Narayangarh (N), and the Narayani MFT outlet (MFTO), which corresponds to the present apex of the Narayani megafan. Smaller, local rivers such as the Rapti River drain the Siwaliks. Geographically, the southern Himalayan flank is south of the highest peaks, such as A: Annapurnas Mt, D: Daulaghiri Mt, E: Everest Mt, K: Kathmandu; L: Langtang Mt, M: Manaslu Mt. These high peaks form the geographical High Himalayas (HH), with much higher relief than the geographic Lesser Himalayas (LH), south of the orange-colored dashed line. Note that the lithological HH is also present in tectonic windows within the geographic LH. The study area (black-outlined rectangle) is located in the Siwalik hills at the front of the range, in the axis of the Narayani Megafan. Location of the section studied by (Charreau et al., 2021) indicated by Surai S.: Surai Section. Geological map compiled by the Department of Mines and Geology of Nepal (Kathmandu, 1994).

2. Central Himalayas and sampling site setting.

After introducing the Central Himalayas (§ 2.1.), we briefly present the Siwaliks (§ 2.2.) and the site of the new Section (§ 2.3.).

The new Valmiki Section extends north-south in the Valmiki Wildlife Sanctuary (north Bihar region of India), south of the Chitwan Dun (Fig. 1-2). It forms an almost continuous series of molasses thick of ~4,000 m extending back to the late Miocene, as shown by our magnetostraphic study (§ 4.2.). The section lies south of the present-day catchment of the Narayani River, which drains the entire Himalayan wedge from South Tibet to the Siwaliks. We expect that the Valmiki sedimentary archives recorded the paleoerosion of the lithologic units outcropping in the Narayani Catchment.

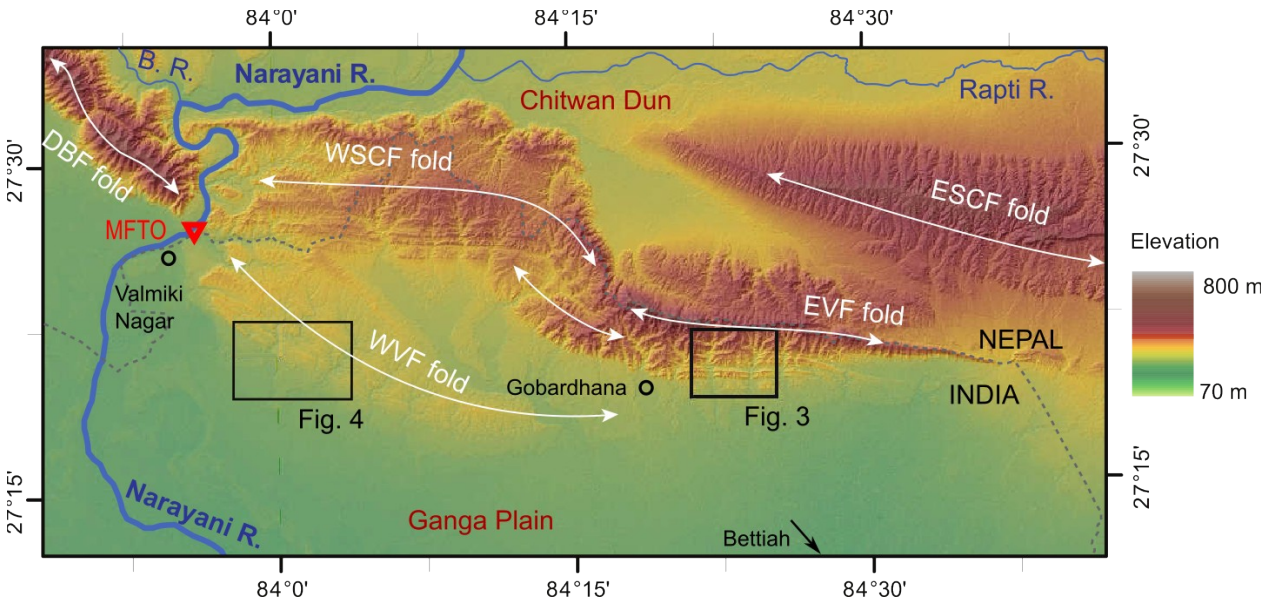

Fig. 2. Topographic map of the Outer Siwalik Hills south of the Chitwan Dun in Central Nepal. The South Chitwan presents en-echelon folds which are uncommon in the Outer Siwaliks. As the folds have grown during the Quaternary, they have diverted the main Himalayan Narayani River and the local Rapti River to the West. The Narayani River is presently pinned across the MFT at the junction between the South Chitwan en-echelon folds, south of the Rapti River, and the Dumkibas single frontal fold (DBF fold), south of the Binai River (B. R.). South of Chitwan Dun, deformation is divided in two sets of structures. (1) The two most frontal structures, the Valmiki Folds, are separated into the West Valmiki Fold (WVF) and the East Valmiki Fold (EVF) (called Valmiki Nagar Range and Southwest Churia Range in (Divyardashini and Singh, 2019)). The sections presented in this study are located along the southern flanks of these two folds. (2) The northern structures, the South Chitwan Folds, are separated into the West South Chitwan Fold (WSCF) and the East South Chitwan Fold (ESCF) (called Southwest Churia Range and Southeast Churia Range in (Divyardashini and Singh, 2019)). MFT Outlet indicated by triangle point down (MFTO).

2.1. Central Himalayas and Narayani Catchment geologic and geomorphologic setting.

The Himalayan Arc in Nepal divides in four main east-west trending geological units (Colchen et al., 1986), from north to south: (1) the Tethyan Sedimentary Series or TSS, grouping medium to low-grade detrital and carbonate metasediment of Paleozoic to Eocene age; (2) the High Himalayan Crystalline

or HHC, consisting of high-grade metamorphic gneisses and migmatites, with Miocene leucogranites intruding both the TSS and the HHC; (3) the Lesser Himalayas or LH, grouping metamorphosed Precambrian to Palaeozoic metasediment from the Indian craton; (4) the Siwaliks, consisting of Neogene sediment deposited in the foreland Himalayan basin of the Ganga Plain and exhumed during the Late Cenozoic by thin skin tectonics. In this study, we group the TSS and the HHC into a lithologic group called High Himalayas (HH), which overlap the geographic High Himalayas, the Himalayan region with the highest summits. Similarly, the LH lithologic unit overlaps the geographic Lesser Himalayas, the region of lower relief south of the geographic HH. Two major thrusts bound the Siwaliks: the Main Boundary Thrust (MBT) which overthrusted LH on top of the Siwaliks, and the Main Frontal Thrust (MFT), which is the most frontal thrust of the range yielding to the southernmost frontal topographic expression of the Himalayan wedge north of the Ganga Plain. The Siwaliks outcrop in Central Himalayas along up to four topographic folds belts called the Siwalik Hills, separated by internal thrusts faults (Fig. 1-2).

The Narayani River is a major Himalayan river and drains the Himalayas in Central Nepal, over a catchment extending 210 km from east to west (Fig. 1). The four main tributaries of the Narayani River source from South Tibet and drain southward across the four main geologic units. Presently, the TSS, HHC and LH occupy 34%, 24% and 42% of the surface of the Narayani Catchment at the MBT-outlet (MBTO on Fig. 1), respectively. South of this outlet, the Narayani River flows through the piggy-back sedimentary basin of the Chitwan Dun. The frontal Siwalik belt deflects the Narayani River westward over a distance of 40 km west of Narayangarh before the river crosses the MFT (MFTO on Fig. 1). In the Chitwan Basin, the Narayani River collects sediment from the Rapti River, a minor tributary draining a 100-km east-west long segment of the Siwalik belts. Downstream of the MFT in India, the Narayani River is named the Gandak River and flows southeastward through the Ganga Plain, via a braided channel evolving into a meandering channel. The Narayani River deposits sediment over 230 km in the Narayani Fan, an alluvial megafan of a gentle slope, and then merges with the Ganga River (Sinha and Friend, 1994).

The Narayani Catchment receives intense monsoon precipitation, 1,500 mm/y on average, locally up to 5,000 mm/y along the southern flank of the High Himalayas (Putkonen, 2004; Andermann et al., 2011). Intense precipitation combined with high relief and steep slopes favor high erosion rates driven by landsliding (Gabet et al., 2004; Gallo and Lavé, 2014; Morin et al., 2018; Marc et al., 2019) and river incision (Lavé and Avouac, 2001). Present erosion rates display marked contrasts from north to south across Central Himalayas. These contrasts are consistent with the long-term erosion rates derived from in-situ thermochronology. North in semi-arid South Tibet, erosion rates are below 0.2-0.4 mm/y (Gabet et al.,

2008). Southward across the HHC, the erosion rates reach a first maximum at 2-5 mm/y (Burbank et al., 2003; Huntington et al., 2006; Blythe et al., 2007; Whipp et al., 2007; Lavé and Avouac, 2001; Garzanti et al., 2007; Godard et al., 2012) and drop below 0.5 mm/y in the LH (Herman et al., 2010; Robert et al., 2009; Wobus et al., 2005; Andermann et al., 2012; Godard et al., 2012, 2014). At the Himalayan front in the Siwaliks Hills north of the Ganga Plain, high uplift rates combined to erodible material induce a second peak of erosion rates, up to 10-15 mm/y (Lavé and Avouac, 2000).

Due to the erosive conditions of its catchment, the Narayani River is the largest contributor of sediment to the Ganga River. Modern sediment fluxes yield a mean annual sediment supply of 135 Mt/y, which corresponds to catchment-averaged present erosion rates of 1.6 (-0.2/+0.35) mm/y (Andermann et al., 2012; Morin et al., 2018). The TCN ^{10}Be concentrations in the sandy quartz fraction of the Narayani River sediment correspond to consistent millennial erosion rates of 1.8 (±0.4) mm/y (Lupker et al., 2012a). Compared to elsewhere in the Himalayas, the ^{10}Be concentrations of the Narayani sediment display relative stability (less than 40% dispersion) over a 6-year period with an average value of ~$10x10^3$ at/g (Lupker et al., 2012a).

2.2. The Siwaliks of Central Himalayas.

Active folding exposes the Siwalik sedimentary series in the Siwalik Hills (Lavé and Avouac, 2000). Their fold belts orient WNW-ESE, with an elevation below 1,000 m. The Siwalik series consist in a 3 to 6 km thick pile of molasses deposited during the Neogene and produced by several million years of intense erosion in the geographic High Himalayas (Herail and Mascle, 1980).

The Siwaliks present fluvial facies and a deposition setting similar to the modern Indian foreland basin (Jain and Sinha, 2003; Dubille and Lavé, 2015). In the Ganga Plain at the Himalayan front, sediment deposited on a series of large alluvial megafans associated to transverse Himalayan rivers that drain the Himalayas from the high elevated Tibet to the lowland piedmont (Fig. 1) (DeCelles et al., 1998; Gupta, 1997). These megafans alternate with interfan areas which sediment was deposited by local rivers sourcing from the Mahabarat or the Siwaliks (Fig. 1). The Siwalik sediment alternates layers of mud- and clay-stone, fine-grained to coarse sandstone and conglomerates deposited by gravely braided rivers. Grain size coarsens upward, because of the gradual southward migration of the Himalayan thrust wedge and depositional facies (Lyon-Caen and Molnar, 1985; DeCelles et al., 1998; Dubille and Lavé, 2015). The Siwalik series are continental and have limited biostratigraphic constraints. Since the 1980s, magnetostratigraphic studies have constrained depositional ages, especially in Nepal (Appel et al., 1991; Harrison et al., 1993). Some sedimentary sections date back to ca. 15 Ma (Gautam and Fujiwara, 2000). Few sections cover the full period from the Middle or Late Miocene to the Quaternary. The Surai Section (Appel et al., 1991; Ojha et al., 2009), and, in a more dispersed pattern, the Arung-Binai Section west of

the Narayani MFT-outlet, are the main sections which have sediment records dated from the Quaternary (Tokuoka et al., l986).

2.3. The sampled Valmiki sections.

The study area in the Siwaliks has remained almost unexplored and geologically undescribed so far. The Siwalik frontal folds are south of the Chitwan Dun piggy-back basin (Fig. 2). They extend over two Wildlife Sanctuaries with an extensive preserved forest cover, the Chitwan National Park in Nepal and the Valmiki National Park in India. No road or river entirely crosses these folds from south to north. The area consists of Siwalik sediment deposited in the late Cenozoic and folded in a series of en-echelon folds with low relief (white double-arrows, Fig. 2). We identify the West South Chitwan Fold and the East South Chitwan Fold (WSCF and ESCF) in the north, and the West and East Valmiki frontal Folds (WVF and EVF) in the south, all located in the hanging wall of the MFT. Elevation is low, 250-700 m. In particular, the WVF displays minimal elevations (more than 100 m) above the surrounding plains. We investigated and sampled the southern limb of the EVF in India, ~40 km east of the MFTO (Fig. 2-3), in Fall 2012 and Spring 2016. We carried out a complementary study, involving discrete sampling, along the southern limb of the WVF in India (Fig. 2, 4), in Fall 2011 and Spring 2017. The section across the EVF, referred to "the Section" or “the Valmiki Section”, is actually composed of three segments of subsections (Fig. 3).

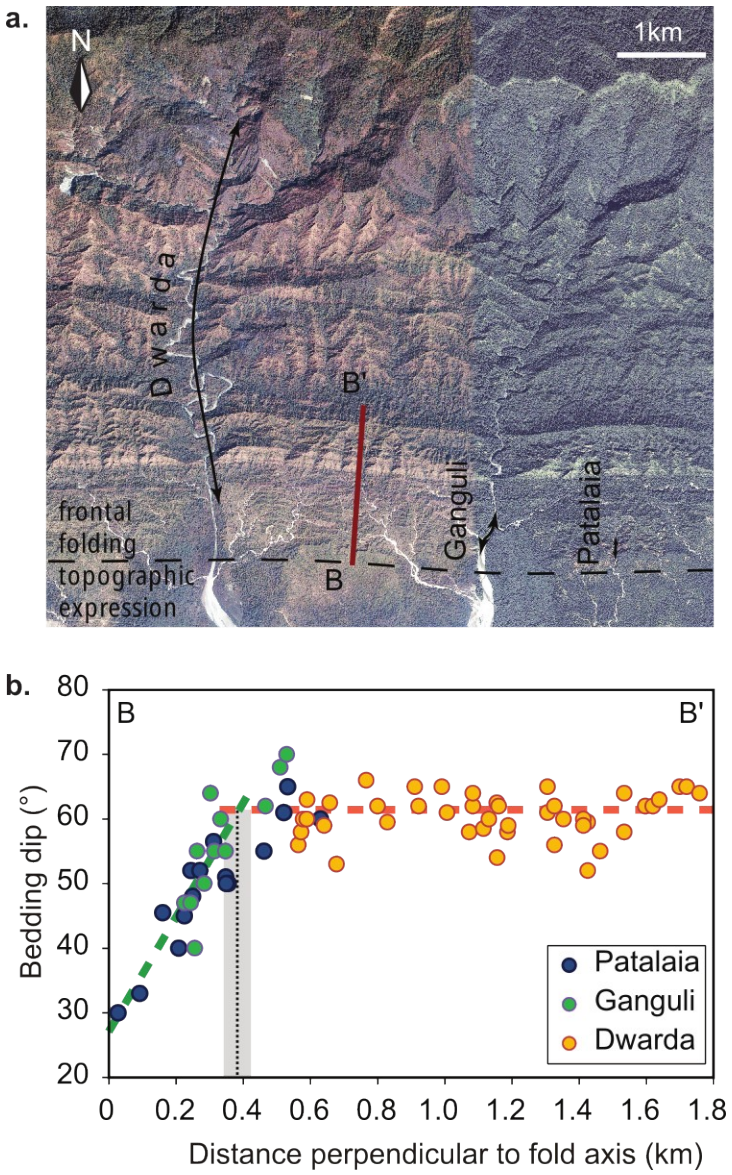

Fig. 3. Composite East Valmiki Section (EVF). Location in the South Chitwan in Fig. 2. **a.** Surveys along the southern flank of the fold, realized following the Dwarda, Ganguli and Patalaia valleys. Background satellite image from Google Earth©. **b.** Projection of the dip measurements for the three sections on the BB' transect (location indicated in a.). The fold presents a monotonous homoclinal structure with west-east bedding attitude, and dip angle around 60°. Dip values decrease southward at the frontal part. We interpret this as the signature of syn-folding sedimentation.

The Section and more generally the study area were selected for several reasons that enable the reconstruction of Late Cenozoic erosion of the Himalayas from the analysis of TCN in past sediment:

(1) The Section is in the axis of an alluvial megafan (grey shading in Fig. 1), and not in the interfan zone as the Surai Section (Charreau et al., 2021). Sediment in the section presumably originates from the Narayani Catchment, and shall reflect the erosion of a catchment covering the complete north-to-south extent of the Himalayas, including the High Himalayas, and not only a local catchment in the southern tip of the Himalayas, draining the Lesser Himalayas (LH) or the Siwaliks (geological units Fig. 1).

(2) This catchment drains an area where major elements, Sr-Nd isotopic composition and erosion rates have been documented more comprehensively than anywhere in the Himalayas. Thermochronology has constrained erosion rates in several areas of the catchment and has suggested an increase in erosion rates over the last few million years (Huntington et al., 2006; Blythe et al., 2007).

(3) The frontal Siwalik folds south of the Chitwan Dun (Fig. 2) appear less mature, and probably developed later than elsewhere along the Central Himalayas. Therefore, sediment deposition in the Section probably lasted until late Quaternary, before folds grew.

(4) The frontal Siwalik folds developed 30 km south of the main topographic front, that is the MBT, (Fig. 1-2), at a distance greater than the gravel-sand transition, usually at 10-20 km south of the Himalayan front in Central Nepal (Dubille and Lavé, 2015; Dingle et al., 2017). Consequently, the Section should be richer in fine-grain sediment suitable for magnetostratigraphic dating especially during the Quaternary, while this approach is difficult in other sections, in which conglomerates become dominant for that period (Charreau et al., 2021).

3. Methods.

After synthesizing our approach (§ 3.1.) applied on the sampling sites (§ 3.2.), we develop methods for magnetostratigraphic dating (§ 3.3.) and provenance tracing (§ 3.4.). Then, we present methods to reconstruct the Himalayan paleoerosion rate record (§ 3.8.), with TCN ^{10}Be measurement (§ 3.5.), and corrections for plain exposure (§ 3.6.) and for recent Siwalik exhumation obtained with ^{36}Cl measurement on felspar (§ 3.7.). We provide Extended Methods in Supplementary Information.

3.1. Determining paleoerosion rates from in-situ ^{10}Be cosmogenic nuclide analyses: an overview.

Published work amply describes the approach to determine paleoerosion rates from ^{10}Be cosmogenic concentrations in the quartz fraction of past sedimentary archives (Charreau et al., 2011; Amidon et al., 2017; Puchol et al., 2017; Charreau et al., 2021, Mandal et al., 2021).

The sedimentary archives of the Valmiki Section originate from Himalayan rocks in which terrestrial cosmogenic nuclides (TCN, e.g. ^{10}Be and ^{36}Cl) are produced by collision of cosmic rays with atoms of rock minerals during erosion near surface. The river network rapidly conveys erosion products through the Himalayas. At the range outlet, the TCN ^{10}Be content of sediment reflects erosion rates averaged over the contributing catchment (Brown et al., 1995). Farther downstream, rivers transport sediment through the Ganga Plain before sequestration and deep burial. During this fluvial transport, sediment is partly exposed to cosmic rays and accumulates an additional dose of cosmogenic nuclides. After sediment burial and until today, radioactive decay affects this initial TCN content within sediment. During the final stage of the recent Siwalik exhumation caused by thin skin tectonics, sediment accumulates a last dose of TCN when reaching the surface. Measuring present ^{10}Be content in the quartz fraction of Siwalik sediment allows to trace paleoerosion rates of the Himalayas, as expressed by:

$$^{10}C = e^{-\lambda t}\left[\sum_{j=1,2,3}\frac{\Lambda_j \bar{P}_j}{\bar{\varepsilon}\,\rho_r} + {}^{10}C_{fp}\right] + {}^{10}C_{rex} \qquad \text{(Eq. 1a)}$$

$$\text{that is } \bar{\varepsilon} = \frac{1}{\rho_r}\cdot\frac{\sum_{j=1,2,3}\Lambda_j \bar{P}_j}{\left[{}^{10}C - {}^{10}C_{rex}\right]e^{\lambda t} - {}^{10}C_{fp}} \qquad \text{(Eq. 1b)}$$

The $\bar{\varepsilon}$ is the Himalayan paleoerosion rate averaged across the catchment (red-outlined, Fig. 1); ^{10}C is the present ^{10}Be concentration (atom/g of quartz) measured in Siwalik sandstone; $\bar{P}_j$ is the overall paleoproduction rate averaged over the catchment at the time of erosion and accounts for each cosmogenic production pathways (spallation, slow and fast muon capture); ρ_r is the density of the eroded rocks; λ is the radioactive decay constant of ^{10}Be; Λ_j is the attenuation length of each production pathway (g/cm^2); *t is* the time during which sediments was buried, that is the depositional age); $^{10}C_{fp}$ is the concentration (atom/g of quartz) of cosmogenic nuclides accumulated by sediment during transport and final deposition in the Ganga Plain, that is until buried deep enough to be fully shielded from cosmic rays; and $^{10}C_{rex}$ is the concentration accumaluted during their recent exhumation before their sampling on the outcrop.

Determining the paleoerosion rate from the present ^{10}Be concentration, ^{10}C, in the Siwalik rocks (§ 3.4.), and according to (Eq. 1b) requires to measure four parameters, t, $\bar{P}_j$, $^{10}C_{fp}$, $^{10}C_{rex}$:

- t, by carrying out magnetostratigraphy to construct an age model for the Section (§ 3.2.),

- $\bar{P}_j$, by assuming the past catchment average production rates similar to modern ones that are calculated based on the modern elevation of the catchment using the Basinga tool box (Charreau et al., 2019). To validate this hypothesis, we carried out major element and Sr-Nd isotopic analyses on bulk sediment to trace provenance from the main Himalayan lithologic units (§ 3.3.),

- $^{10}C_{fp,}$ by carrying out observations on the stratigraphic positions of samples to assess ^{10}Be contribution during sediment transfer using (Lauer and Willenbring, 2010)'s model (§ 3.5.),

- $^{10}C_{rex,}$ by assuming an average Siwalik fold exhumation rate, with a validation by ^{36}Cl measurements in feldspar of the TCN-analyzed samples (§ 3.6.).

After accounting for the corrective terms, which are the contribution during transfer in the floodplain, radioactive decay and the contribution during recent exhumation, we compute ^{10}Be initial paleoconcentrations and then paleoerosion rates (§ 3.7).

3.2. Sampled sections.

We carried out sampling along the Dwarda, the Ganguli and the Patalaia Rivers, to construct the EVF Section, located East of Gobardhana village (Fig. 3). We additionally collected a few Pleistocene sediment samples along the Maloni Naha and the Gonauli Rivers, in the southern limb of the young WVF (Fig. 2), close to the current Narayani MFT outlet (MFTO). We measured the bedding dip attitudes (Fig. 4a) and we used satellite imagery (Google Earth©) to define the structures and laterally correlate the stratigraphy between the studied sections and sites (all field observations on the sections detailed in § 4.1).

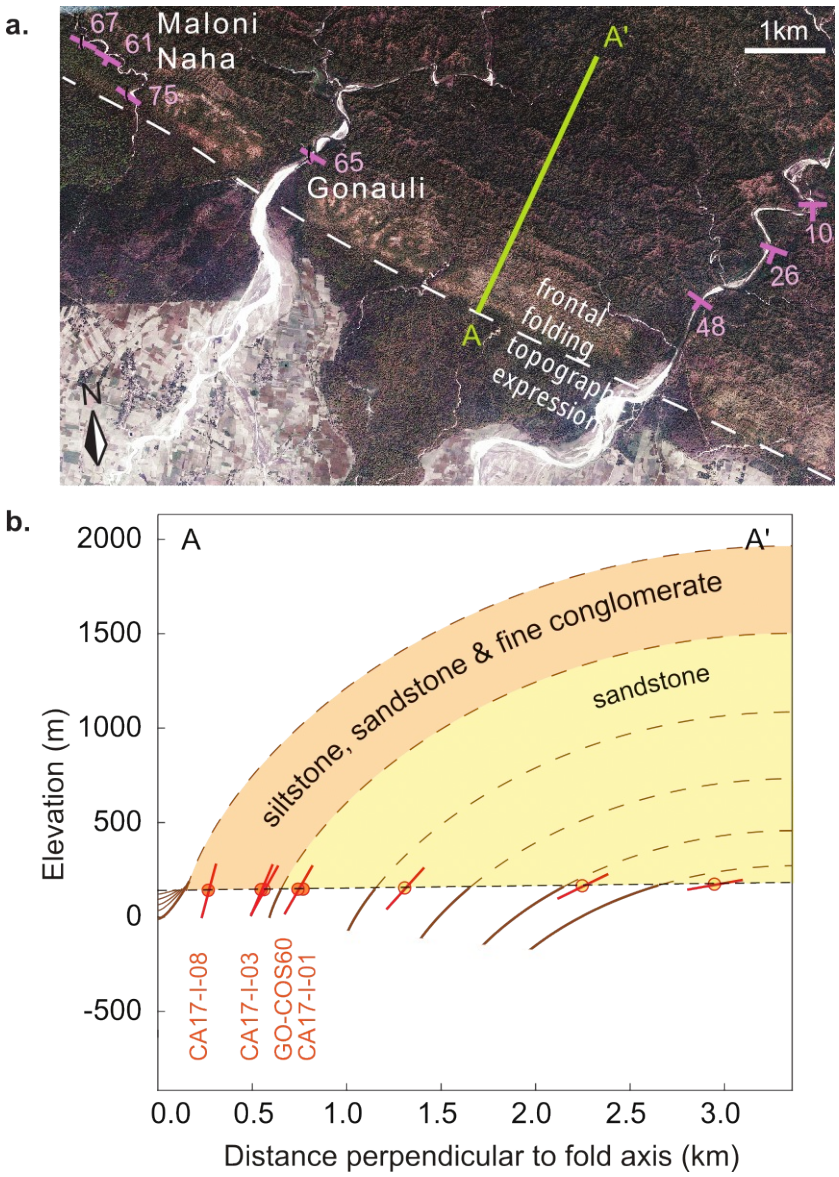

Fig. 4. Composite West Valmiki Section (WVF). Location in the South Chitwan in Fig. 2. **a.** The locations of the discontinuous Gonauli and Maloni Naha surveys are represented by pink marks where samples were collected, with a background satellite image (Google Earth©). **b.** Projection of the dip-measurements and the samples for the three sections on the AA' transect (location indicated in a.).

3.3. Magnetostratigraphy and stratigraphic age model.

To date the EVF Section, we drilled oriented cores in clay and fine (and rarely coarse) sand at regular intervals for paleomagnetism measurement. We collected 20-30% of samples by hand using

plastic cubes in poorly consolidated facies. We carried out sampling every 5 m and systematically included duplicates. We determined the stratigraphic depth of sampling sites using our field measurements (tape measurement, strikes and dips of the strata) and GPS coordinates.

We investigated magnetic mineralogy combining thermo-magnetic curves to determine the Curie points, Isothermal Remanent Magnetisation (IRM) and hysteresis acquisitions. We demagnetized samples using alternating fields and ten to twelve steps, in the paleomagnetism laboratory of the Institut du Globe de Paris, France (IPGP, France). We measured remanences at each step using a three-axis DC Squid. We established the magnetic polarity column based on: (1) samples having a clear and unambiguous magnetic component determined from principal component analysis on Zijderveld diagrams; (2) at least two samples of similar polarity to define a polarity interval. We then correlated the composite magnetostratigraphic column to the reference scale of Ogg (2012) using the Dynamic Time Warping algorithm (Lallier et al., 2013) (see extended methods in Supplementary Information).

3.4. Major element and Sr-Nd isotopic analyses for provenance.

The TSS, HHC, and LH Himalayan lithologic units are made of sediment or meta-sediment, for instance paragneiss and micaschist, with similar major element content, except for carbonate affected by diagenesis and alteration. Contrastingly, major element content evolves in the Himalayan sediment and allows to trace grain-size sorting and weathering (Lupker et al., 2011; Lupker et al., 2012b), or recycling of former Siwalik sediment (Charreau et al., 2020). Contrarily to major elements, the TSS, HHC, and LH have distinct Nd and Sr isotopic signatures in their silicate fraction (Galy and France-Lanord, 2001), which makes these signatures suitable tracers for sediment provenance. With these isotopes, we tested how sediment provenance evolves through time and whether provenance covers the High Himalayas lithologic group (HHC + TSS) as the present Narayani Catchment does.

For major element and Sr-Nd isotopic analyses, we powdered bulk sandy sediment samples in two aliquots. After $LiBO_2$ fusion (Carignan et al., 2001), we measured major and trace elements on one aliquot at Service d'Analyse de Roches et de Minéraux at the Centre de Recherches Pétrographiques et Géochimiques (SARM-CRPG, Vandoeuvre-les-Nancy, France), using ICP-OES iCap6500 for major element and Sc concentrations, and ICP-MS iCapQ for trace elements. We leached the other aliquot with acetic acid to obtain a silicate residue (Galy and France-Lanord, 2001; Hein et al., 2017). We measured Sr and Nd isotopes on the residue at CRPG, using a Triton Plus(TM) multi-collector thermal ionization mass spectrometer with NBS-987 as a standard and quality control and a Neptune Plus (TM) multi-collector inductively coupled plasma mass spectrometer, respectively. We normalized $^{143}Nd/^{144}Nd$ (Yang et al., 2017). Two-sigma analytical errors are $2x10^{-5}$ and $3x10^{-5}$ for $^{87}Sr/^{86}Sr$ and $^{143}Nd/^{144}Nd$, respectively.

We determined for each analyzed sample how the HH (TSS and HHC) and the LH contribute to the silicate fraction of the sediment using Morin's (2015) stochastic inversion, as well as mean values and standard deviation of Sr-Nd concentration and isotope ratio for the three Himalayan units, based on a large dataset of bedrock and monolithologic river sediment (Morin, 2015). Most of error on the respective contribution originates from the statistical uncertainty derived from the uncertainty on the Sr and Nd isotopic ratio of the end-member units (TSS, HHC, and LH). We did not take into account the carbonate contribution in our results. This contribution is low for the HHC and LH, but amounts to 40% of the TSS contribution in present-day Narayani River sand (Morin, 2015). Therefore, the silicate-derived TSS fraction represents a lower bound on the actual TSS fraction.

3.5. ^{10}Be and ^{9}Be measurements in the quartz fraction of Siwalik sediment.

We prepared 42 samples of fine to medium mostly unconsolidated sandstone for analyses of ^{10}Be concentrations. We expected the ^{10}Be concentrations in samples to be low, because of erosion rates potentially higher than 1 mm/y, and we sampled unusual large masses of sand (1 to 5 kg) to extract a sufficient amount of quartz (up to 900 g).

We purified quartz from the sandy samples and prepared it at CRPG for in-situ ^{10}Be measurement. We isolated quartz from the 125-250 μm (or 140-280 μm) fraction, except for coarse-grain samples for which we used the 250-500 μm fraction. Lupker et al. (2012a) found that these two fractions on modern Narayani sediment provide similar ^{10}Be concentration within a 15% margin, which suggests that the results obtained with the two fractions can be averaged for interpretation. We tested this inference by parallel analysis of the two fractions in four samples.

We first removed kyanite and sillimanite with heavy liquids (sodium polytungstate). We further purified quartz using H_2SiF_6 and HCl leachings. We removed atmospheric ^{10}Be from the quartz surfaces by three successive HF leachings. Then, we added an in-house ^{9}Be carrier (or industrial one for seven samples) to samples. We isolated Be following the procedure described in (Lenard, 2019) (see Supplementary Information). We measured ^{10}Be/^{9}Be ratios at the French national Accelerator Mass Spectrometer facility (ASTER-CEREGE, Aix-en-Provence, France) (Arnold et al., 2010), with a normalization following (Braucher et al., 2015), and with an average procedural blank of $3x10^{-15}$ for the in-house carrier (10^{-14} for the industrial carrier).

As we measured unusual masses of quartz, we anticipated a natural ^{9}Be content that could not be negligible compared to the amount of added ^{9}Be carrier. Therefore, we systematically measured the Be content of our sample using ICP-MS at CRPG, following (Lenard et al., 2020). For several measurements, ^{9}Be concentration was up to 20% lower than the expected theoretical values from the added mass of ^{9}Be

carrier (Tab. S7). To be conservative, when calculating ^{10}Be concentrations from ^{9}Be/^{10}Be measurements, we use the higher ^{9}Be content between the ICP-MS value and the theoretical value.

Uncertainties on ^{10}Be concentrations account for analytical measurement of the ^{10}Be/^{9}Be ratio, the blank, and uncertainties linked to the ^{9}Be content considered.

3.6. Model for the ^{10}Be floodplain exposure contribution.

Sediment is exposed to cosmic rays when repetitively transported, deposited and remobilized by erosion of river banks and bottom of the river channel through the Ganga Plain. We estimated the ^{10}Be contribution during sediment transfer using the steady-state mass-balance model of (Lauer and Willenbring, 2010). We validated this model for the Narayani setting using modern ^{10}Be concentrations from the mountain Narayani outlet (MBTO) to the Narayani confluence with the Ganga River (Lupker et al., 2012a) (Supplementary Information Fig. S1; in the following, all figures and tables from the Supplementary Information are numbered starting with a S). As input parameters of the model, such as channel geometry and dynamics, grain size distribution (Tab. S9), we use published data and satellite imagery observations on the modern Narayani River. We assume spatially and temporally steady values for the model parameters throughout the sedimentary history of the Valmiki Section, except for the Narayani Fan, considered to have covered, on the long term, a wider extent than today (Pati et al., 2019). For each sample, we assessed the distance to the mountain front at deposition time. We considered that the migration rate of the mountain front relative to stable India equals the average migration rate of sediment facies, and is steady with a value of 15+/-5 mm/y during the Late Cenozoic in Central Himalayas (Lyon-Caen and Molnar, 1985).

We also added a ^{10}Be contribution during final burial to this ^{10}Be contribution during sediment transfer within the floodplain. We derived this second contribution (Supplementary Information) from the initial sequestration depth. We estimated this depth from field measurements of the stratigraphic depth of the sample, that is the position of the sample below the top of the sedimentary unit to which it belongs. To minimize this final burial ^{10}Be contribution (the greater is the burial depth, the smaller is this contribution), we collected most samples at the base of multi-metric sandstone beds. We calculated the floodplain contribution with a Monte Carlo method to obtain a probability distribution which accounts for the substantial uncertainties associated to the parameters.

3.7. Additional exposure during recent fold exhumation.

Sediment received additional exposure to cosmic rays during exhumation close to the surface during frontal Siwaliks folding. This contribution during exhumation impacts the samples having a low ^{10}Be concentration before exhumation, in particular the oldest samples subject to advanced radioactive decay.

Ideally, we could have minimize the dominant spallogenic component of this contribution by digging 1 to 2 m deep into the outcrop wall before sampling. But digging is difficult into indurated strata and was anyway not welcome since we were required to leave a minor imprint in the Valmiki Tiger natural preservation area. To limit this ^{10}Be recent contribution, we first collected samples at the bottom of cliffs high of 3 to 20 meters, and when possible at the level of a fresh cliff collapse or actively eroding bank (Fig. S2). We quantified this contribution by measuring ^{36}Cl in feldspar from ten samples. Measurements of two radiogenic TCN (^{10}Be and ^{36}Cl) help to unravel complex erosion histories (Lal, 1991; Amidon et al., 2017), since ^{36}Cl has a shorter half-life (301 ky) than ^{10}Be (1.387 My) (Korschinek et al., 2010; Chmeleff et al., 2010). Then, we calibrated a simple exposure model from our ^{36}Cl results.

3.7.1. ^{10}Be contribution during Siwalik exhumation calculated from ^{36}Cl measurement in feldspar.

We separated feldspar from quartz of ten samples using flotation or heavy liquids at CRPG and prepared leached feldspar fractions for ^{36}Cl extraction at CEREGE (Schimmelpfennig et al., 2011). We measured ^{36}Cl/^{35}Cl and ^{35}Cl/^{37}Cl ratios using isotope dilution accelerator mass spectrometry (AMS) at ASTER-CEREGE in 2017 and 2021 (Arnold et al., 2013). We measured the element concentrations in the leached feldspars and in the bulk sediment at SARM-CRPG (Table S10). Using the spreadsheet version of the online CREp ^{36}Cl calculator (Schimmelpfennig et al., 2022) with our ^{36}Cl and element concentrations, we derived the contributions of the spallogenic and muonic contributions, and of the ^{35}Cl capture of thermal and epithermal neutrons. We hypothesized water-saturated samples at depth, using (Baldwin and Butler, 1985)'s compaction curve for sandstone to approximate sandstone porosity and density as a function of depth, (taking a solid rock density of 2.7 g/cm). This porosity estimate was previously validated for Siwalik sandstone sampled in Central Nepal (Dubille, 2008). The calculated porosity decreases from 40% to 20% for increasing sample ages.

For sediment older than 2-3 Ma, the spallogenic and muonic ^{36}Cl components, $^{36}Cl_{cosmo}$, are only due to recent exposure at the outcropping surface and not to the initial ^{36}Cl before sediment burial because it has totally decayed. To handle this, we computed the ^{36}Cl production rates in feldspar, $P_{F_{36}}$, at the sample site elevation (~200 m.a.s.l.) according to the concentrations of K and Ca in each feldspar sample. We derived the ^{10}Be contribution due to recent exposure using the ratio between the ^{10}Be production rates in quartz and the ^{36}Cl production rates in feldspar at this elevation for steady erosion, $\frac{P_{Q_{10}}}{P_{F_{36}}}$:

$$^{10}C_{rex} = \frac{P_{Q_{10}}}{P_{F_{36}}} . {}^{36}C_{cosmo} \qquad \text{(Eq. 2)}$$

For sediment younger than 2 Ma, the initial ^{36}Cl before sediment burial, despite having decayed by radioactivity, cannot be neglected compared of the recent exposure contribution. For this young sediment, we used a modified formula to estimate the recent exposure (Supplementary Information).

3.7.2. Model of ^{10}Be contribution during exhumation for samples without ^{36}Cl measurement.

Independently, we estimated the ^{10}Be contribution during exhumation using a simple model of TCN production close to a surface under steady erosion:

$$ {}^{10}_{model}C_{rex} \cong F \,.\, S_F \sum_{j=1,2,3} \frac{\Lambda_j P_j}{\varepsilon_{rex} \rho_s}, \qquad \text{(Eq. 3)} $$

with P_j the local cosmogenic production rate for all three pathways (spallation, slow and fast muon capture), ε_{rex} the local modern erosion (incision) rate, ρ_s sandstone density, S_F the shielding factor and F a qualitative factor. We set F to 0 for sample sites with fresh cliff collapse or evidence of marked outcrop erosion between 2012 and 2016 (Fig. S2), 0.5 for sites with fairly recent cliff erosion, or 1 for sites without evidence of recent erosion (Tab. S8).

Based on both exhumation rates of the fold (see § 5.1.) and incision rates measured farther east (Lavé and Avouac, 2000), we expected ε_{rex} = 5-10 mm/y as average erosion rates in the Dwarda Section – and lower erosion rates for the WVF. We computed a maximum topographic shielding factor for each sample from the cliff angle. For most samples, the cliff is sufficiently high to approximate the angle as an infinite slope for the spallogenic pathway. We made the shielding factor vary between 1 (steady vertical erosion of the surface) and the minimum value (lateral erosion added to vertical erosion) using a Monte Carlo approach to derive the Pdf (Probability Density Function) of the recent exposure of each sample.

For the ten samples analyzed for ^{36}Cl in feldspar, we compared the ^{36}Cl-derived recent exposure to the concentration predicted by this simple erosion model, considering local geometric factors of the sampled outcrop (cliff height and angle). After estimating the average exhumation rate that best reflects the ^{36}Cl-derived recent exposure, and in absence of systematic measurement of ^{36}Cl in the feldspar for all our 42 samples, we used this calibrated model to calculate the recent exposure contribution to the overall ^{10}Be concentrations.

3.8. ^{10}Be initial Himalayan paleoconcentrations and ^{10}Be paleoerosion rates.

Following (Eq. 1b), we subtracted the cosmogenic contribution during exhumation to the measured ^{10}Be concentrations. We corrected the results for radioactive decay using λ_{10Be} = 4.998±0.043×10^{-7} y^{-1} (Korschinek et al., 2010) and obtained ^{10}Be uncorrected paleoconcentrations. We subtracted the

cosmogenic contribution during sediment transfer from the results to obtain the ^{10}Be initial paleoconcentrations reflecting Himalayan paleoerosion.

To convert initial Himalayan paleoconcentrations into paleoerosion rates, we assumed that the cosmogenic production rate in the contributing catchment, supposedly the Narayani Catchment, has remained steady since 7.5 Ma and close to the modern value (discussion in § 5.2.2.).

We computed ^{10}Be production rates with the modified Lal-Stone scaling model (Lal, 1991; Stone, 2000) using the Basinga tool box (Charreau et al., 2019). We set the sea level high latitude (SLHL) production rate at 4.18 atom/g (Martin et al., 2017), with factors of 0.9886, 0.0027 and 0.0087 for the SLHL neutron, slow and fast muonic pathways (Braucher et al., 2011). The cosmogenic production rate calculation includes the glacial cover provided by the GLIMS database (Raup et al., 2007) assuming glaciers totally shield underlying rocks and hence produce sediment with null cosmogenic concentration (for instance, Charreau et al., 2019). We did not include topographic shielding (DiBiase, 2018) nor paleomagnetic temporal variations. The variations of the magnetic dipole affect production rates especially at low latitudes. But on average, production rates can be considered relatively steady at +/-20% since 4 Ma (Lenard et al., 2020). The Narayani contributing area was defined by its catchment upstream of Narayangarh (or MBTO) (red-outlined catchment, Fig. 1) and does not include the frontal Siwalik units. We propagated paleoerosion rate uncertainties from uncertainties associated to (1) measured ^{10}Be concentrations, (2) production during sediment transfer and recent Siwalik exhumation, and (3) stratigraphic ages, using a Monte-Carlo approach.

4. Results and interpretation.

We first describe the fold structure and sedimentologic stratigraphy of the main composite section, the East Valmiki Fold (EVF) Section (§ 4.1.1.). We briefly present the complementary, discontinuous, composite section, the West Valmiki Fold (WVF) Section (§ 4.1.2). Then, we develop our magnetostratigraphic dating results on the EVF Section, and estimated ages on the WVF Section (§ 4.2.). We present our major element and Sr-Nd isotopic results that we combine with our sedimentologic observations to interpret the depositional setting, weathering, and sediment provenance (§ 4.3.). We present our TCN ^{10}Be concentration results (§ 4.4.1.) and interpret them as paleoerosion rates of the Narayani Catchment (§ 4.4.4.), with corrections for plain exposure during sediment transfer (§ 4.4.2.) and recent exposure due to Siwalik exhumation, with our ^{36}Cl measurement (§ 4.4.3.).

4.1. Field observations on the Valmiki Section.

4.1.1. The East Valmiki Fold (EVF) composite section.

Fold structure.

We mainly focus our study east of Gobardhana village on the EVF Section, a set of three parallel surveys (or subsections) along small rivers in the south flank of the EVF in its central part, from west to east, the Dwarda River, the Ganguli River and the Patalaia River (Fig. 3). Surveyed stratigraphic thickness amount to 3,500 m, 380 m, and 210 m, for the Dwarda, the Ganguli and the Patalaia Section, respectively. Bedding attitudes orient uniformly at N95. This improves stratigraphic matching between the surveys. The three subsections overlap and Patalaia extends the section to recently deposited Siwalik sediment. We consider that their equivalent level under the Ganga Plain is ~100 m deep.

Folded sedimentary strata mostly consist of a continuous series of south-dipping, 55-65° inclined beds. South, over a distance of 380 m along the frontal part (above 300 m depth), bedding flattens down to 30° (Fig. 3b). Flattening supposedly reflects the signature of syn-folding sedimentation. North (below 2,600 m depth), bedding gradually flattens down to 25°. We assume bedding flattens down to sub-horizontal attitude near the range crest line. Along with flattening bedding strike rotates counter-clockwise, from south dipping to SE dipping. Between both ends of the section, we did not identify any stratigraphic duplication, major unconformity or fault. The EVF develops over a width of 12 km, as an anticline with a 60° steep south frontal limb. Without published structural data on the northern limb, we cannot assess the geometry and possible asymmetry of the fold and cannot determine finite shortening. We did not observe a frontal tectonic scarp, which suggests that the MFT is blind at this location. At the fold front, 10 km east of the Ganguli River, alluvial terraces display bedding-parallel scarps. We interpret these scarps as flexural slip. These two observations suggest that the EVF might correspond to a fault propagation fold. This fold is eroded for the most part, as shown by the contrast between the local topography 600 m above the Ganga plain and the exhumation of 4,000 m of rocks.

Stratigraphic description.

We distinguish five facies FA1 to FA5, from the base to the top (Fig. 5):

FA1. At the bottom, from 3,900 to 3,300 m. Metric, fining upwards, fine sand to silty beds dominate. They rarely alternate with clay, paleosoils, and massive, decametric fine to medium sandstone bodies. These bodies present rare cross-bedding and contain few centimetric quartz or quartzitic pebbles or fine intraformational conglomerates of mud gravel, and rare silt lenses.

FA2. From 3,300 to 2,900 m. Massive and plurimetric to decametric fine to medium sandstone bodies gradually dominate. The fining upwards, from medium sand to fine sand and silty beds, is not

regular, and occurs up to the top of this group. Close to the top of the group, several centimetric coarse to gravelly beds with erosive bases interbed within the sandstone bodies.

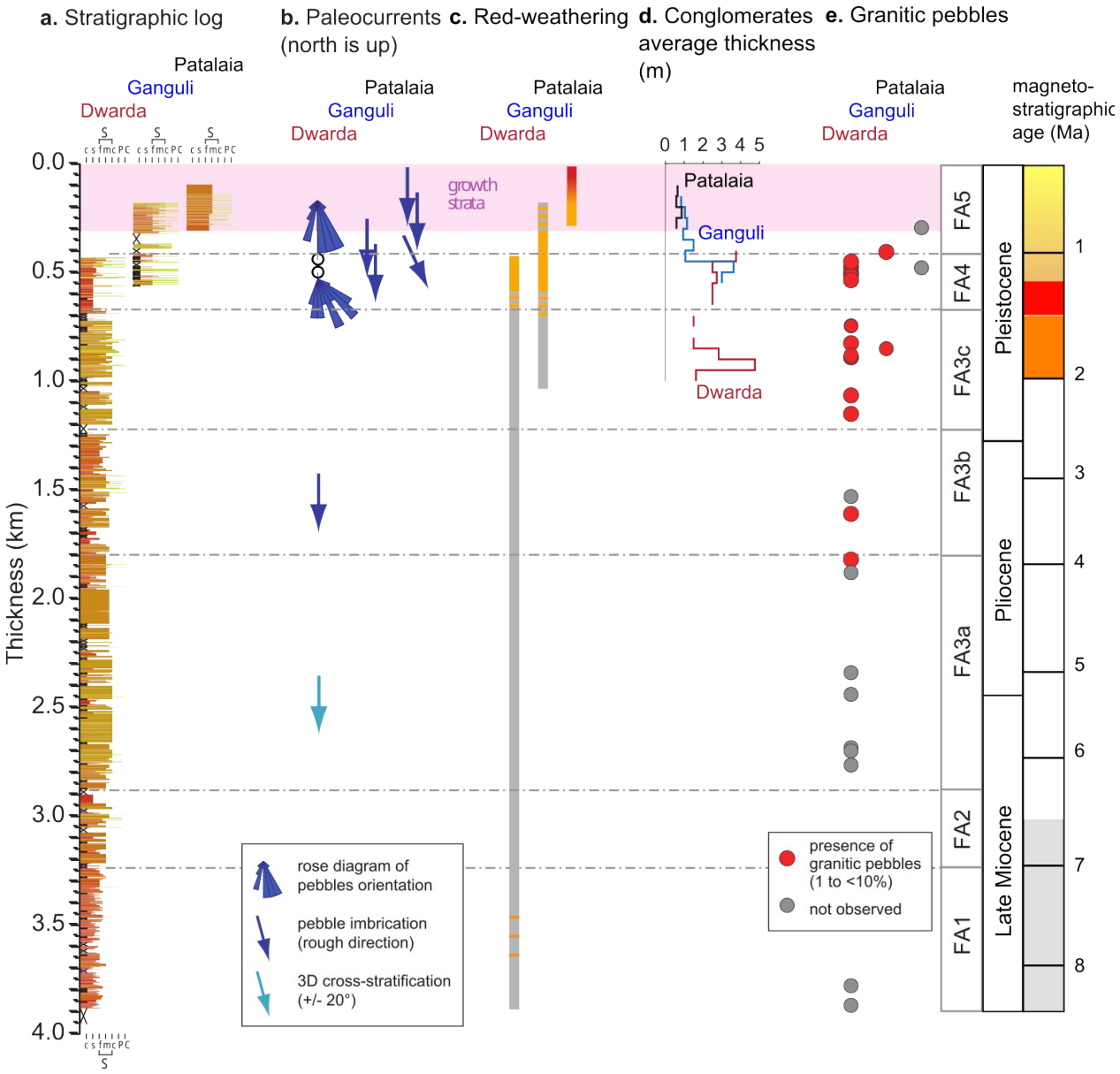

595 **Fig. 5.** Stratigraphic column and field measurements. For clarity, only the composite continuous EVF Section is presented (and not the discontinuous composite WVF Section). Location of the EVF Section is indicated in Fig. 2-3. **a.** Stratigraphic logs, with c: clay, s: silt, S: sand, f: fine sand, m: medium sand, c: coarse sand, P: pebble, C: cobble. Log colored for clarity. Fine to medium sandstone favorable for ^{10}Be measurement are present all over the Section. **b.** 600 Paleocurrent directions, which mostly point to a permanent southward direction over time. **c.** Weathering intensity of sediment, with gray-colored: grayish mudstone, orange-colored: orange

weak-weathering of mudstone and fine sandstone, red-colored: red deep-weathering of all the facies. **d.** Average thickness of the conglomeratic layers and of the sandstone layers over a sliding window of 50 and 100 m respectively. **e.** Presence or absence of granitic pebbles in the conglomeratic layers or in the pebble-rich base of the coarse sandy layers. Facies FAx are indicated (see § 4.1.1.). Additionally, we report our magnetostratigraphic age results fully presented in Fig. 8. We also highlight in the form of colored rectangles, the periods < 1.25 Ma, 1.25-1.5 Ma, 1.5-2 Ma, 2-6.5 Ma, and > 6.5 Ma, which we also highlight in the subsequent figures and refer to when we interpret our results.

_____

FA3. From 2,900 to 700 m. Almost continuous, pluridecametric, massive, medium to coarse sandstone bodies present a "salt and pepper" appearance. These bodies have planar stratification or cross-bedding, lenses of silt and occasional nodules, indurated by calcite cement. They regularly incorporate mud clasts, either isolated or in metric pebbly beds (intraformational conglomerates or puddingstones) and channel lag deposits rarely intercalate with other layers. The sandstone bodies are occasionally fine-grained or, conversely, contain thin bed of gravels/pebbles or isolated quartzite gravels. We identify three sub-units. FA3A, below 1,800m, the sandstone bodies dominate and metric fining-up thin beds and clayey beds are rare. FA3B, from 1,800 to ~1,200 m, metric, fining upwards, fine sand to silty beds and metric to rarely decametric, silty to clayey horizons are present. FA3C, above 1,200 m, plurimetric to decametric massive medium to coarse sandstone bodies dominate, with a slightly decreasing thickness (below 5 m).

FA4. From 700 to 400 m. Fine-grained bodies dominate but an early appearance of some major clast-supported conglomeratic beds is observed. Plurimetric (2 to 5 m), yellow-grey unconsolidated mud to siltstone, sandstones and pebbly beds alternate. The Ganguli has more pebbly beds than the Dwarda, despite incomplete strata exposure. Conglomeratic layers show well sorted and rounded pebbles with imbrication patterns (Fig. S2). Most pebbles apparently derive from quartzite or quartz-rich LH resistant sandstone, and a few ones from granite. Yellow to orange color weathering in silty to muddy layers suggests a longer exposure in the plain before burial.

FA5. From 400 to 100 m. In the Ganguli and Patalaia. Metric conglomeratic gravelly to pebbly beds intercalate with massive silty to medium sand. Sand occasionally contains fine gravelly lenses and conglomerates represent 40% of the strata. Compared to FA4, gravel beds are thinner (~1m), clasts are smaller and contain a certain proportion of subangular shapes, and granitic pebbles are absent. Weathering follows an upward gradient, with deep red-weathering for the most recent levels in the Patalaia survey, which points to a long exposure duration in the plain before burial.

We measured a few paleo-current directions (Fig. 5), mostly from pebble imbrications, which all indicate a southward or SSE-ward direction of flowing, consistent with sustained sediment supply from rivers draining the Himalayas toward the southern part of the Ganga Plain. Most pebbles are quartzite or quartz-rich lithified rocks and probably originate from the LH. The Dwarda and lower Ganguli conglomerates contain a few granite pebbles, probably sourced from the upper HHC granites or from the granites outcropping in the klippen of HHC and TSS in the LH. These well rounded pebbles, whatever their lithology, suggest that they represent pristine material from the Himalayan hillslopes that survived to long distance transport. We did not observe gneiss pebbles, probably because they do not survive long transport distances due to their erodibility of two orders of magnitude higher than quartzite (Attal and Lavé, 2006), and because of the deeper weathering of biotite- and feldspar-rich lithologies during transfer through the Ganga plain (Lupker et al., 2012b). In the Patalaia and upper Ganguli, granite pebbles are absent and the proportion of subangular pebbles becomes visually significant. This suggests a short transport distance, with an origin from the pebbles recycled from the conglomerates of the upper Siwaliks (Dubille and Lavé, 2015).

4.1.2. The West Valmiki Fold (WVF) composite section.

We completed the EVF section with samples potentially corresponding to the most recent sediment deposited by the Narayani River before they have been exhumed by the growth of the frontal Siwalik folds. For this, we collected a few Pleistocene sediment samples, in the southern limb of the young WVF (Fig. 2), close to the current Narayani MFT outlet (MFTO). We carried out sampling along two small rivers draining a subdued topography, the Maloni Naha River and the Gonauli River (Fig. 4). These rivers only expose limited, discontinuous sections which we did not date by magnetostratigraphy. We estimated stratigraphic ages from the structural position of the samples using a sediment accumulation curve similar to the EVF section.

We performed bedding dip measurement along the downstream part of these two rivers and along a third one located 5 km eastward (Fig. 4a), and we completed with observations on satellite imagery (Google Earth©). The WVF presents a 9.5 km wide asymmetrical anticline with a steep south frontal limb, dipping up to 75° near the front, probably corresponding to the expression of a fault propagation fold. The finite shortening accommodated by the anticline is 2 to 2.5 km, and structural uplift reaches 2 km at the fold axis. This small amount of the finite shortening suggests that the fold initiated only a few hundreds of thousand years ago.

The facies of this section are similar to FA4, although less well structured. Specifically, we observe a few gravelly beds/lenses intercalated with silty/muddy and fine sand layers. Yellow to orange color weathering in silty to muddy layers indicate some exposure in the plain before burial.

4.2. Paleomagnetic measurement and magnetostratigraphic scale.

Paleomagnetic measurement is restricted to the three EVF sections with continuous sampling. The paleomagnetic results and the magnetostratigraphic correlation are presented in Fig. 6-7-8, Fig. S3-S4, Tab. S2-S3. Rock magnetism experiments indicate that titanium-poor magnetite is the dominant magnetic mineral in all samples but is sometimes associated with hematite (see Supplementary Information). Among the 397 demagnetized samples, 125 have unstable direction and are not interpreted, 188 have a relative stable component that decay toward the origin and 84 have remanent direction trajectories that follow great circle paths (Fig. 6c). Among the 188 samples having a stable component, 104, 76 and 8 where interpreted as normal, reverse polarities and intermediate directions (that is east-west directions, normal directions with negative inclination and reverse direction with positive inclination), respectively.

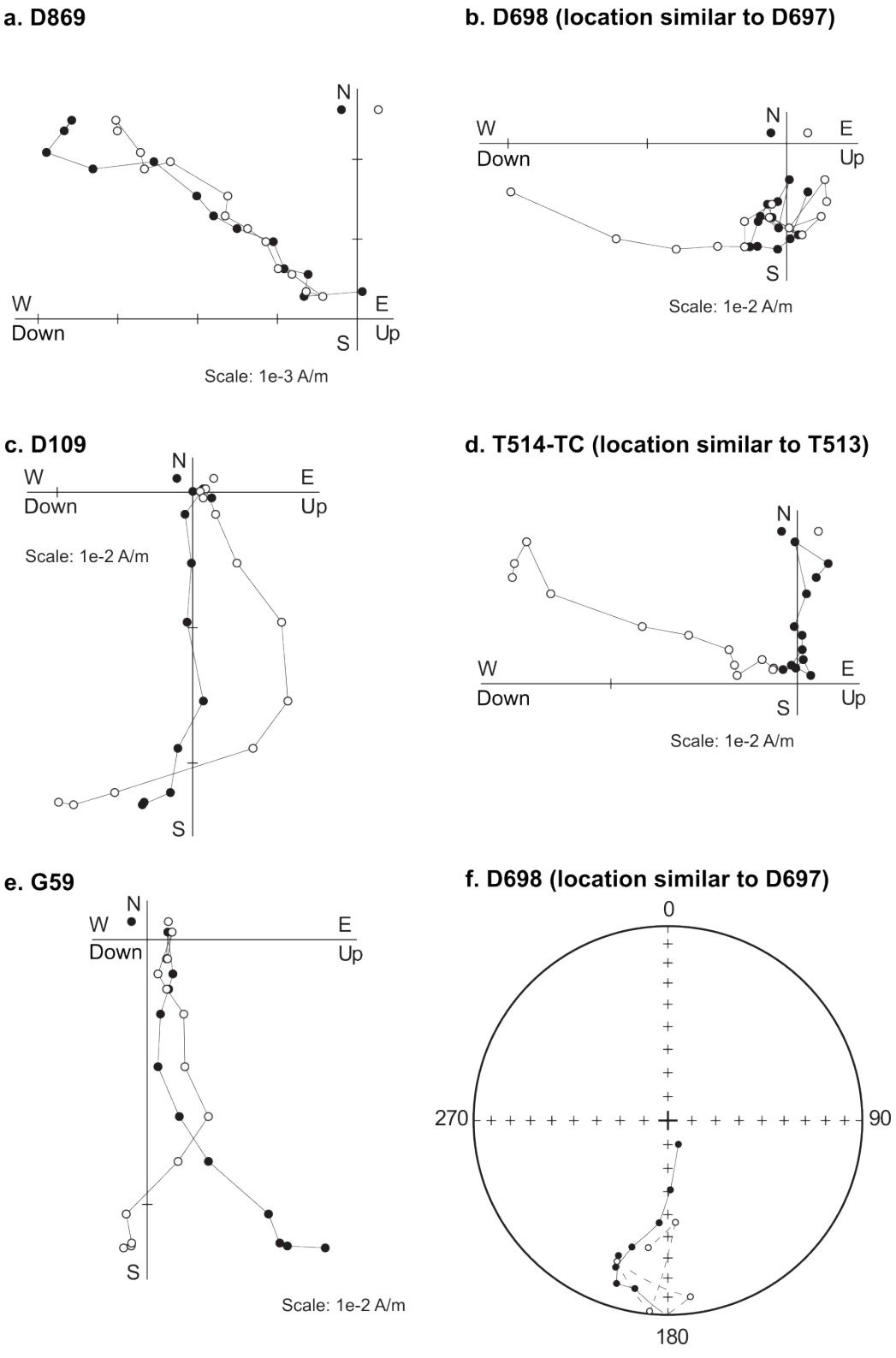

680 **Fig. 6.** Representative Zijderveld diagrams (**a-e**) and stereoplot projection (**f**). (Zijderveld, 1967). Dwarda, from bottom to top, samples D109, D698 (D697) and D869 (a-c). Patalaia: sample T514-TC (T513) (d). Ganguli: sample G59 (e). Stereoplot for the Dwarda sample D698 (D697) (f).

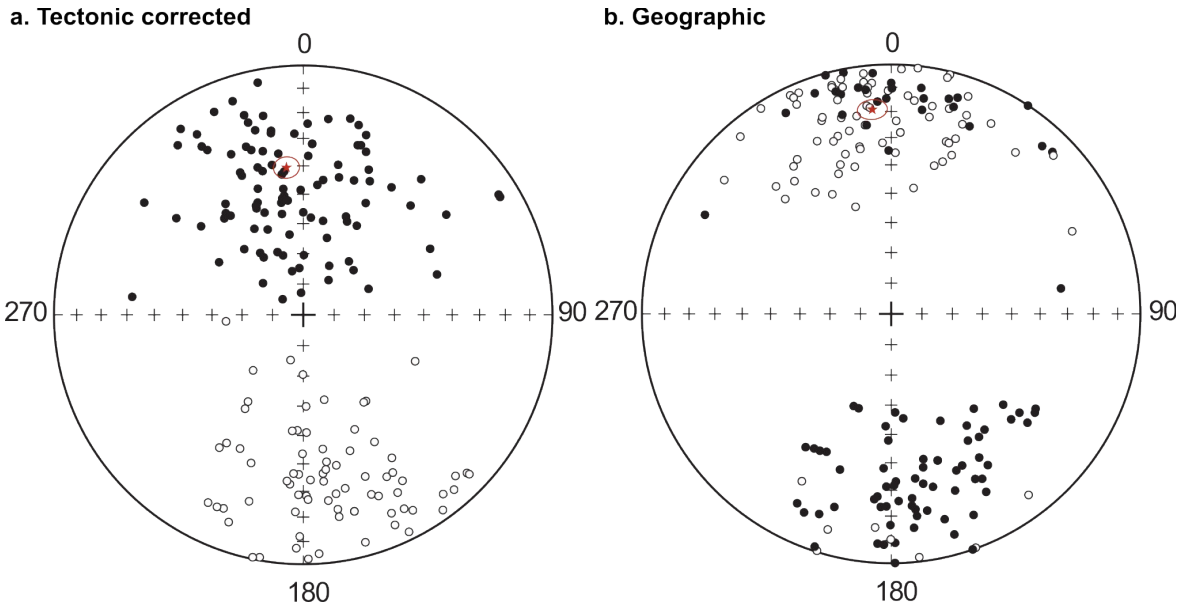

Fig. 7. Stereonet projections. Normal and reverse polarities are represented (a-b). Red star: mean direction.

We provide Zijderveld interpretations, stereoplot projections of the stable components, their mean directions and statistical analysis to ensure the primary of the remnant directions in the Supplementary Information.

The magnetostratigraphic column, built from the 189 samples having a reliable magnetic component, displays 14 normal polarity intervals and similar number of reversed ones (Fig. 8d). We determined most polarity intervals using more than three samples of similar polarity. However, we defined magnetic polarities intervals r2, r5, n6, n9 and r10 (Fig. 8) by one single sample only, but for each of these intervals we demagnetized a second sample from the same stratigraphic horizon to confirm the first result. The results in the three overlapping EVF subsections are consistent and confirm that their relative positioning in the final stratigraphic scale is adequate.

We correlated our results to the reference scale using the dynamic time warping algorithm of (Lalier et al., 2013). Most probable correlations date the Valmiki Section from 8 Ma to 0 Ma (reference chrons C4A to C1), with sedimentation rates steady on average, close to 0.5 mm/y. First, we determined an age model with all intervals (Fig. S5). But that model correlates the normal interval n2 to C1r.1n/2n and produces an unconformity at the base of the r2 reverse interval, followed by a sedimentation rate unrealistically larger than the mean subsidence rate (below 0.5 mm/y) documented in front of the central

Himalayan range (Ojha et al., 2009). We discarded that model and determined a new age model without the n2 interval, which we consider as our reference chronostratigraphic scale (Fig. 8d).

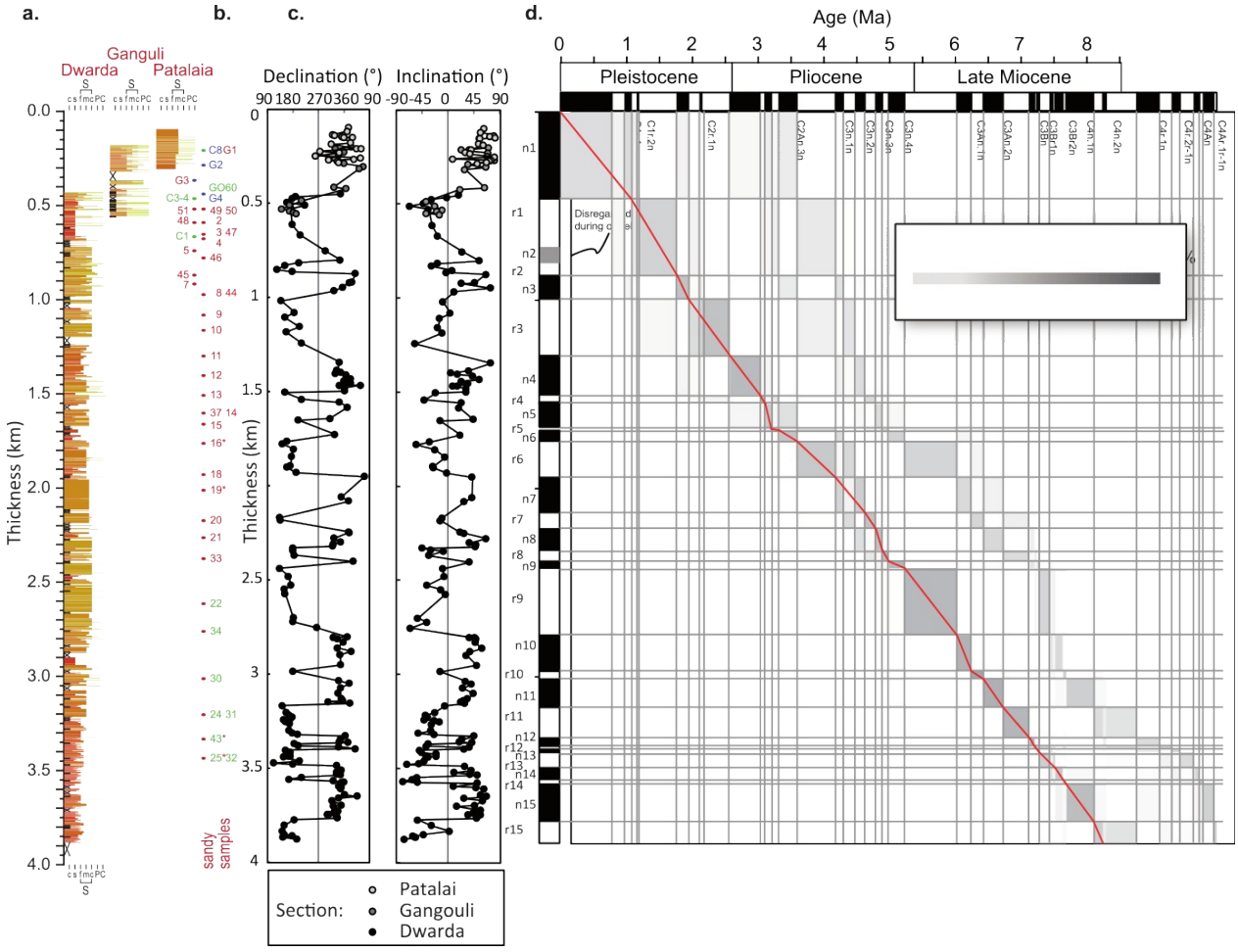

Fig. 8. Magnetostratigraphic column and correlation to the reference scale. Only the presented here, continuous composite EVF Section was dated by magnetostratigraphy. **a.** Stratigraphic logs of the composite EVF Section (see Fig. 5). **b**. Stratigraphic position of the sandy samples with geochemical and isotopic results. The sandy samples are colored whether they are from the Dwarda (red) and the Ganguli (blue), or from the WVF Section (green). Sample abbreviations are indicated Tab. S4. No geochemical or isotopic measurement for the Patalaia. **c**. Magnetic declination and inclination (Tab. S3). **d.** Magnetostratigraphic column and correlation to (Ogg, 2012)'s reference scale. The density plot compiles 10,000 possible correlations to the reference scale. We determined these correlations using (Lallier et al., 2013), with assumed minimal variations of accumulation rates over time. We disregarded polarity interval n2 because the inclusion of n2 requires an unconformity unobserved in the field (see § 4.2. and Fig. S5 for an alternative column which

includes n2). We determined magnetic intervals with two successive horizons of the same polarity. We excluded samples with transitional directions. Red curve: best fit age model.

We estimated the stratigraphic ages of the samples collected in the West Valmilki folds from the structural position of the samples using a sediment accumulation curve similar to the EVF area. Those five WVF samples were dated at 0.465, 1.076, 1.101, 1.412 and 1.453 Ma.

4.3. Major element and Sr-Nd isotopic analyses to trace provenance.

4.3.1 Major elements.

The 39 sandy analyzed samples cover ages from 7.5 to 0.5 Ma. Because of variable carbonate content in Himalayan sediment, related to pedogenesis during sediment burial or dissolution during fold exhumation, we favored an investigation of elemental ratios, that is concentration normalized to Si (Lupker et al., 2012b), rather than raw concentrations (Fig. 9, and Fig. S6).

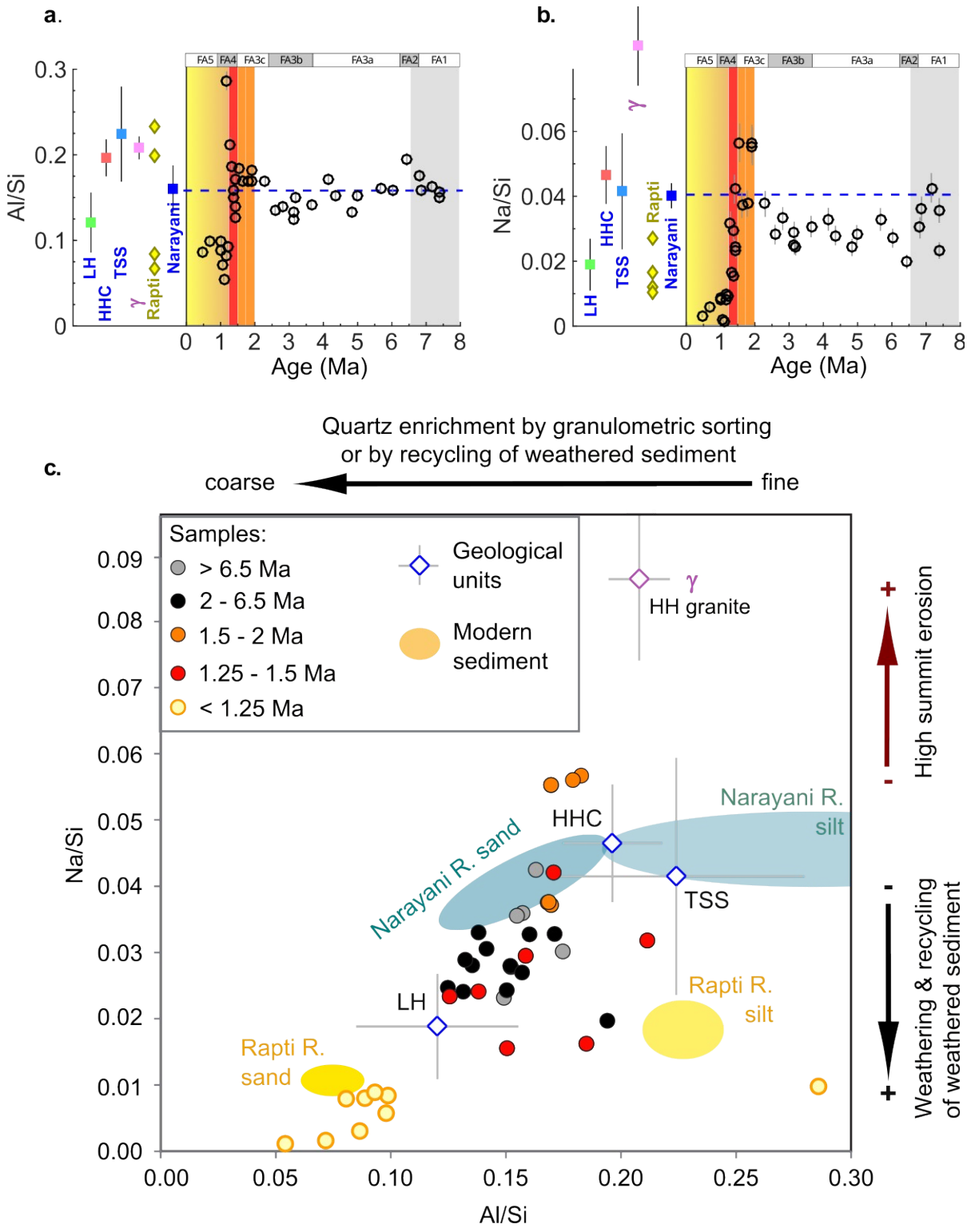

735 **Fig. 9.** Evolution since the Late Miocene of Al/Si (**a**) and Na/Si (**b**) in our sandy samples of the Valmiki Section. Displayed on the left for comparison: main Himalayan units (HHC, TSS, LH, and Himalayan leucogranite 'γ') and sediment of the Narayani River and the Rapti River (this latter

mostly drains Siwalik reliefs in the Chitwan Dun). **c.** Na/Si vs Al/Si, samples plotted with an age-dependent color scale. Blue-contoured diamonds: mean modern values for the main Himalayan units (Morin, 2015). Blue- and yellow-colored ellipses: mean range of values for sandy and silty modern samples of the Narayani River and the Rapti River. Al/Si reflects sample grain size (Lupker et al., 2011) or quartz enrichment during weathering and recycling of Siwalik sediment like in the Rapti River. In these sands, Na/Si drop compared to the Narayani end-member reflects Na depletion associated to plagioclase weathering, and more generally sediment weathering (Lupker et al., 2012b). Pre-1.25 Ma samples show weak weathering (25% Na/Si depletion) consistent with burial in the Ganga Plain: we can thus consider them as direct erosion products of the HH (TSS + HHC). Post-1.25 Ma samples show deep weathering and coarsening, similar to recycled sediment of the Rapti R.: we cannot consider them as direct products of the HH and we exclude those post-1.25 Ma samples in our paleo-erosion reconstruction. On the other hand, during the 1.5-2 Ma period, several samples show a Na-enriched signature, higher than the main Himalayan units, suggesting an increased contribution from the High Himalayan leucogranite.

Our elemental results on the Valmiki sand show substantial variation since the Late Miocene, with three periods.

(1). From 7.5 to 2 Ma, ratios have low dispersion, compatible with an origin from a ternary mix of the main Himalayan lithologic units HHC, TSS and LH. The ratios are close to the modern Narayani sand (Fig. 9) for immobile elements such as Al, Fe or Ti. On the contrary, Ca/Si and Mg/Si are much lower than in modern Narayani sediment, as expected from variable carbonate content. Na/Si is ~25% below modern Narayani. We interpret this as consistent with Na depletion associated with plagioclase weathering, as documented for sediment transfer in the Ganga Plain (Lupker et al., 2012b).

(2). From 2 to 1.25 Ma, ratios have a greater dispersion of values, in particular for Na/Si (Fig. 9a-b, Fig. S6). As shown in a Na/Si vs Al/Si chart (Fig. 9c), three samples older than 1.5 Ma present higher Na/Si than the modern Narayani sand. We cannot explain those values by a mix of the average LH, HHC and TSS end-members. In the Narayani, the main pole of Na-rich sediment is associated with the rivers draining the leucogranite-rich units of the High Himalayas (Manaslu and Langtang regions, labeled HH granite in Fig. 9c). We assume that this pole is a possible origin for these samples. At the opposite, several samples younger than 1.5 Ma display depleted Na/Si (Fig. 9) despite normal content in other elements except Ca (Fig. S6). Na-depletion is concomitant with orange-weathered siltstone, and we propose that

Na-depletion is caused by a deeper weathering in a sedimentary setting (stratigraphic period FA4) with less frequent visits of the main channel and dominated by overbank deposits.

(3). The period younger than 1.25 Ma shows SiO_2-enrichment (90% vs 75%) and strong depletion in other elements (Fig. 9, Tab. S4). The most mobile elements, Ca, Mg, Na, are almost absent. Elemental depletion is hardly compatible with a mix of the average LH, HHC and TSS end-members. We also observe such a depletion in the modern sand of local rivers draining the Siwaliks Hills, regardless of grain size and Al content (Fig. 9a, c). This suggests that samples younger than 1.25 Ma may derive from local Siwalik-draining rivers like the Rapti River (see also the Surai Section in Charreau et al., 2021)**.**

4.3.2. Sr-Nd isotopes and relative contribution of Himalayan geological units.

Our $^{87}Sr/^{86}Sr$ and εNd results on the Valmiki sand range from 0.745 to 0.78 except one outlier at above 0.8, and from -19 to -16, respectively (Fig. 10, Fig. S7, Tab. S6). We divide their evolution in two periods (Fig. S7). From 7.5 to ca. 2 Ma, average $^{87}Sr/^{86}Sr$ decreases from 0.77 to 0.76. The εNd decreases coevally from -17.4 to -18.5, with widely dispersed values. After 2 Ma, the isotopic trend shifts. The εNd increases to -17.4, with still a large dispersion, and the $^{87}Sr/^{86}Sr$ drops to ~0.75 before returning to ~0.77 for samples younger than 1.25 Ma.

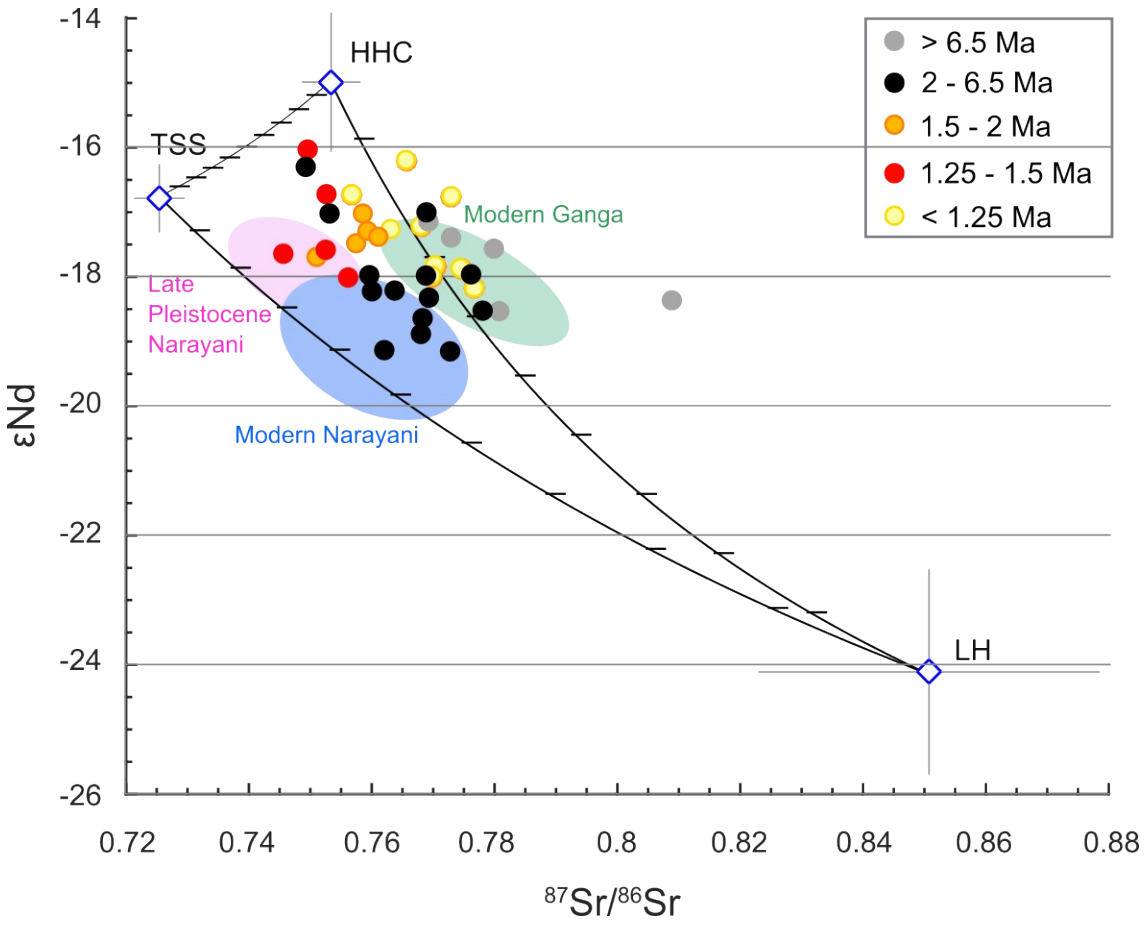

Fig. 10. Evolution since the late Miocene of the εNd and $^{87}Sr/^{86}Sr$ of our sandy samples of the Section. Samples plotted with an age-dependent color scale. Color-filled ellipses: mean range of values for the modern Narayani and the Ganga sand and the late Pleistocene for the Narayani Fan (Morin, 2015). Black curves: ternary mixing between the main Himalayan units. Most Sr-Nd isotopic signatures of the Valmiki and modern Narayani sand fall within the mixing domain of these three units, with the exception of the pre-6.5 Ma samples, which have a slightly more radiogenic Sr signature, similar to the modern Ganga.

We plotted the isotopic ratios against each other in a ternary diagram (Fig. 10). All samples, except one $^{87}Sr/^{86}Sr$ outlier, fall within or close to the ternary mixing range defined by the HHC, TSS and LH. Most samples are dominated by TSS and HHC compared to LH. The Valmiki samples are individually within the range of isotopic values of the modern Narayani River sand or the Narayani Fan developed during the Late Pleistocene (Singh et al., 2008; Morin, 2015). But we observe that the average value of the

Valmiki samples is offset to the right compared to the average value of the modern or Late Pleistocene sediment in the ternary diagram.

Siwalik sediment shows an average Na/Si depletion of 25% compared to present-day Narayani sand. We assume that depletion is related to plagioclase weathering. Because plagioclase is Rb-poor and Sr-rich relative to micas and the middle silicate phase in Himalayan rocks, any loss of plagioclase in rocks induces a more radiogenic Sr signature of the silicate phase, that is a higher $^{87}Sr/^{86}Sr$ compared to modern Narayani.

In the Valmiki samples, two populations stand out. (1) Samples older than 6.5 Ma and samples younger than 1.25 Ma shift to the right of the ternary diagram. For Valmiki samples younger than 1.25 Ma, we consider that Na depletion and the higher Rb/Sr ratio illustrate plagioclase deep weathering (Fig. S6). Because plagioclase is less radiogenic than micas, the $^{87}Sr/^{86}Sr$ of plagioclase-depleted sediment shifts to the right of the ternary mixing diagram. Contrastingly for the Valmiki samples older than 6.5 Ma, we do not observe any Na-depletion or higher Rb/Sr compared to Pliocene samples and the plagioclase/mica composition cannot explain the higher $^{87}Sr/^{86}Sr$ signature. We can only note that their signature shifts away from modern Narayani sediment towards modern Ganga sediment (Lupker et al., 2013).

We inverted the isotopic ratios into the relative contributions of each lithologic unit and provide a more quantitative view on provenance over time (Fig. 11, Tab. S6). The relative contributions of the HH (HHC+TSS) and of LH have remained roughly constant since the Late Miocene, with values around 70+/-10 and 30+/-10% respectively. Within the HH contribution, the HHC and TSS relative proportions display variations. The HHC contribution decreases from 60 to 45% while the TSS contribution increases from 0 to 20% from 7.5 to 2 Ma, followed by rapid, contrasted variations between 2 and 1.25 Ma. From 2 to 1.5 Ma, the TSS contribution peaks at ~40% (Fig. 11), close to modern or Late Pleistocene contributions (Morin, 2015), before dropping again at values of 20+/-10% from 1.5 to 1.25 Ma.

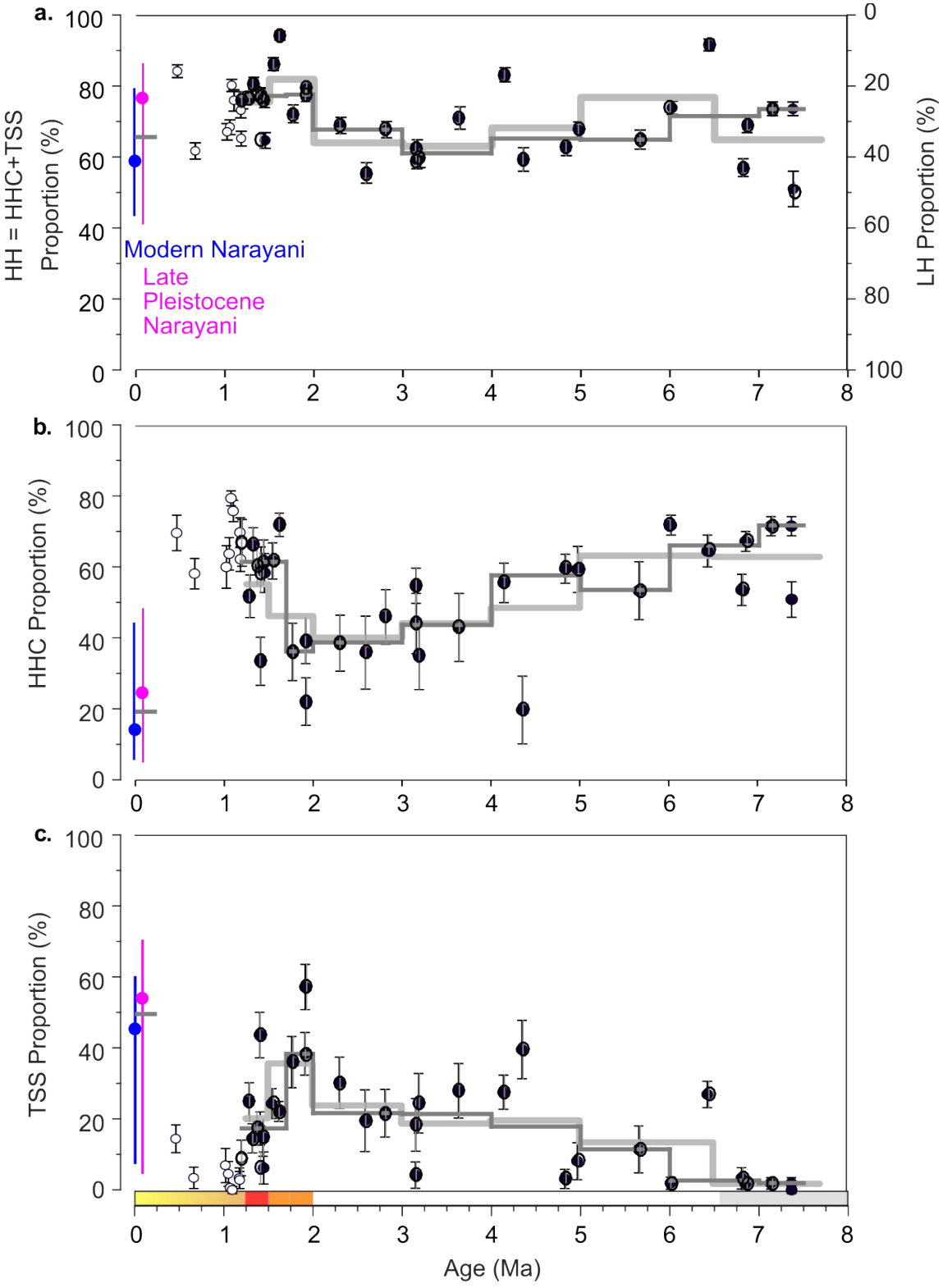
a.
HH = HHC+TSS Proportion (%)
LH Proportion (%)
Modern Narayani
Late Pleistocene Narayani
b.
HHC Proportion (%)
c.
TSS Proportion (%)
Age (Ma)

825

Fig. 11. Relative contributions of the main Himalayan units in the sediment mix. We calculated the ternary sediment mix for the sandy samples of the Section based on our Sr-Nd isotopic values and on the mean modern values for the main Himalayan units: LH (a), HHC (b) and TSS (c) (mean values from Morin, 2015). On the left, proportions for the modern and late Pleistocene Narayani are also presented, with vertical bars showing the dispersion of measured values (Morin, 2015).

4.4. ^{10}Be concentrations, corrections, and paleoerosion rates.

4.4.1. ^{10}Be measurement.

Our in situ cosmogenic ^{10}Be concentration results for the Valmiki sand range from 600 to 13,000 atom/g. Most concentrations are lower than the modern Narayani sand at the MBT Outlet (Fig. 12, Tab. S7). Our concentrations decrease with sample age, as expected from ^{10}Be radioactive decay. One-sigma uncertainties are 29% on average. With values between 8 and 64%, our errors are higher than previous studies on modern Himalayan sand (Lupker et al., 2012a). Total uncertainties mainly derive from 22% analytic uncertainties on measured ^{10}Be/^{9}Be. Measured ^{10}Be/^{9}Be is on average an order of magnitude larger than the analytic blank. However, for a few samples, measured ^{10}Be/^{9}Be can be as low as only five times the blank. Because we anticipated low concentrations for the old samples, we dissolved large quartz mass (Methods in § 3.4.). This resulted in larger natural ^{9}Be content in the targets measured by AMS, less efficient chromatographic elemental separation, and lower AMS current. All these factors impacted uncertainties.

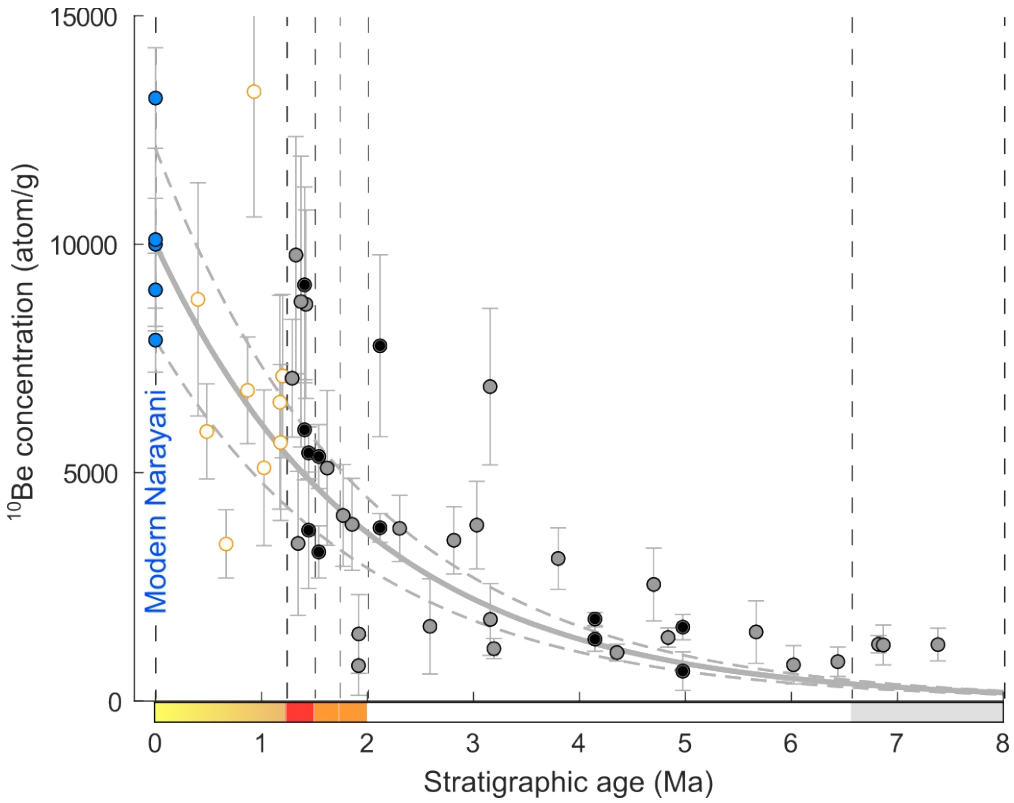

Fig. 12. Measured ^{10}Be concentrations in quartz fractions (either 125-250 or 250-500 µm) of our sandy samples of the Section. Orange-contoured circles: recycled Siwalik sediment. Black-filled circles: samples with duplicate measurements (Tab. S8) for similar or distinct grain size. Blue-filled circles: modern values for the Narayani downstream the MBT (Lupker et al., 2012a). The theoretical concentration derived from the mean value of these modern concentrations by including radioactive decay is indicated by the gray curve. The dashed curve represents one-sigma uncertainties.

Our duplicates show limited reproducibility. Errors are higher than 29% and two duplicates on three differ from each other at one-sigma (Fig. S8). Most duplicates are from sand of different grain sizes. Coarser fractions do not have systematically lower concentrations. As the difference of concentrations between distinct grain-size fractions of modern sand is limited to 15% (Lupker et al., 2012a), we suppose that undetermined causes distinct from grain-size affected reproducibility for our samples. Alternatively, rather low AMS Be currents (Tab. S7) for some of these duplicates might explain limited reproducibility. However, no systematic bias due to low currents was detected. And we do not detect a link between deviation from the mean trend and the mass of dissolved quartz for the ^{10}Be analysis (Fig. S9).

4.4.2. Assessment of the ^{10}Be contribution due to exposure in the Ganga Plain.

We determined the ^{10}Be contribution due to exposure after the sediments left the mountain outlet and before their complete shielding after burial. This sediment transfer ^{10}Be contribution to the initial ^{10}Be paleoconcentration ranges from 1,100 to 2,100 atom/g with one-sigma uncertainty of +30 / -25% on average (Fig. S10b, Tab. S8). The sediment transfer contribution and the associated correction depend on three parameters among others in our model: (1) the megafan width, which determines the interval between deposition and remobilization during sediment transfer; (2) the paleodistance to the front with a higher correction for older sediment deposited farther from the front; (3) the initial depth of deposition before final burial. The late burial contribution depends on this later parameter and is maximal for the samples younger than 1.25 Ma, deposited in thin layers of overbank deposits. To the contrary, the sediment transfer contribution increases on average with age, due to more distal position and associated longer transfer time in the plain.

This component due to exposure in the Ganga Plain represents between 10 and 20% of modern ^{10}Be concentration at MBTO (10^4 atom/g) and is lower than our average analytic error.

4.4.3. Assessment of the ^{10}Be contribution due to Siwalik exhumation: ^{36}Cl measurement results and model.

We obtained 10 sample fractions enriched in feldspar. Fractions had 5 to 50% of remaining quartz. A batch separated by flotation contained half K-feldspar and half Na-dominant plagioclase. A second batch separated by density mainly contained K-feldspar. Our ^{36}Cl concentration results in feldspar average at 7,300 atoms/g and 12,100 atoms/g in the first and second batch, respectively (Tab. S10). Using the radiogenic production model, we calculated a radiogenic component averaging at 82% of the ^{36}Cl content in feldspar and ranging from 50 to 116%. The cosmogenic component includes the components from the following pathways: nucleogenic, muogenic, thermal and epithermal capture on ^{35}Cl. By subtraction of the ^{36}Cl concentrations by the radiogenic component, we obtain a cosmogenic component limited to 18% on average. The cosmogenic component is similar in the first and the second batch, because the higher nucleogenic ^{36}Cl production rates in the second batch (due to higher K content) counterbalance a higher radiogenic component resulting from a higher Cl content (46 ppm vs. 31 ppm on average for the second and first batch respectively). Due to its very small contribution, the cosmogenic component is affected by a high uncertainty. Furthermore, for two samples, we calculated a radiogenic content equal to or higher than the total ^{36}Cl concentration, which results in a negative value of the cosmogenic component for these

samples. This seems caused by an overestimation of the radiogenic contribution, due to currently still unknown reasons.

Using Eq. SI.4 (Supplementary Information § S3.7.2.), we calculated the cosmogenic component of the ^{36}Cl concentration which corresponds to the recent exposure due to Siwalik exhumation. The ^{10}Be contribution due to recent exposure (called recent ^{10}Be contribution) varies between 0 (or negative values) and 2,000 atom/g and averages around 500 atom/g (Fig. 13, Tab. S11). Using our simplified model of production due to recent exhumation (Eq. 3, § 3.7.2.), we calculated an average erosion rate of ~6 mm/y to account for this average ^{10}Be contribution of 500 atom/g. This average erosion rate is consistent with the response to the long-term uplift rate of the EVF fold that we estimated based on published work (see discussion § 5.1.). However, the recent ^{10}Be contributions present a wide dispersion around 500 atom/g, and we observed highly variable recent erosion along the channel banks during the field trips. This suggests that each sample may have recent erosion rates that substantially deviate from 6 mm/y, with recent erosion rates locally below 2 mm/y (Fig. 13).

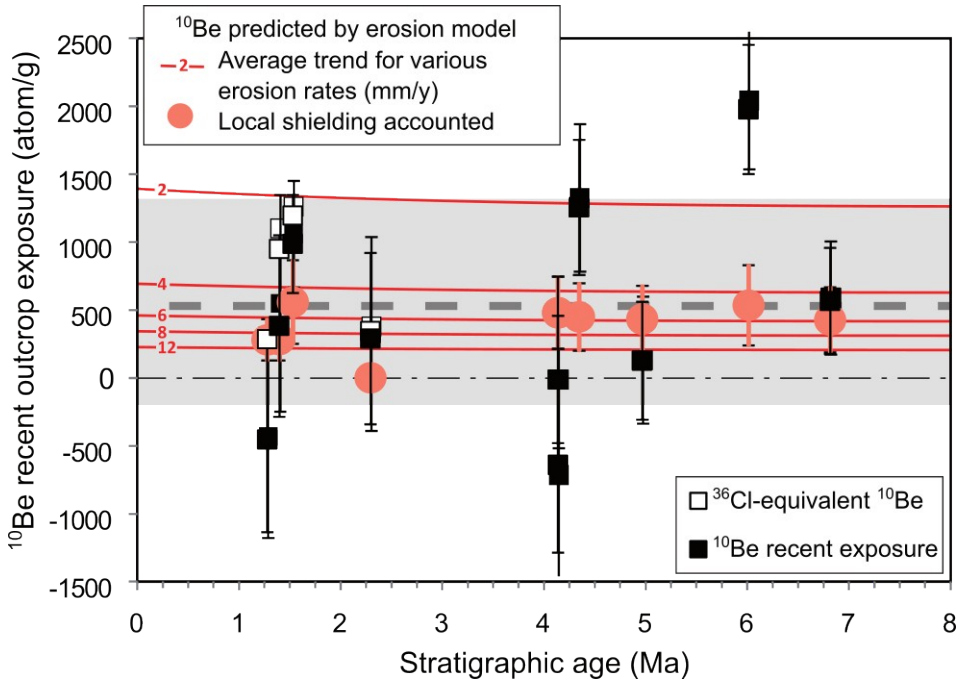

Fig. 13. Estimate of the ^{10}Be accumulated during recent exhumation along the Dwarda valley. For ten sandy samples, we derive this contribution from ^{36}Cl measurement in feldspar using the simplified Eq. 2 (§ 3.6.1.) (open squares) or the corrected Eq. SI.11a (§ S3.7.2.) (black-filled squares). Negative values result from theoretical radiogenic contribution (^{36}Cl produced by radiogenic-induced neutron capture on ^{35}Cl) larger than measured ^{36}Cl content. The red curves correspond to ^{10}Be produced by our steady surface erosion model Eq. 3 (§ 3.6.2.) for 2 to 12 mm/y

erosion rates. The ^{36}Cl-derived values fall for 70% within the one-sigma range of this model and their mean value (~500 atom/g = gray dashed line) corresponds to ~5 mm/y erosion rate. This model includes uniform topographic shielding factor, and density increases with burial depth. Conversely, the pinky orange-filled circles correspond to the model result for the ten individual samples including shielding factor based on the sampling site geometry and indications on recent cliff collapse or major erosion (Fig. S2, Tab. S8). Error bar: one-sigma uncertainty produced by a bayesian exploration for erosion rate randomly varying between 2 and 12 mm/y.

In the following, we applied our recent exhumation model (Eq. 3) to all our samples with a high uncertainty in the recent erosion rates of the sampled banks, with equiprobable values between 2 and 12 mm/y, to account for the average value and the high dispersion of recent ^{10}Be contribution derived from ^{36}Cl. Including a factor when recent bank erosion is visible, our model predicts a recent ^{10}Be contribution ranging from 0 to 500 atom/g, up to 1,500 atom/g for the 97.5% confidence interval (Fig. S10, Tab. S11). For young samples, the recent ^{10}Be contribution represents 0 to 15% of the mean ^{10}Be concentration in modern Narayani sand (10^4 atom/g). But for samples older than 6 Ma, the recent ^{10}Be contribution represents more than 100% of the mean Narayani ^{10}Be concentrations, after the initial concentration substantially decreased by radioactive decay (Fig. 14b). Consequently, the correction for exhumation substantially impacts the calculation of ^{10}Be paleoconcentrations in our samples older than 6 Ma, and substantially increases their uncertainties.

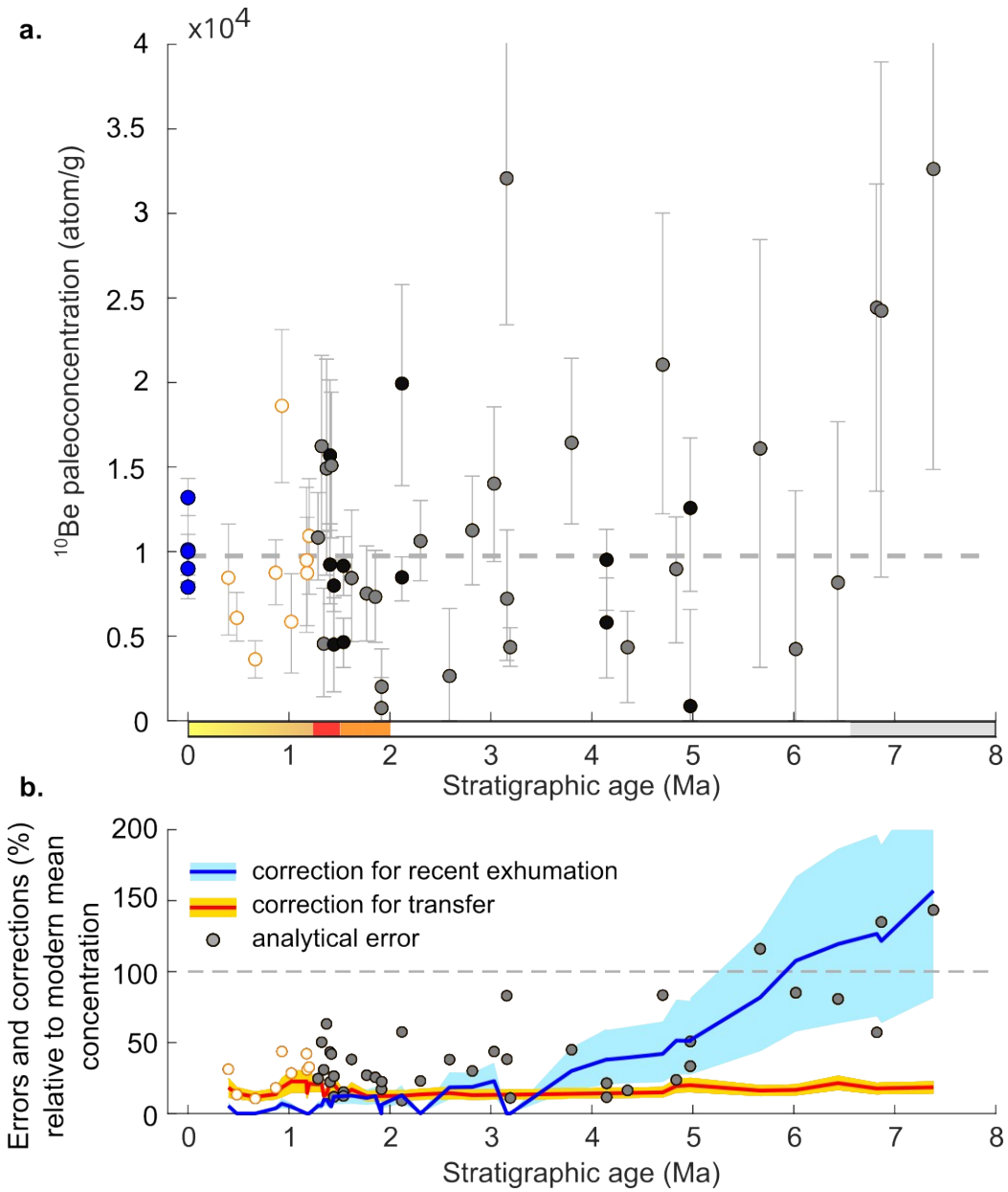

Fig. 14. a. Final ^{10}Be paleoconcentrations after applying plain transfer and recent exhumation exposure corrections. Error bars: one-sigma deviation from median value. Orange-contoured circles: recycled Siwalik sediment. Black-filled circles: samples with duplicate measurement for similar or distinct grain size. Blue-filled circles: published modern samples for the Narayani downstream the MBT (Lupker et al., 2012a). **b.** Comparison of the amount of analytic error or corrections for exposure during plain transfer and during recent exhumation. Values expressed as ratios to the modern concentration in the Narayani sand (~10,000 atom/g).

4.4.4. Paleoconcentrations reflecting the Himalayan erosion and paleoerosion rates.

We calculated the ^{10}Be paleoconcentrations reflecting past Himalayan erosion and our results range from 700 to ~32,000 atom/g. Our paleoconcentrations distribute around the modern concentrations of the Narayani sand (~10,000 atom/g) and do not show any long-term trend (Fig. 14, Tab. S8). The paleoconcentrations dispersion reflects the dispersion of ^{10}Be uncorrected concentrations. Our corrections for sediment transfer and recent exhumation noticeably impact the low-concentrated samples, as highlighted by some paleoconcentrations of a few thousand atoms per gram only, well below modern Narayani concentrations. Contrastingly, the three samples older than 6.5 Ma retain high paleoconcentrations even after subtracting our corrections, but with large uncertainties.

Recycling very likely impacted the samples younger than 1.25 Ma recycling (orange circles Fig. 14). Consequently, we assumed that the ^{10}Be concentrations of these young samples do not reflect the erosion of the Narayani Catchment. We excluded these samples from the calculation of paleoerosion rates (justification § 5.2.1.). For the samples older than 1.25 Ma, we calculated paleoerosion rates assuming that the average ^{10}Be production rate of the Narayani Catchment has remained roughly stable since 7.5 Ma (discussion § 5.1.).

We calculated paleoerosion rates for the Narayani Catchment between 7.5 and 1.25 Ma (Fig. 15, Tab. S8). Our results are more dispersed than modern erosion rates (Lupker et al., 2012a). Four samples, Dwcos8, Dwcos44, Dwcos11 and Dwcos33 (fraction 140-280 μm), have so low paleoconcentrations that calculated paleoerosion rates reach 5 to 22 mm/y. Among these four samples, Dwcos8 and Dwcos44, collected in the same stratum at 1.9 Ma, show paleoconcentrations five times lower than the average paleoconcentration for the 2-6 Ma period. These two samples confirm that some concentrations in the sediment record cannot be explained in a context of steady erosion and are translated into unrealistically high erosion rates compared to average rates. In the following, we consider that such high erosion rates averaged on the Naryani Catchment are unlikely and we arbitrarily cap our paleoerosion rate values by 5 mm/y (discussion § 5.2.3.).

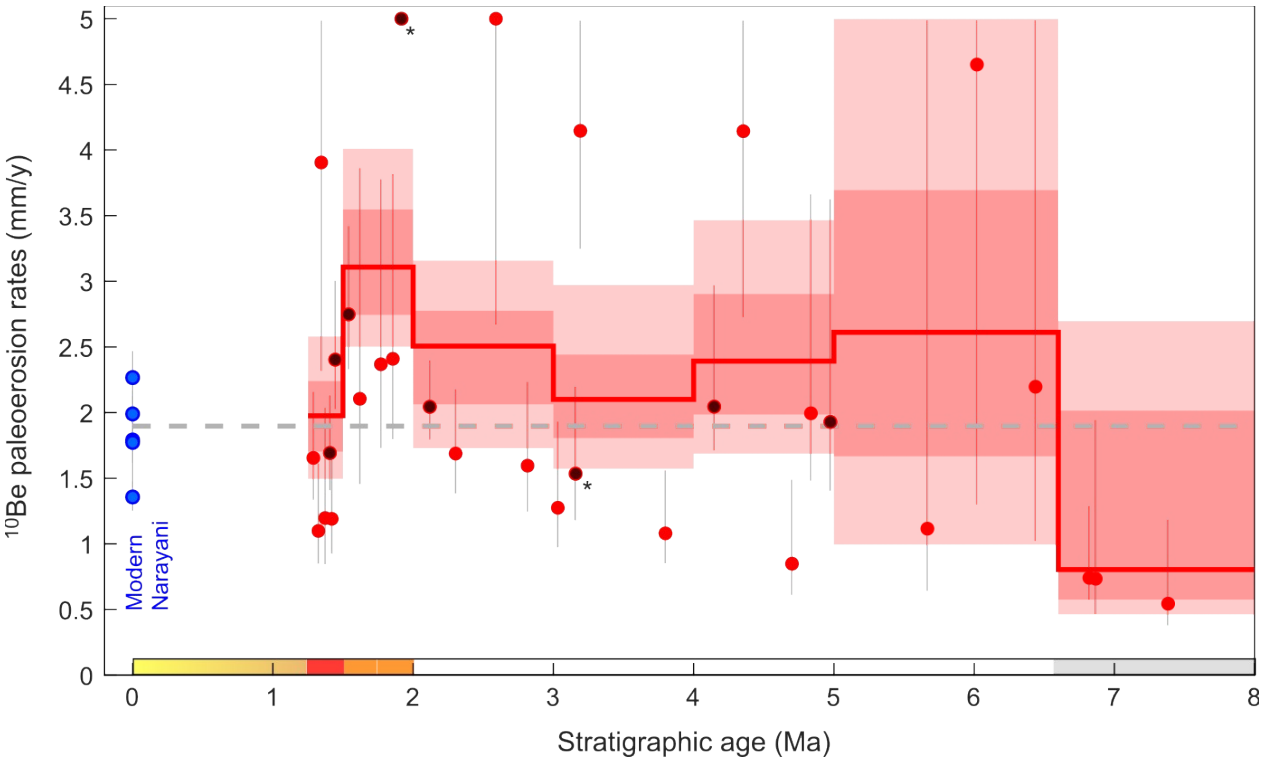

Fig. 15. ^{10}Be paleoerosion rates derived from the ^{10}Be paleoconcentrations assuming a steady production rate in the Narayani Catchment. Erosion rates arbitrarily capped to 5 mm/y (discussion in § 5.2.3.). Error bars: one-sigma deviation from median value. Brownish black-filled circles: mean value of measurements in the same sandstone layer (indicated by the symbol '*') or in duplicates on the same sample (without symbol '*'). Red stepped curve: median value of the Pdf (Probability Density Function) associated to the paleoconcentration averaged during the considered time interval. Dark-red shading: one-sigma deviation from the median. Light-red shading: two-sigma deviation from the median. Blue-filled circles: Published erosion rates from the Narayani sand (concentrations from (Lupker et al., 2012a) but using the production rate that we calculated in this study), with their mean value is extended by the gray dashed line.

To document the average paleoerosion rate trend in the Himalayas and smooth out data dispersion, we compute paleoerosion rates averaged over regularly-spaced intervals (red curve and shaded areas Fig. 15). In addition to the interval limits given by the transitions that we assume to occur at 1.25, 1.5, 2 and ~6.5 Ma, we divided the erosion rate history into 1-My intervals so that each interval contains at least three ^{10}Be concentration measurements. For each interval, we followed a Bayesian approach and derived the Pdf (Probability Density Function) of the mean erosion rate over the interval. We represented the

median value of the average paleoerosion rate and one-sigma uncertainties of this temporal mean erosion rate (quantiles at 16 and 84%). We reduced the samples with two replicates or samples collected from the same strata (Tab. S8, e.g. Dwcos8 and Dwcos44) to one single value by taking the mean of the concentrations. This way, we do not over-represent a given stratum that corresponds to an "instantaneous" erosion rate – we define instantaneous as meaning that the TCN-derived paleoerosion rate integrates less than 1,000 years for the Narayani Catchment. We preferred median paleoerosion rate values to mean values because medians are less sensitive to the 5 mm/y capping erosion rate value.

At first order, the paleoerosion rates that we averaged over intervals have remained steady since 6.5 Ma, at 2.2-2.5 mm/y, close to the mean erosion rate of the modern Narayani River (red curve, Fig. 15). The paleoerosion rate average shows large uncertainties on some intervals. Contrastingly in the Late Miocene, before 6.5 Ma,, the paleoerosion rate average is 3.5 times lower than the post-6.5 Ma record and modern times, at 0.8 (+1.2 / -0.2) mm/y.

At second order, the average paleoerosion rate amounts to 3 mm/y in the 1.5-2 Ma early Pleistocene and is 35% higher than the Pliocene average (Fig. 15). We observe this increase of average paleoerosion rate compared to the Pliocene both in the average value and in the minimum value, which exceeds 2 mm/y. However, we cannot precisely quantify the amplitude of this increase, because of the 5 mm/y capping value of paleoerosion rate for the Dwcos8 / Dwcos44 pair (samples at 1.9 Ma, Fig. 15). Finally, during the 1.25-1.5 Ma period, the average paleoerosion rate falls back to a value close to modern values. This suggests that the early Pleistocene excursion to paleoerosion rates higher than the Plio-Pleistocene mean value was temporary.

5. Discussion.

We presented the previously unstudied Valmiki Section, and our magnetostratigraphic dating, provenance and paleoerosion rate results. We now discuss our dating constraints and their implications on sedimentation rates and fold initiation in the Valmiki setting (§ 5.1.). Before discussing the paleoerosion rate evolution, we show with our major element and Sr-Nd isotopic results that our samples were deposited by the Narayani River for most of the Section, except after 1.25 Ma, and possibly except before 6.5 Ma (§ 5.2.1.). We propose that the catchment-averaged ^{10}Be production rate has remained steady since 7.5 Ma (§ 5.2.2.) and we discuss the potential causes for the apparent broad variability of our paleoerosion rates, either linked to our corrections or to landsliding activity (§ 5.2.3.). We then discuss the possible causes explaining how our paleoerosion rates evolved from 7.5 to ca. 0 Ma (§ 5.3.) and position our results in the context of previous TCN (§ 5.4.1.) and thermochronology (§ 5.4.2.) paleoerosion rate studies.

5.1. The Valmiki sections: Ssedimentation rate, fold initiation and growth rate.

Based on paleomagnetism on regularly-spaced sampling sites, we determined a continuous chronostratigraphic scale of the EVF Section with a steady sedimentation rate from the Late Miocene (8 Ma) to the Pleistocene (ca. 0 Ma) (Fig. 8). A few short-term sedimentation rate variations (Fig. 8) might reflect real variations. Alternatively, they may be artifact caused by the lower resolution of the central part of the paleomagnetic record. With short-term variations excluded, sedimentation rates remain close to 0.5 mm/y, that is at ~0.46 mm/y from 8 to 3 Ma and at ~5 mm/y from 3 to 0.7 Ma, the time of incipient fold growth as detailed below. The Valmiki sedimentation rates are consistent with other sections in Central Himalayas, such as the Surai Section (Appel et al., 1991; Gautam and Rösler, 1999; Corvinus and Rimal, 2001; Ojha et al., 2009; Charreau et al., 2021) and the Bakeya Section (Harrison et al., 1993), displaying rates at 0.44 mm/y after 8 Ma.

Contrasting with those sections, the Valmiki Section has a lower proportion and a smaller thickness of the conglomerate layers, and yields a dating resolution adequate to address the question of the climate change impact on Himalayan erosion rates over the late Pliocene and Quaternary. The Bakeya Section has no sediment younger than 4-5 Ma (Harrison et al., 1993). The Surai Section has weak dating constraints from 4 to 1 Ma, with no constraint after 1 Ma (Charreau et al., 2021), and with no consensus on the magnetic polarity interval definitions (Corvinus and Rimal, 2001; Ojha et al., 2009; Charreau et al., 2021).

Based on our Quaternary constraints and a probable steady sedimentation rate, we discuss the timing of the EVF uplift. The bedding dip flattens in the front of Patalaia and upper Ganguli, which we interpret as growth strata. These growth strata initiate at 0.7+/-0.04 Ma and would mark the inception of the folding of this frontal structure. At the anticline axis near the EVF topographic ridge, the structural uplift reaches ~4,250 m. Therefore, the average uplift rate would have been ~6 mm/y since 0.7 Ma. This value is lower than the Holocene uplift rates of 10 mm/y measured farther east, at the longitude of Kathmandu (Lavé and Avouac, 2000). However, in the Valmiki setting, two structures, the EVF and ESCF, partition Himalayan horizontal shortening (Fig. 2), and this northern fold might absorb some part of regional shortening.

For the WVF, without magnetostratigraphic constraints, we infer fold growth inception from the absorbed finite shortening of 2-2.5 km. Assuming a maximum shortening rate of 21 mm/y for the frontal thrust (Lavé and Avouac, 2000), the fold should initiate before ~0.1 Ma. Because Siwalik deformation in

the WVF setting seems partitioned between the WSCF and the frontal WVF, we assume that the growth of the WVF initiates earlier, at 0.2 or 0.3 Ma.

5.2. Range of application and representativeness of Himalayan erosion rates.

Before discussing our results in terms of the evolution of erosion in the Central Himalayas, we address the questions: (1) Which of our samples are true deposits of the Narayani River? (2) For these samples, have the geometry and elevation of the Narayani Catchment remained steady, or do we need to adjust the catchment-averaged ^{10}Be production rate? (3) What are the potential causes of variation in paleoerosion rates and which signal can we ultimately interpret in terms of variations of tectonic or climatic forcing?

5.2.1. Sample paleolocation relative to the paleo-Narayani Fan.

To reconstruct how paleoerosion rates evolved, we should determine whether our samples were deposited in an environment steadily fed by the same large transverse Himalayan river, the paleo-Narayani River, or by another river.

As the Himalayan wedge has converged towards the Indian continent, the sedimentary facies of the Narayani Fan have migrated southwards across the foreland basin (Lyon-Caen and Molnar, 1985). This migration impacts the relative position and deposition environment of each sample of the Section, as shown by the upward coarsening of sediment grain size (Dubille and Lavé, 2015). We illustrate two critical stages in Fig. 16. (1) The oldest samples might record the transition from the paleo-Karnali Megafan or the paleo-Ganga Megafan to the Narayani Fan deposition environment. (2) The youngest samples probably record the transition of the deposition environment from the Narayani Fan to local alluvial fans fed by Siwalik rivers. This latter transition may be gradual or suddenly triggered by the growth of a new Siwalik front fold, the deviation of the Narayani River, and the shift of the Narayani Megafan apex, as shown by the modern 50 km offset between the Narayani MBT and MFT outlets (Fig. 1-2).

Our major element and Sr-Nd isotopic results combined with our sedimentologic observations yield information about the paleolocation of our samples.

(1) Before 6.5 Ma. The samples are likely deposited by a meandering river, farther from the Himalayan front than for subsequent periods, as shown by dominant siltstone overbank deposits and thin sandstone layers (Facies FA1). The obliquity of the modern Narayani Fan and the location of the deposits (Fig. 16) suggest that samples are deposited on the southwestern margin of the paleo-Narayani Fan drained by meandering channels. We could speculate that the samples are deposited distally by the paleo-Gaghara

River or the paleo-Ganga River in the Ganga Plain. The Sr-Nd isotopes may support this hypothesis: the samples are more Sr-radiogenic than the expected mix of the main lithologies present in the Narayani Catchment, similarly to modern Gaghara or Ganga sand (green ellipse Fig. 10), and they correspond to very low TSS contributions (Fig. 11c). Alternatively, we could interpret our Sr-Nd results as indicating a smaller northward extent of the paleo-Narayani Catchment that might induce an absence of drainage area eroding the TSS.

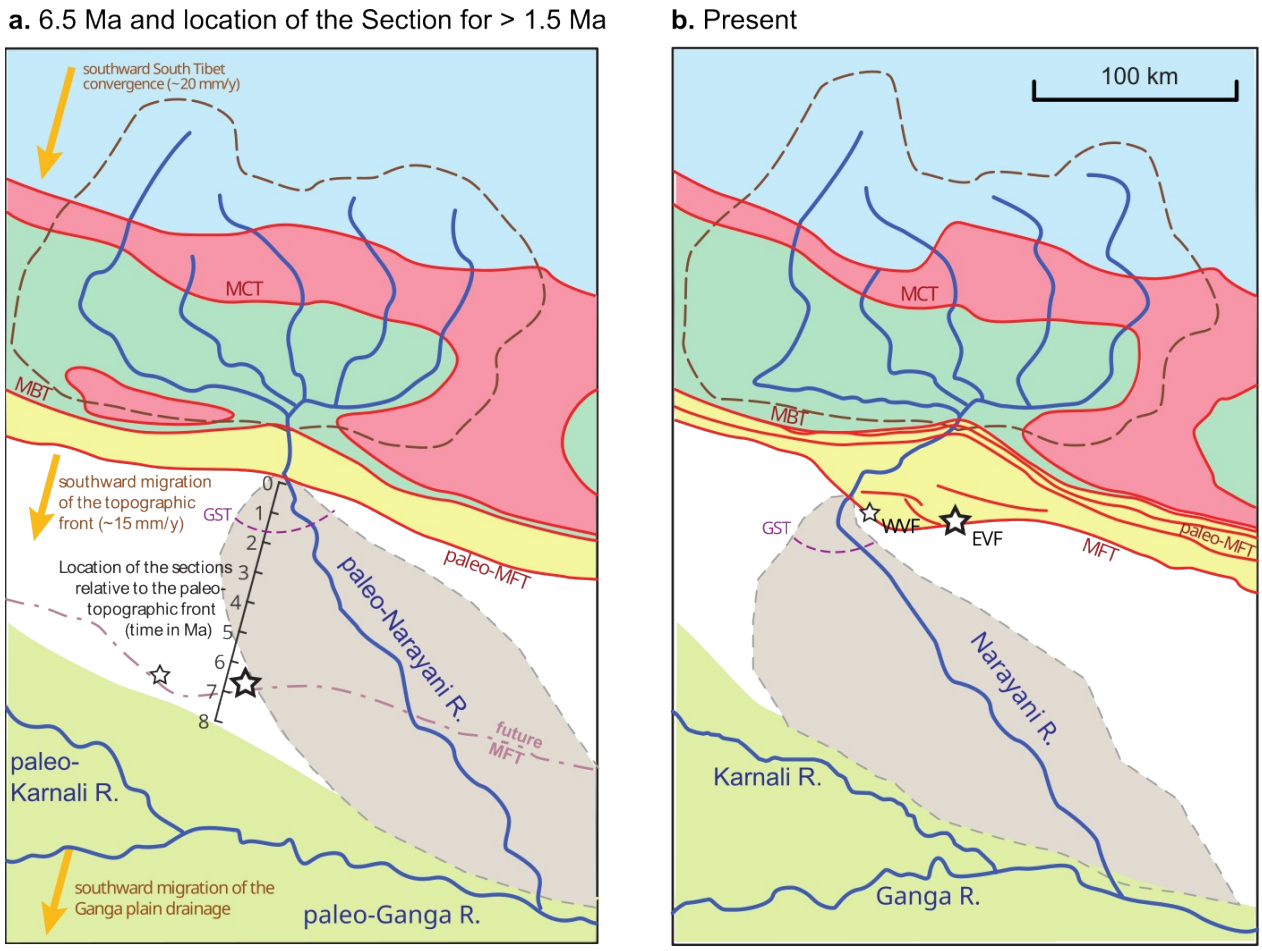

Fig. 16. Evolution of the paleolocation of our samples relative to the Himalayan front and to the Narayani Megafan. **a.** Hypothetical configuration of the foreland basin at 6.5 Ma, with the paleo-MFT, MBT and MCT thrusts. Light brown surface: Narayani paleo-Megafan. Small and big stars: paleolocation of the composite WVF and EVF sections. Line and stratigraphic ages from 8 to 0 Ma: paleolocation of our samples relative to the topographic Himalayan front and to the Narayani paleo-Megafan. Before 6.5 Ma, the location of Narayani outlet is less certain, and the deposition environment might have been the floodplains of the Ganga River or Karnali River rather than the Narayani Megafan (discussion in § 5.2.1.). After 1.5 Ma, the exhumation of the South Chitwan and

Valmiki Folds pushed westward the Narayani outlet and small rivers originating from the Siwaliks Hills, similar to the modern Rapti River, fed our sample sites. This transition may have been gradual, or abrupt in case of a lateral shift of the Narayani outlet due to river deviation by frontal fold growth. **b.** Modern configuration.

---

(2) From 6.5 to 1.5 Ma. The samples are probably deposited in the central part of the paleo-Narayani Fan by a braided river of varying depth, as shown by facies dominated by weakly weathered thick sandy beds (Facies FA2 and FA3). Most elemental ratios are similar to modern Narayani sand. At second order, Na/Si averages at 0.03, lower than for modern Narayani sand at 0.04. This Na depletion suggests partial plagioclase weathering during sediment transfer through the plain (Lupker et al., 2012b) or during pedogenesis and diagenesis, including alteration during the Siwalik exhumation.

(3) From 1.5 to 1.25 Ma. Our samples are deposited closer to the Himalayan Front. Controlled by Siwalik folding, the location of the fan outlet at the MBT or MFT has a stronger impact on sample location related to the paleo-Narayani Fan. The samples can be in the sandy to conglomeratic deposits in the paleo-Narayani Fan axis, or in a lateral position at the northern margin of the paleo-Narayani Fan. Our major element and isotopic results do not depart from the values of the 6.5-1.5 Ma period. However, some samples collected in strata with variegated, orange-weathered siltstone layers present lower Na/Si ratio, despite normal ratios for other elements (except Ca). This suggests deeper plagioclase-weathering (Fig. 9). These variably weathered facies are made of overbank deposits (FA4) interbedded with conglomeratic layers that include well-rounded granitic pebbles. We interpret these facies as the transition to a more lateral position in the Narayani Fan. The Narayani River, or one of the channels in its braided course, visits and deposits sediment more rarely in this part of the fan, inducing longer near-surface residence times and deeper weathering for our samples.

(4) After 1.25 Ma. Depressed elemental ratios mark this period, with particularly a low Al/Si and a very low Na/Si. This depleted signature is similar to the signature of sand deposited by modern local rivers that drain the Siwalik Hills (Fig. 9), in other words recycled Himalayan sediment, and to the sand of the top of the Surai Section (Charreau et al., 2021). Concurrently, granitic pebbles probably from the lithologic High Himalayas (HH) are present before 1.25 Ma but disappear by 1 Ma (Fig. 5e). These two facts suggest that the Narayani River stops depositing sand in the area of the Section. Thus, samples younger than 1.25 Ma were likely deposited by local rivers draining the Siwaliks Hills. These rivers alternately deposit overbank sediment and thin conglomeratic layers. Red weathering in FA5 facies (Fig.

5c) reflects the lower lateral mobility and much shallower channel depth of these local rivers, as well as reduced subsidence due to local synfolding sedimentation.

Recycled sediment was produced by the development of the Siwalik Hills that impacted the course of the Narayani River (Divyadarshini and Singh, 2019) and the location of the Narayani Fan (Fig. 2, 16). Structural and magnetostratigraphic data suggest that frontal growth of the EVF and WVF initiates lately at ca. 0.7 and ca. 0.4 Ma, respectively. However, the uplift of the northern WSCF and ESCF folds may start earlier, probably at 1 to 1.25 Ma. The growth of the WSCF folds would deflect the Narayani westwards and pin the river at its current MFT-outlet. Whatever the folding and diversion scenarios, the samples younger than 1.25 Ma do not derive from the geographic HH, nor from the Narayani Catchment above the MBT-outlet. For this reason, we exclude these samples from our reconstruction of Himalayan paleoerosion.

5.2.2. Geometry and elevation of the paleo-Narayani Catchment.

In dynamic settings such as the Himalayas, horizontal advection fosters drainage evolution (Bonnet, 2009). Consequently, the question of the extent of the Narayani Catchment over long time scales is particularly acute. Because of a steep topographic gradient north to south of the Himalayas, a possible variation of northern extent of the catchment may impact sediment ^{10}Be concentrations and paleoerosion rates in the Siwaliks.

At first order, our major element and most of our Sr-Nd isotopic results suggest contributions steadily dominated by lithologic HH relative to LH, similar to modern and late Pleistocene Narayani sand (Morin, 2015). The proportions between LH and HH appear steady on average over the entire period. This suggests that the paleo-Narayani River has drained the geographic High Himalayas since the late Miocene. However, the relative proportions of HHC and TSS display variability. This variability might reflect changes in the catchment extension. Alternatively, because the variations are rapid and transient, the northern TSS-dominant flank of the geographic High Himalayas and the southern HHC-dominant flank may have supplied varying relative contributions to the erosion flux. Hereafter, since the HHC/TSS proportions are steady on average at first order, we consider that the catchment extent remained steady from 6.5 to 1.25 Ma.

Before 6.5 Ma, we proposed (§5.2.1.) varied interpretations of the relative proportion of TSS near 0%, which invite us to consider the paleoerosion rates before 6.5 Ma cautiously.

In addition to a varying extent of the Narayani Catchment, at least three other variations may affect ^{10}Be production rates and paleoerosion rates: (1) topographic elevation change knowing that production rates are quite sensitive to elevation; (2) glacial cover, since we set production rates for subglacial sediments to zero due to the ice shielding the cosmic flux; and (3) the magnetic dipole variations, which

we previously showed that the variations may have little impact (Lenard et al., 2020). With regard to elevation change, the Himalayas are an orogenic wedge at first approximation (Hilley and Strecker, 2004). The mean elevation of a triangular wedge only depends on the elevation of the rear part of the wedge. Here, this rear part is South Tibet, which elevation has remained steady since the Late Miocene (Garzione et al., 2000; Gébelin et al., 2013). Consequently, we assume that the mean Himalayan elevation has not varied substantially. With respect to ice cover evolution, the Narayani Catchment may have had up to 20% ice cover during glacial periods (Shi, 2002), compared to 9% today (Raup et al., 2007), with an Equilibrium Line Altitude (ELA) lowered by an amount of 500 m up to 1,000 m along the northern and southern flanks respectively (Gayer et al., 2006; Asahi, 2010). In a catchment in Western Himalayas, such ELA depressions modified ^{10}Be production rates by at most 28% (Kapannusch et al., 2020). Applied to paleoconcentrations, this modification remains lower than our uncertainties. Such modifications may have had a higher impact on the 0-0.8 Ma period, characterized by maximum glacial extent but our samples do not record that period. For simplicity, we will not account for production rate changes due to glacial cover.

To summarize, we consider that the potential variations of production rates are lower than our ^{10}Be paleoconcentration uncertainties. We assume that the contributing catchment was the Narayani Catchment and that the ^{10}Be production rates in this catchment have remained steady, close to modern values since 7.5 Ma.

5.2.3. Variability of paleoconcentrations and paleoerosion rates.

At first order, our ^{10}Be paleoerosion rate reconstruction shows steady average erosion rates in the Central Himalayas after 6.5 Ma. At second order, ^{10}Be paleoconcentrations and derived paleoerosion rates show rapid variations and a large dispersion. Paleoconcentration dispersion around a mean of 10^4 atom/g goes from a factor one-fifth to three. This dispersion does not prevent a first-order interpretation as shown by paleoerosion rates averaged over 1-Ma intervals. Nevertheless, we discuss the origin of these variations and their geological meaning. The low reproducibility of our ^{10}Be measurements may partly explain dispersion. But the associated amplitude, between one half and two, suggests that other processes could also be invoked to fully explain the dispersion.

Impact of corrections for sediment transfer and recent exhumation on erosion rate variability.

Corrections for TCN production during sediment transfer and during recent exhumation affect paleoconcentrations, with a high impact on the very low TCN concentrations.

The sediment transfer correction does not correlate to sample age and appears limited to ~20% of the mean paleoconcentration of 10^4 atom/g. The sediment transfer correction may therefore not be the cause of the broad dispersion of the paleoconcentrations. However, the sediment transfer model only provides mean values and does not allow estimating variability. We assumed that the Narayani Fan had a steady width over time, but this may be untrue. For instance, the fan had shorter width over the last few hundred years compared with its long-term width (Pati et al., 2011). Consequently, we could challenge our model's assumption that the paleo-Narayani River visited any point of its fan at the same frequency. If the paleo-Narayani River visited the lateral parts of its fan less frequently than the central part, samples would be subject to longer exposure time in the Ganga Plain and larger corrections should be necessary. However, we lack long-term data on the fan dynamics, and on the geochemical signature of deep weathering at the fan surface, which could be identified in the major element signature of samples. This prevents us to estimate the maximum variations of the sediment transfer correction.

The correction associated to ^{10}Be production during recent Siwalik exhumation affects the oldest samples, with an average correction above 100% of an initial paleoconcentration of 10^4 atom/g for samples older than 6 Ma. We had the initial goal to determine this production from ^{36}Cl concentrations only. But the result is imprecise. We even have two negative values for equivalent recent exposure times, due to low ^{36}Cl concentrations and high uncertainties on the radiogenic component (§ 4.5.). To overcome this problem, we assumed steady-state incision of the Dwarda Channel and designed a simple model compatible with ^{36}Cl measurements. However, this model is a rough approximation because incision and lateral erosion rates may be variable and discontinuous, as suggested by (1) several strath terraces (Fig. S2) along the middle and lower Dwarda Valley, (2) local bank erosion by small landslides, or (3) the dispersion of the ^{36}Cl-based correction around the average value. Reduced erosion rate at the level of a resistant layer can therefore induce large ^{10}Be contribution due to recent exposure. In our corrective model, this would imply an underestimation of paleoerosion rates. In contrast, a recent but undetected bank erosion by a landslide would lead to an overestimation.

Geomorphologic sources of paleoerosion rates variability.

High values of paleoconcentrations can be explained by a weaker than average erosion of the bank or by long lasting exposure on top of the Narayani Fan. Conversely, these two corrections cannot easily explain very low paleoconcentrations for samples younger than 4-5 Ma. A geomorphologic cause should be invoked.

Large-amplitude variations of ^{10}Be paleoerosion rates have been previously observed in the Himalayas (Puchol et al., 2017; Dingle et al., 2018; Lenard et al., 2020; Mandal et al., 2021) and elsewhere (Amidon et al., 2017; Oskin et al., 2017; Mariotti et al., 2021). Variations were interpreted as

resulting from climate change and maximum glacial extension (Mariotti et al., 2021), from tectonics and duplexing process cycles (Mandal et al., 2021), or from geormophologic processes related to catchment evolution (Amidon et al., 2017). For the Dwarda, we cannot easily link the rapid and ample paleoconcentration variations to one of these causes. We do not formally reject an origin linked to high frequency climatic cycles for instance the Milankovitch cycles, but we cannot detect it, possibly because of aliasing issues and a lack of sampling resolution. The absence of correlation with Sr-Nd isotopic or geochemical signature variations does not favor such interpretation.

Alternatively, some of our samples may integrate products from transient – not in steady state – erosion processes such as mass wasting, particularly for samples with erosion rates above 5 mm/y. In the Himalayas, low concentrations in sediment may result from a large input of material issued from active landslide areas (Puchol et al., 2014), or from the supply of numerous co-seismic landslides (Wang et al., 2017). Theoretically, landslide stochastic inputs are gradually smoothed out downstream, but smoothing depends on the size of the catchment. The critical size over which smoothing operates depends on the maximum size of landslides: for a surface of 1 km^2 and a volume of 0.05 km^3, the critical size is around 100 km^2 (Niemi et al., 2005; Yanites et al., 2008). In the Himalayas, some giant rockslides have produced several km^3 of sediment (Lavé et al., 2023; Weidinger et al, 2006). For them, the critical catchment size may be larger than 10,000 km^2, as also indicated by the existence in the Narayani Fan of sediment with a mineralogical signature indicating a contribution occasionally dominated by the products of a giant rockslide (Lavé et al., 2023).

If sediment supply is dominated by a giant landslide or by numerous coseismic landslides, the Narayani sediment does not result from erosion products mixed in proportions related to their relative background erosion rate from all parts of the drainage basin – "background" meaning unrelated to landslides. In other words, erosion is not at steady state over the whole contributing basin, and the hypothesis for the use of (Eq. 1) is no longer valid. Consequently, we assume that these very low concentrations/high erosion rates do not represent erosion rates averaged throughout the catchment. For that reason, we arbitrarily cap these values at 5 mm/y, a value which is unlikely at the outlet of large Himalayan catchments (Lupker et al., 2012a; Kapannusch et al., 2020). This maximum value partly affects our average paleoerosion rates for the 1.5-2 Ma and 2-3 Ma intervals.

5.3. Evolution of erosion rates in Central Himalayas.

Despite their large uncertainties of 40% at one-sigma, our ^{10}Be paleoerosion rates along the Valmiki Section provide original and relatively constraining information on the erosion of Central Himalayas since the Mio-Pliocene transition. Combined with our geochemical and isotopic data, they allow us to draw up the evolution of the mean erosion rate in several phases.

From 7.5 to 6.5 Ma, paleoerosion rates are very low, 0.8 (-0.2 / +1.2) mm/y, compared to the next periods or to modern times. Large paleoerosion rate uncertainties, together with uncertainties in sediment provenance, do not ease the interpretation the low paleoerosion rates, and call for further investigation.

From 6.5 to 2 Ma, average erosion rates are ~2 mm/y. The HH/LH contributions remain relatively stable and indicate climatic and tectonic forcing similar to the modern Narayani Catchment. Our data suggest that the tectonic Himalayan wedge may have reached a steady erosional behavior since at least the early Pliocene. Second-order cyclic variations of the Si content and $^{87}Sr/^{86}Sr$ signature suggest cyclic LH/HH relative contributions with a period of ~2 My (Fig. S11, an increased LH contribution leads to more radiogenic and SiO_2-enriched sediment). This could reflect the cyclic activation of a new duplex on the Main Himalayan Thrust (MHT) (Lavé and Avouac, 2001; Bollinger et al., 2004; Grandin et al., 2012), or an out-of-sequence cyclic reactivation of the Main Central Thrust (Hodges et al., 2004). Farther west, (Mandal et al., 2021) have interpreted near-cyclic variations in paleoerosion rates with a period of ~1 My as the erosive response of the topography due to cyclic duplex accretion along the MHT. However, in the Valmiki Section, we do not observe such ^{10}Be paleoconcentration cyclic variations and any correlation with geochemical and isotopic variations. Therefore, based on our dataset, we can difficultly identify the response to an occasional in-depth activation of new ramps in depth or a reactivation of the MCT. However, the steady mean erosion rates and provenance during this period allow us to reject any major tectonic change in the tectonic evolution of the Himalayas, in agreement with thermochronologic modeling (Robert et al., 2009; Herman et al., 2010).

From 2 to 1.5 Ma, provenance and paleoerosion rates rapidly change. Several indicators jointly suggest that the Quaternary Glaciations impacted erosion patterns: (1) a 35% increase in average erosion rates from 2 to 3 mm/y as compared to the Pliocene, (2) the highest HH/LH contributions of our full record, (3) the increase in the TSS contribution at the start of this period (Fig. 11), and (3) Na-rich sediment probably derived from leucogranitic outcrops, mostly located at the level of the summits of the HH. As climate cooled down during the Quaternary, lower temperatures and their fluctuations around 0°C fostered an increased contribution of frost-weathering and periglacial sediment at high elevation (Rempel et al., 2016; Scherler, 2014; Banerjee and Wani, 2018). The Quaternary Glaciations also promoted the development of upper valley glaciers in the Himalayas. Frost cracking along hillslopes and valleys lowering by glaciers, which erosive effectiveness has been documented elsewhere (Hallet et al., 1996; Herman et al., 2013), may have greatly increased landscape erosion in the High Himalayas.

The last period, from 1.5 Ma to present, is documented by the Valmiki Section only from 1.5 to ~1.25 Ma, after which the section does not record a pristine paleo-Narayani signature. For the more recent time, we have the modern signature in the Narayani sediment and the one of the last interglacial-glacial transition (0-40 ka) within cores drilled into the Narayani Fan (Morin, 2015). The three records, modern

sediment, late Pleistocene cores and the 1.5-1.25 Ma part of the Valmiki Section have similarities in major element composition and ^{10}Be-derived paleoerosion rates. Therefore, we assume that paleoerosion rates during the undocumented period between 1.25 Ma and 40 ka could have remained similar on average.

Accordingly, after 1.5 Ma, paleoerosion rates, major element ratios, and HH/LH contributions would have returned to values similar to the Pliocene. The excursion to higher erosion rates between 2 and 1.5 Ma would have then been temporary. No known climatic or tectonic event at ~1.5 Ma could explain this rapid return to previous erosion patterns. We speculate that this return might be caused by a hysteresis between glacial development and efficiency of glacial erosion (Pedersen and Egholm, 2013). At the beginning of glaciations, glaciers carve a pre-existing fluvial landscape. They are initially in strong disequilibrium with the long profile and shape of valleys, promoting enhanced erosion. Subsequently, during the middle Quaternary, the U-shaped and upper flat-bottomed valleys inherited from earlier glacial cycles no longer produce as much subglacial erosion. The moderate impact of the last glaciation on erosion as recorded in a formerly glaciated catchment in the Western Himalayas (Kapannusch et al., 2020) is consistent with a lower glacier erosive activity during the Middle and Late Quaternary.

5.4. Consistency with former estimate of paleoerosion rates in Central Himalayas.

5.4.1. Comparison with other ^{10}Be-paleoerosion rate records.

The record from the Valmiki Section provides new insights on ^{10}Be-derived paleoerosion rates in the Central Himalayas. At the scale of the whole range, it complements published records (Fig. 17): (1) the sections as proximal records at the front of the paleo-Yamuna River (Mandal et al., 2021) and the paleo-Karnali River (Charreau et al., 2020), west of the Valmiki Section, and (2) the distal record of the Bengal Fan integrating erosion across the Central and Eastern Himalayas, drained by the Ganga River and Brahmaputra River (Lenard et al., 2020). While the Bengal Fan records a complete erosive history during the Quaternary, the paleo-Yamuna and Karnali records do not cover this period and stop at 2 and 3.5 Ma. Modern erosion rates in these two catchments can be compared to late Pliocene values and provide a trend.

The four records (Fig. 17) display several common features. Average paleoerosion rates appear steady in the Himalayas since 6.5 Ma. None of the four records support any major (two or three-fold) and permanent increase in erosion rates. None of the records support a permanent impact of the Quaternary Glaciations on erosion rates in the Himalayas, since modern erosion rates are systematically equal or lower than Pliocene paleoerosion rates.

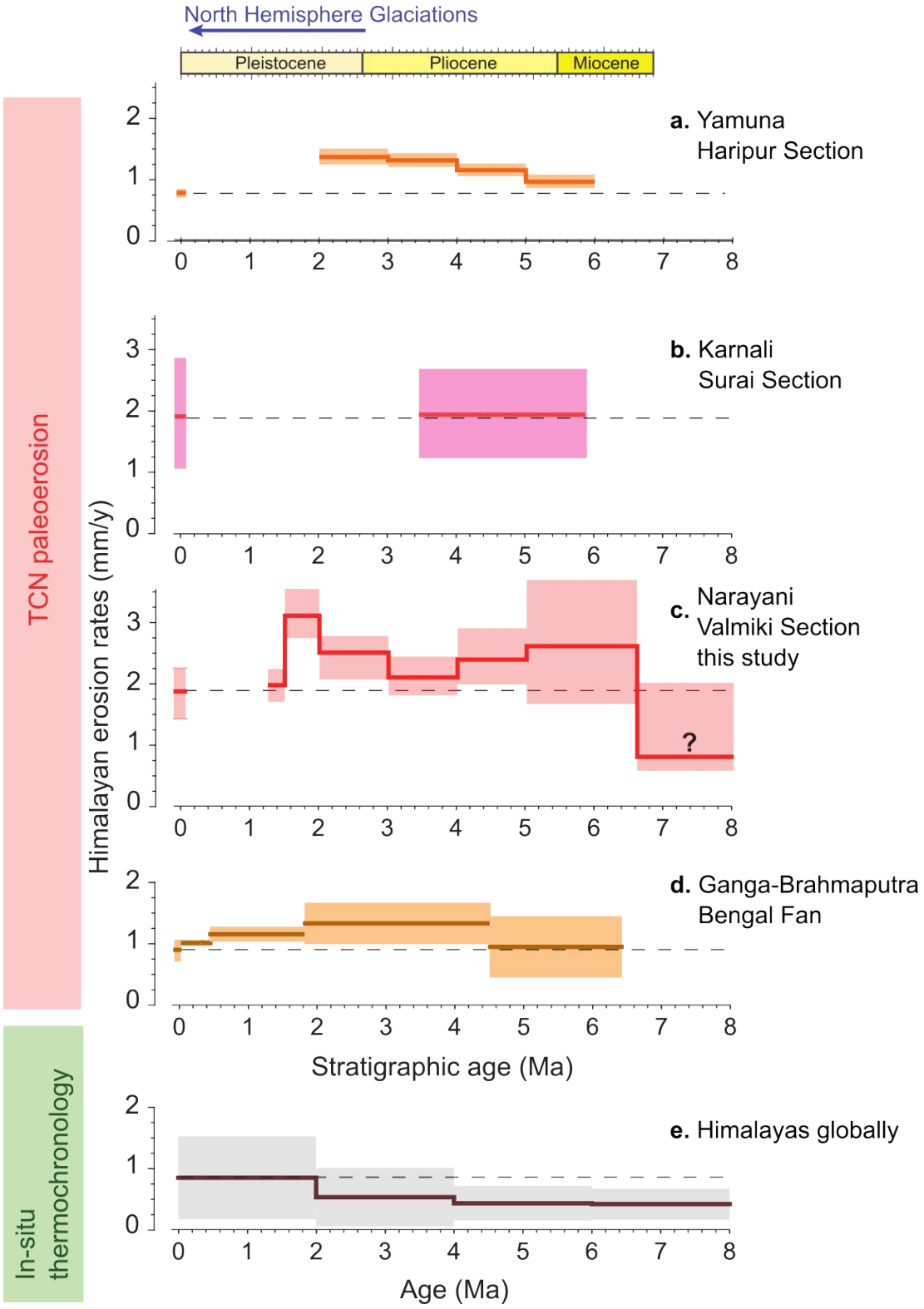

Fig. 17. Synthesis of paleoerosion records in the Himalayas.

Average trends and 1-sigma deviations of the ^{10}Be-derived paleoerosion rates presented by time-intervals for (**a**) the Haripur section (Mandal et al., 2021), (**b**) the Surai Section (Charreau et al., 2021), (**c**) the Valmiki Section (this study), (**d**) the Bengal Fan (Lenard et al., 2020). (**e**) Erosion rates obtained from a compilation of in-situ thermochronology (Herman et al., 2013). The ^{10}Be-derived signal for major transhimalayan rivers (Yamuna R., Karnali R. and Narayani R.) as well for the whole Ganga-Brahmaputra catchment indicate: (1) No permanent increase in erosion rates synchronous with the onset of the Northern Hemisphere Glaciations, in contrast with the thermochronologic signal (2) Pliocene erosion rates higher or equal to modern rates, (3) Local transient increase in erosion rates, detected so far in the Narayani Catchment, but not at broad scale, and possibly related to the onset of Early Quaternary glacial erosion in the Himalayas.

At second-order, based on our new Valmiki Section, the Quaternary Glaciations may have transiently impacted paleoerosion rates in the Central Himalayas in the Middle Quaternary from 2 to 1.5 Ma. The Bengal Fan does not record this transient impact. It is unlikely that a transient signal originating from the Central and Eastern Himalayas and lasting 0.5 My would have been buffered during transport, since sediment transfer time in the plain are less than 10 ky (Lupker et al., 2012a). The difference between the Valmiki Section and the Bengal Fan may rather arise from the distribution of ice cover in Central and East Himalayas. Presently, the Narayani Catchment has the most extended glacial cover of all major southern-facing Himalayan catchments (Raup et al., 2007), twice that of the Karnali Catchment, and four times that of the Ganga Catchment upstream Rishikesh, at the range outlet. We suppose that the northern flanks of the Himalayas in South Tibet produce an even smaller glacial contribution to the erosion flux. Drained by the Yarlung Tsangpo or Upper Brahmaputra River, this region is arid. This implies smaller glacial advances at the LGM than along the southern flanks (Shi, 2002; Gayer et al., 2006), and lower ice flow velocities and hence subglacial erosion efficiency. The Narayani Catchment may therefore have an increased sensitivity to glacial erosion during glacial advances compared to the entire Ganga-Brahmaputra Catchment.

5.4.2. Comparison with in-situ thermochronology.

We compare our results with in-situ thermochronology published for the Narayani Catchment, in terms of spatial and temporal variations. However, in-situ thermochronology is interpreted as local paleoerosion rates whereas our cosmogenic dataset for Valmiki Section averages paleoerosion rates over the whole Narayani Catchment.

We can spatially refine our interpretation of paleoerosion by dividing the Narayani Catchment into two lithologic domains, the Lesser (LH) and the Higher Himalayas (HH), which occupy 42 and 58% of the modern catchment, respectively. From our Sr-Nd isotopic results, the Narayani River has been exporting 70% of HH sediment on average since the Late Miocene (Fig. 11). The modern carbonate flux represents 10% of the sedimentary load and mainly from the TSS (Morin et al., 2018). Based on these ratios and assuming outcropping areas steady over time, the global ^{10}Be paleoerosion rate of 2 mm/y corresponds to average paleoerosion rates of 1.3 and 2.5 mm/y in the LH and the HH. These differentiated erosion rates are consistent with modern erosion rates based on contrasted ^{10}Be concentrations in modern sediment of the two domains (Niemi et al., 2005; Godard et al., 2012; Godard et al., 2014; Puchol et al., 2014). Additionally, within the HH, the modern distribution of erosion rates indicates that the southern flank of the High Himalayas, exposed to heavy monsoonal precipitation, experiences higher erosion rates than the northern flank (Lavé and Avouac, 2001; Garzanti et al., 2007). We therefore assume that erosion rates along the southern flank of the geographic HH stayed above 3 mm/y during the Late Cenozoic.

Paleoerosion rates were derived for the Late Cenozoic (<1 Ma for the HH domain) from low temperature thermochronologic data, more precisely from (U,Th)/He and fission tracks in apatites. Those paleoerosion rates amount to 0.3 to 1 mm/y in the geographic LH (the frontal Himalayan area of low elevation which dominantly contains LH units but also can contain other units), and are much higher in the geographic HH, up to 2-4 mm/y (Burbank et al., 2003; Blythe et al., 2007; Whipp et al., 2007; Herman et al., 2010; Robert et al., 2009; Nadin et Martin, 2012). The si-situ thermochronology paleoerosion rates are consistent with our ^{10}Be-derived paleoerosion rates, in terms of absolute amount and regional distribution, even though at second order, the thermochronologic paleoerosion rates are somewhat lower in the LH than our ^{10}Be paleoerosion rates.

In parallel, the time variations of the thermochronology paleoerosion rates have been debated. Inversion of multithermochronometers using 1-D (Thiede and Ehlers, 2013) or 3-D (Herman et al., 2010) thermal models suggests that erosion rates would have remained roughly steady throughout the Late Cenozoic. Contrastingly, inversions applied to a large dataset (Herman et al., 2013) or to single vertical profiles in the HHC (Huntington et al., 2006; Blythe et al., 2007) indicate an increase in erosion rates by a factor two to five, between ~3 and 0.9 Ma.

Our results do show an erosion rate increase in the early Quaternary that might partly support the conclusions of these latter studies. An increase in erosion rates of ~35% in the early Quaternary would be limited to the geographic HH if it has been resulted from glacial and periglacial erosion. Given that the area affected by glacial and periglacial erosion during glacial times, mostly in the geographic HH, represents less than 40% of the Narayani Catchment, such an increase in the mean rate could correspond to an increase by a factor two (from 2.5 to 4-5 mm/y) of the High Range erosion rates.

Although this estimate is partly consistent with thermochronology studies carried out in the HHC of the Narayani Catchment (Huntington et al., 2006; Blythe et al., 2007), it differs in several ways. First, the ^{10}Be paleoerosion rates increase is only temporary during the early Quaternary. Second, the thermochronology studies propose 0.5 to 1.5 mm/y paleoerosion rates in the HHC during the Pliocene, which is much lower than our ^{10}Be paleoerosion rates in the HHC during the period. Third, these studies sampled the age-elevation thermochronologic transects along ridges that were not glaciated during the LGM, so glacial erosion is not expected to have contributed to erosion.

To summarize, if our data do not support a twofold increase in erosion rates in the late Cenozoic, it is not because recent rates seen by thermochronology would be overestimated (Schildgen et al., 2018), but rather because older thermochronologic paleoerosion rates in the Pliocene are underestimated compared to our ^{10}Be results.

8. Conclusion.

We designed this work to challenge the absence, previously observed in the Bengal Fan sediment record (Lenard et al., 2020), of a permanent increase in erosion rates in the Himalayas despite global cooling and extended glaciations throughout the late Cenozoic. To this aim, we documented a new composite section thick of 4,000 m across the Siwalik sedimentary record in the Valmiki Tiger Reserve, Bihar, India. The Section is in the north-south axis of the alluvial megafan of the Narayani River, a major transverse river of Central Himalayas. Combining our observations to paleomagnetism, major element and Sr-Nd isotopic geochemistry, ^{10}Be and ^{36}Cl TCN measurements, we obtain the following major conclusions.

(1) The Valmiki Section covers a period extending from 8.2 to ca. 0.7-0.4 Ma, during the Late Cenozoic. There, because the Siwalik folds developed 30 km south of the High Himalayan Front, which is farther from the front than elsewhere in the Siwaliks, most of the section is made up of fine-grained sediments, which are suitable for paleomagnetism studies. During this period, the sedimentation rate in the Ganga plain remained relatively steady at 0.45-0.5 mm/y.

(2) From 7.5 to 1.25 Ma, the Valmiki Section is a genuine record of erosion over the entire tectonic wedge of the Central Himalayas, and most probably over the catchment of the paleo-Narayani River, a major tributary of the Ganga River, with the relative contributions of the Lesser Himalayas and the High Himalayas (HH = HHC + TSS) remaining steady on average. This new section makes it possible to investigate the links between erosion and climate at the start and during the Quaternary Glaciations in the Central Himalayas. Thus, we consider that the composite Valmiki Section records the erosion of the entire tectonic prism in the Central Himalayas until the most recent time.

(3) From 1.25 Ma to 0.4 Ma, the youngest sedimentary rocks of the Valmiki Section correspond to recycled sediments issued from the erosion of the emergent relief of the frontal Siwalik folds, whereas the Narayani River was diverted westward by these uplifting anticlines.

(4) Our ^{10}Be mean paleoerosion rates, averaged over ~1 Ma intervals, have remained roughly stable since 6.5 Ma, within the range of modern values, at 1.4-2.3 mm/y. For the samples older than 5 Ma, this conclusion should be tempered, since the uncertainties on these average values are high (one-sigma error above 40%), particularly because of the corrections related to the recent exposure contribution.

(5) Superimposed on this first-order stability, we record a transient increase at the beginning of the Quaternary between 2 and 1.5 Ma. This transient increase is not followed by a substantial and permanent increase associated with the Quaternary Glaciations, and ends with a return to average modern or long term erosion rates. We suggest that this temporary increase is caused by enhanced erosion (erosion rates increased by a factor of two) of the High Himalayas by the initial carving of the glacial valleys, and that it might partly explain the erosion rate increase documented by thermochronologic studies in the High Himalaya (Huntington et al., 2006).

Despite this local and transient increase, the four TCN ^{10}Be records of the Himalayas (this study, the Surai Section (Charreau et al., 2021), the Yamuna Section (Mandal et al., 2021), and the Bengal Fan (Lenard et al., 2020)) do not support the hypothesis of a substantial and permanent increase in erosion rates as advanced in published work (Zhang et al., 2001; Herman et al., 2013). On the contrary, our results show that erosion rates were as high in the Pliocene as they are today, with rates above 3 mm/y in the High Himalayas. Apart from a transient response to early glacial development in the Quaternary, steady erosion rates indicate that the erosion of the Himalayan range is controlled by tectonics and by the 5,000-m high topographic step between the South Tibetan Plateau and the Ganga Plain rather than by climate.

Acknowledgments

The Bihar State Forest Department is acknowledged for authorization for working and sampling in the Valmiki Tiger Reserve, National Park and Wildlife Sanctuary. V. Jain and R. Sinha are warmly acknowledged for their assistance in getting these authorizations. The study benefited from fruitful discussions with P.H. Blard on ^{10}Be samples preparation. The teams of CRPG, SARM, CEREGE, IPGP are thanked for their assistance in sample preparation and measurements. The teams of CRPG, SARM and CEREGE are thanked for their assistance in sample preparation and measurements. We particularly thank Pierre Voinchet for his guidance and help on the ESR dating of WVF samples which unfortunately did not give easily exploitable results. The ^{10}Be measurements were performed at the ASTER AMS national facility (CEREGE, Aix en Provence) which is supported by the INSU/CNRS, the ANR through the "Projets thématiques d'excellence" program for the "Equipements d'excellence" ASTER-CEREGE action and IRD. The field and analytic works were funded by the ANR Calimero, ANR Himal Fan projects and an INSU Syster project. S. Lenard PhD funding was provided by a Université de Lorraine-CRPG 3-year PhD fellowship.

All the authors declare the absence of any financial conflict of interest. They also declare the absence of affiliation that have a conflict of interest with the results of this paper.

Author contributions

J.L. and J.C. designed the study. J.L. and A.G. made initial explorations for choosing the section location. J.L., J.C., S.L., A.G., R.K.K., F. S., R.P., G.M. and C.F.L. performed field observations and collected the samples. J.C. and S.L. performed paleomagnetism measurements. S.L., G.A., K.K., Z.F., L.L., and I.S. prepared CRN or isotopic samples, or performed the AMS measurements. J.L., S.L. and J.C. performed the computations. SL., J.L., J.C., and C.F.L. interpreted the results and wrote the manuscript.

References

Adams, B. A., Hodges, K. V., Whipple, K. X., Ehlers, T. A., Van Soest, M. C., & Wartho, J. (2015). Constraints on the tectonic and landscape evolution of the Bhutan Himalaya from thermochronometry. Tectonics, 34(6), 1329-1347. https://doi.org/10.1002/2015tc003853

Amidon, W. H., Fisher, G. B., Burbank, D. W., Ciccioli, P. L., Alonso, R. N., Gorin, A. L., Christoffersen, M. S. (2017). Mio-Pliocene aridity in the south-central Andes associated with Southern Hemisphere cold periods. Proceedings of the National Academy of Sciences, 114(25), 6474-6479. https://doi.org/10.1073/pnas.170032711

Andermann, C., Bonnet, S., Gloaguen, R. (2011). Evaluation of precipitation data sets along the Himalayan front. Geochemistry, Geophysics, Geosystems 12. https://doi.org/10.1029/2011gc003513

Andermann, C., Crave, A., Gloaguen, R., Davy, P., Bonnet, S. (2012). Connecting source and transport: Suspended sediments in the Nepal Himalayas. Earth and Planetary Science Letters 351-352, 158-170. https://doi.org/10.1016/j.epsl.2012.06.059

Appel, E., Rösler, W., Corvinus, G. (1991). Magnetostratigraphy of the Miocene-Pleistocene Surai Khola Siwaliks in West Nepal. Geophysical Journal International 105, 191-198. https://doi.org/10.1111/j.1365-246X.1991.tb03455.x

Arnold, M., Merchel, S., Bourlès, D.L., Braucher, R., Benedetti, L., Finkel, R.C., Aumaître, G., Gottdang, A., Klein, M. (2010). The French accelerator mass spectrometry facility ASTER: Improved performance and developments. Nuclear Instruments and Methods in Physics Research Section B: Beam Interactions with Materials and Atoms 268, 1954-1959. https://doi.org/10.1016/j.nimb.2010.02.107

Arnold, M., Aumaître, G., Bourlès, D. L., Keddadouche, K., Braucher, R., Finkel, R. C. et al. (2013). The French accelerator mass spectrometry facility ASTER after 4 years: Status and recent developments on 36Cl and 129I. Nuclear Instruments and Methods in Physics Research Section B: Beam Interactions with Materials and Atoms, 294, 24-28. https://doi.org/10.1016/j. nimb.2012.01.049

Asahi, K. (2010). Equilibrium-line altitudes of the present and Last Glacial Maximum in the eastern Nepal Himalayas and their implications for SW monsoon climate. Quaternary International, 212(1), 26-34. https://doi.org/10.1016/j.quaint.2008.08.004

Attal, M., Lavé, J. (2006). Changes of bedload characteristics along the Marsyandi river (Central Nepal): Implications for understanding hillslope sediment supply, sediment load evolution along fluvial networks, and denudation in active orogenic belts. Geological Society of America Special Papers, 398, 143-171. https://doi.org/10.1130/2006.2398(09)

Baldwin, B., Butler, C.O. (1985). Compaction Curves. AAPG Bulletin 69, 622-626.

Banerjee, A., & Wani, B. A. (2018). Exponentially decreasing erosion rates protect the high-elevation crests of the Himalaya. Earth and Planetary Science Letters, 497, 22-28. https://doi.org/10.1016/j.epsl.2018.06.001

Bernet, M., van der Beek, P., Pik, R., Huyghe, P., Mugnier, J.-L., Labrin, E., Szulc, A. (2006). Miocene to Recent exhumation of the central Himalaya determined from combined detrital zircon fission-track and U/Pb analysis of Siwalik sediments, western Nepal. Basin Research 18, 393-412. https://doi.org/10.1111/j.1365-2117.2006.00303.x

Blythe, A.E., Burbank, D.W., Carter, A., Schmidt, K., Putkonen, J. (2007). Plio-Quaternary exhumation history of the central Nepalese Himalaya: 1. Apatite and zircon fission track and apatite [U-Th]/He analyses. Tectonics 26. https://doi.org/10.1029/2006TC001990

Bollinger, L., Avouac, J. P., Beyssac, O., Catlos, E. J., Harrison, T. M., Grove, M., Goffé, B., Sapkota, S. (2004). Thermal structure and exhumation history of the Lesser Himalaya in central Nepal. Tectonics, 23(5). https://doi.org/10.1029/2003TC001564

Bonnet, S. (2009). Shrinking and splitting of drainage basins in orogenic landscapes from the migration of the main drainage divide. Nature Geoscience, 2(11), 766-771. https://doi.org/10.1038/ngeo666

Braucher, R., Merchel, S., Borgomano, J., Bourlès, D.L. (2011). Production of cosmogenic radionuclides at great depth: A multi element approach. Earth and Planetary Science Letters 309, 1-9. https://doi.org/10.1016/j.epsl.2011.06.036

Braucher, R., Guillou, V., Bourlès, D.L., Arnold, M., Aumaître, G., Keddadouche, K., Nottoli, E. (2015). Preparation of ASTER in-house 10Be/9Be standard solutions. Nuclear Instruments and Methods in Physics Research Section B: Beam Interactions with Materials and Atoms 361, 335-340. https://doi.org/10.1016/j.nimb.2015.06.012

Brown, E.T., Stallard, R.F., Larsen, M.C., Raisbeck, G.M., Yiou, F. (1995). Denudation rates determined from the accumulation of in situ-produced 10Be in the luquillo experimental forest, Puerto Rico. Earth and Planetary Science Letters 129, 193-202. https://doi.org/10.1016/0012-821X(94)00249-X

Burbank, D. W., Blythe, A. E., Putkonen, J., Pratt-Sitaula, B., Gabet, E., Oskin, M., Barros, A., Ojha, T. P. (2003). Decoupling of erosion and precipitation in the Himalayas. Nature, 426(6967), 652-655. https://doi.org/10.1038/nature02187

Carignan, J., Hild, P., Mevelle, G., Morel, J., Yeghicheyan, D. (2001). Routine Analyses of Trace Elements in Geological Samples using Flow Injection and Low Pressure On-Line Liquid Chromatography Coupled to ICP-MS: A Study of Geochemical Reference Materials BR, DR-N, UB-N, AN-G and GH. Geostandards Newsletter 25, 187-198. https://doi.org/10.1111/j.1751-908X.2001.tb00595.x

Caves Rugenstein, J.K., Chamberlain, C.P. (2018). The evolution of hydroclimate in Asia over the Cenozoic: A stable-isotope perspective. Earth-Science Reviews 185, 1129-1156. https://doi.org/10.1016/j.earscirev.2018.09.003

Cerling, T.E., Harris, J.M., MacFadden, B.J., Leakey, M.G., Quade, J., Eisenmann, V., Ehleringer, J.R. (1997). Global vegetation change through the Miocene/Pliocene boundary. Nature 389, 153-158. https://doi.org/10.1038/38229

Charreau, J., Blard, P. H., Puchol, N., Avouac, J. P., Lallier-Vergès, E., Bourlès, D. L., Braucher, R., Gallaud, A., Finkel, R., Jolivet, M., Chen, Y., Roy, P. (2011). Paleo-erosion rates in Central Asia since 9 Ma: A transient increase at the onset of Quaternary glaciations?. Earth and Planetary Science Letters, 304(1-2), 85-92. https://doi.org/10.1016/j.epsl.2011.01.018

Charreau, J., Blard, P.-H., Zumaque, J., Martin, L.C.P., Delobel, T., Szafran, L. (2019). Basinga: A cell-by-cell GIS toolbox for computing basin average scaling factors, cosmogenic production rates and denudation rates. Earth Surface Processes and Landforms, 44(12), 2349-2365. https://doi.org/10.1002/esp.4649

Charreau, J., Lavé, J., France-Lanord, C., Puchol, N., Blard, P. H., Pik, R., Gajurel,A.P., ASTER Team. (2021). A 6 Ma record of palaeodenudation in the central Himalayas from in situ cosmogenic 10Be in the Surai section. Basin Research, 33(2), 1218-1239. https://doi.org/10.1111/bre.12511

Chmeleff, J., von Blanckenburg, F., Kossert, K., Jakob, D. (2010). Determination of the 10Be half-life by multicollector ICP-MS and liquid scintillation counting. Nuclear Instruments and Methods in Physics Research Section B: Beam Interactions with Materials and Atoms 268, 192-199. https://doi.org/10.1016/j.nimb.2009.09.012

Clift, P.D. (2006). Controls on the erosion of Cenozoic Asia and the flux of clastic sediment to the ocean. Earth and Planetary Science Letters 241, 571-580. https://doi.org/10.1016/j.epsl.2005.11.028

Colchen, M., Mascle, G., Van Haver, T. (1986). Some aspects of collision tectonics in the Indus suture zone, Ladakh. Geological Society, London, Special Publications, 19(1), 173-184. https://doi.org/10.1144/gsl.sp.1986.019.01.09

Corvinus, G., Rimal, L.N. (2001). Biostratigraphy and geology of the neogene Siwalik group of the Surai Khola and Rato Khola areas in Nepal. Palaeogeography, Palaeoclimatology, Palaeoecology 165, 251-279. https://doi.org/10.1016/S0031-0182(00)00163-2

Cramer, B. S., Miller, K. G., Barrett, P. J., Wright, J. D. (2011). Late Cretaceous-Neogene trends in deep ocean temperature and continental ice volume: Reconciling records of benthic foraminiferal geochemistry (δ18O and Mg/Ca) with sea level history. Journal of Geophysical Research: Oceans, 116(C12). https://doi.org/10.1029/2011jc007255

DeCelles, P.G., Gehrels, G.E., Quade, J., Ojha, T.P., Kapp, P.A., Upreti, B.N. (1998). Neogene foreland basin deposits, erosional unroofing, and the kinematic history of the Himalayan fold-thrust belt, western Nepal. Geological Society of America Bulletin 110, 2-21. https://doi.org/10.1130/0016-7606(1998)110<0002:NFBDEU>2.3.CO;2

DiBiase, R.A. (2018). Short Communication: Increasing vertical attenuation length of cosmogenic nuclide production on steep slopes negates topographic shielding corrections for catchment erosion rates. Earth Surface Dynamics Discussions 1-17. https://doi.org/10.5194/esurf-2018-48

Dingle, E. H., Attal, M., Sinclair, H. D. (2017). Abrasion-set limits on Himalayan gravel flux. Nature, 544(7651), 471-474. https://doi.org/10.1038/nature22039

Dingle, E.H., Sinclair, H.D., Attal, M., Rodés, Á., Singh, V. (2018). Temporal variability in detrital 10Be concentrations in a large Himalayan catchment. Earth Surface Dynamics 6, 611-635. https://doi.org/10.5194/esurf-6-611-2018

Divyadarshini, A., Singh, V. (2019). Investigating topographic metrics to decipher structural model and morphotectonic evolution of the Frontal Siwalik Ranges, Central Himalaya, Nepal. Geomorphology 337, 31-52. https://doi.org/10.1016/j.geomorph.2019.03.028

Dubille, M. (2008). Transport solide et abrasion dans les rivières à fond rocheux. De la mesure au modèle sur un exemple himalayen. Universite de Grenoble 1.

Dubille, M., Lavé, J. (2015). Rapid grain size coarsening at sandstone/conglomerate transition: similar expression in Himalayan modern rivers and Pliocene molasse deposits. Basin Research 27, 26-42. https://doi.org/10.1111/bre.12071

Edwards, E.J., Osborne, C.P., Stromberg, C.A.E., Smith, S.A., C4 Grasses Consortium, Bond, W.J., Christin, P.A., Cousins, A.B., Duvall, M.R., Fox, D.L., Freckleton, R.P., Ghannoum, O., Hartwell, J., Huang, Y., Janis, C.M., Keeley, J.E., Kellogg, E.A., Knapp, A.K., Leakey, A.D.B., Nelson, D.M., Saarela, J.M., Sage, R.F., Sala, O.E., Salamin, N., Still, C.J., Tipple, B. (2010). The Origins of C4 Grasslands: Integrating Evolutionary and Ecosystem Science. Science 328, 587-591. https://doi.org/10.1126/science.1177216

Gabet, E.J., Pratt-Sitaula, B.A., Burbank, D.W. (2004). Climatic controls on hillslope angle and relief in the Himalayas. Geol 32, 629. https://doi.org/10.1130/G20641.1

Gabet, E. J., Burbank, D. W., Pratt-Sitaula, B., Putkonen, J., Bookhagen, B. (2008). Modern erosion rates in the High Himalayas of Nepal. Earth and Planetary Science Letters, 267(3-4), 482-494. https://doi.org/10.1016/j.epsl.2007.11.059

Gallo, F., Lavé, J. (2014). Evolution of a large landslide in the High Himalaya of central Nepal during the last half-century. Geomorphology 223, 20-32. https://doi.org/10.1016/j.geomorph.2014.06.021

Galy, A., France-Lanord, C. (2001). Higher erosion rates in the Himalaya: Geochemical constraints on riverine fluxes. Geology 29, 23-26. https://doi.org/10.1130/0091-7613(2001)029<0023:HERITH>2.0.CO;2

Garzanti, E., Vezzoli, G., Andò, S., Lavé, J., Attal, M., France-Lanord, C., DeCelles, P. (2007). Quantifying sand provenance and erosion (Marsyandi river, Nepal Himalaya). Earth and Planetary Science Letters, 258(3-4), 500-515. https://doi.org/10.1016/j.epsl.2007.04.010

Garzione, C.N., Dettman, D.L., Quade, J., DeCelles, P.G., Butler, R.F. (2000). High times on the Tibetan Plateau: Paleoelevation of the Thakkhola graben, Nepal. Geology 28, 339-342. https://doi.org/10.1130/0091-7613(2000)028<0339:htottp>2.3.co;2

Gautam, P., Fujiwara, Y. (2000). Magnetic polarity stratigraphy of Siwalik Group sediments of Karnali River section in western Nepal. Geophysical Journal International 142, 812-824. https://doi.org/10.1046/j.1365-246x.2000.00185.x

Gautam, P., & Rösler, W. (1999). Depositional chronology and fabric of Siwalik Group sediments in central Nepal from magnetostratigraphy and magnetic anisotropy. Journal of Asian Earth Sciences, 17(5-6), 659-682. https://doi.org/10.1016/s1367-9120(99)00021-8

Gayer, E., Lavé, J., Pik, R., France-Lanord, C. (2006). Monsoonal forcing of Holocene glacier fluctuations in Ganesh Himal (Central Nepal) constrained by cosmogenic 3He exposure ages of garnets. Earth and Planetary Science Letters, 252(3-4), 275-288. https://doi.org/10.1016/j.epsl.2006.09.040

Gébelin, A., Mulch, A., Teyssier, C., Jessup, M.J., Law, R.D., Brunel, M. (2013). The Miocene elevation of Mount Everest. Geology 41, 799-802. https://doi.org/10.1130/G34331.1

Godard, V., Burbank, D. W., Bourlès, D. L., Bookhagen, B., Braucher, R., Fisher, G. B. (2012). Impact of glacial erosion on 10Be concentrations in fluvial sediments of the Marsyandi catchment, central Nepal. Journal of Geophysical Research: Earth Surface, 117(F3). https://doi.org/10.1029/2011jf002230

Godard, V., Bourlès, D. L., Spinabella, F., Burbank, D. W., Bookhagen, B., Fisher, G. B., Moulin, A., Léanni, L. (2014). Dominance of tectonics over climate in Himalayan denudation. Geology, 42(3), 243-246. https://doi.org/10.1130/g35342.1

Grandin, R., Doin, M. P., Bollinger, L., Pinel-Puysségur, B., Ducret, G., Jolivet, R., Sapkota, S. N. (2012). Long-term growth of the Himalaya inferred from interseismic InSAR measurement. Geology, 40(12), 1059-1062.

Gupta, A.K., Yuvaraja, A., Prakasam, M., Clemens, S.C., Velu, A. (2015). Evolution of the South Asian monsoon wind system since the late Middle Miocene. Palaeogeography, Palaeoclimatology, Palaeoecology 438, 160-167. https://doi.org/10.1016/j.palaeo.2015.08.006

Hallet, B., Hunter, L., Bogen, J. (1996). Rates of erosion and sediment evacuation by glaciers: a review of field data and their implications. Global Planet. Change 12, 213-235. https://doi.org/10.1016/0921-8181(95)00021-6

Harrison, T.M., Copeland, P., Hall, S.A., Quade, J., Burner, S., Ojha, T.P., Kidd, W.S.F. (1993). Isotopic preservation of Himalayan/Tibetan uplift, denudation, and climatic histories of two molasse deposits. The Journal of Geology 101, 157-175. https://doi.org/10.1086/648214

Hein, C.J., Galy, V., Galy, A., France-Lanord, C., Kudrass, H., Schwenk, T. (2017). Post-glacial climate forcing of surface processes in the Ganges-Brahmaputra river basin and implications for carbon sequestration. Earth and Planetary Science Letters 478, 89-101. https://doi.org/10.1016/j.epsl.2017.08.013

Hérail, G., & Mascle, G. (1980). Les Siwaliks du Népal central: Structure et géomorphologie d'un piédmont en cours de déformation (The central nepalese siwaliks: structure and geomorphology of an upheaveling piedmont). Bulletin de l'Association de géographes français, 57(470), 259-267.

Herbert, T. D., Lawrence, K. T., Tzanova, A., Peterson, L. C., Caballero-Gill, R., Kelly, C. S. (2016). Late Miocene global cooling and the rise of modern ecosystems. Nature Geoscience, 9(11), 843-847. https://doi.org/10.1038/ngeo2813

Herman, F., Copeland, P., Avouac, J.-P., Bollinger, L., Mahéo, G., Le Fort, P., Rai, S., Foster, D., Pêcher, A., Stüwe, K., Henry, P. (2010). Exhumation, crustal deformation, and thermal structure of the Nepal Himalaya derived from the inversion of thermochronological and thermobarometric data and modeling of the topography. J. Geophys. Res. 115, B06407. https://doi.org/10.1029/2008JB006126

Herman, F., Seward, D., Valla, P.G., Carter, A., Kohn, B., Willett, S.D., Ehlers, T.A. (2013). Worldwide acceleration of mountain erosion under a cooling climate. Nature 504, 423-426. https://doi.org/10.1038/nature12877

Hilley, G. E., & Strecker, M. R. (2004). Steady state erosion of critical Coulomb wedges with applications to Taiwan and the Himalaya. Journal of Geophysical Research: Solid Earth, 109(B1). https://doi.org/10.1029/2002jb002284

Hodges, K. V., Wobus, C., Ruhl, K., Schildgen, T., Whipple, K. (2004). Quaternary deformation, river steepening, and heavy precipitation at the front of the Higher Himalayan ranges. Earth and Planetary science letters, 220(3-4), 379-389. https://doi.org/10.1016/s0012-821x(04)00063-9

Huntington, K.W., Blythe, A.E., Hodges, K.V. (2006). Climate change and Late Pliocene acceleration of erosion in the Himalaya. Earth and Planetary Science Letters 252, 107-118. https://doi.org/10.1016/j.epsl.2006.09.031

Huyghe, P., Galy, A., Mugnier, J.-L., France-Lanord, C. (2001). Propagation of the thrust system and erosion in the Lesser Himalaya: Geochemical and sedimentological evidence. Geology 29, 1007. https://doi.org/10.1130/0091-7613(2001)029<1007:POTTSA>2.0.CO;2

Jain, V., & Sinha, R. (2003). River systems in the Gangetic plains and their comparison with the Siwaliks: A review. Current Science, 1025-1033. https://doi.org/10.1111/j.1365-3091.1994.tb01426.x

Kapannusch, R., Scherler, D., King, G., Wittmann, H. (2020). Glacial influence on late Pleistocene 10Be-derived paleo-erosion rates in the north-western Himalaya, India. Earth and Planetary Science Letters, 547, 116441. https://doi.org/10.1016/j.epsl.2020.116441

Korschinek, G., Bergmaier, A., Faestermann, T., Gerstmann, U.C., Knie, K., Rugel, G., Wallner, A., Dillmann, I., Dollinger, G., von Gostomski, Ch.L., Kossert, K., Maiti, M., Poutivtsev, M., Remmert, A. (2010). A new value for the half-life of 10Be by Heavy-Ion Elastic Recoil Detection and liquid scintillation counting. Nuclear Instruments and Methods in Physics Research Section B: Beam Interactions with Materials and Atoms 268, 187-191. https://doi.org/10.1016/j.nimb.2009.09.020

Lal, D. (1991). Cosmic ray labeling of erosion surfaces: in situ nuclide production rates and erosion models. Earth and Planetary Science Letters 104, 424-439. https://doi.org/10.1016/0012-821X(91)90220-C

Lallier, F., Antoine, C., Charreau, J., Caumon, G., Ruiu, J. (2013). Management of ambiguities in magnetostratigraphic correlation. Earth and Planetary Science Letters 371-372, 26-36. https://doi.org/10.1016/j.epsl.2013.04.019

Lauer, J., Willenbring, J. (2010). Steady state reach-scale theory for radioactive tracer concentration in a simple channel/floodplain system. Journal of Geophysical Research: Earth Surface 115, F04018. https://doi.org/10.1029/2009jf001480

Lavé, J., Avouac, J.P. (2000). Active folding of fluvial terraces across the Siwaliks Hills, Himalayas of central Nepal. J. Geophys. Res. 105, 5735-5770. https://doi.org/10.1029/1999JB900292

Lavé, J., Avouac, J. P. (2001). Fluvial incision and tectonic uplift across the Himalayas of central Nepal. Journal of Geophysical Research: Solid Earth, 106(B11), 26561-26591. https://doi.org/10.1029/2001jb000359

Lavé, J., Guérin, C., Valla, P. G., Guillou, V., Rigaudier, T., Benedetti, L., France-Lanord, C., Gajurel, A., P., Morin, G., Dumoulin, J., P., Christophe Moreau, C., Galy, V. (2023). Medieval demise of a Himalayan giant summit induced by mega-landslide. Nature, 619(7968), 94-101.

Lenard, S.J.P., Lavé, J., France-Lanord, C., Aumaître, G., Bourlès, D.L., Keddadouche, K. (2020). Steady erosion rates in the Himalayas through late Cenozoic climatic changes. Nat. Geosci. 13, 448-452. https://doi.org/10.1038/s41561-020-0585-2

Lenard, S.J.P. (2019). The evolution of the Himalaya since the Late Miocene, as told by the history of its erosion. Université de Lorraine. https://theses.hal.science/tel-02517014/

Lisiecki, L.E., Raymo, M.E. (2005). A Pliocene-Pleistocene stack of 57 globally distributed benthic δ18O records. Paleoceanography 20, PA1003. https://doi.org/10.1029/2004PA001071

Lupker, M., France-Lanord, C., Lavé, J., Bouchez, J., Galy, V., Métivier, F., Gaillardet, J., Lartiges, B., Mugnier, J.-L. (2011). A Rouse-based method to integrate the chemical composition of river sediments: Application to the Ganga basin. Journal of Geophysical Research 116, F04012. https://doi.org/10.1029/2010JF001947

Lupker, M., Blard, P.-H., Lavé, J., France-Lanord, C., Leanni, L., Puchol, N., Charreau, J., Bourlès, D., 2012a. 10Be-derived Himalayan denudation rates and sediment budgets in the Ganga basin. Earth and Planetary Science Letters 333-334, 146-156. https://doi.org/10.1016/j.epsl.2012.04.020

Lupker, M., France-Lanord, C., Galy, V., Lavé, J., Gaillardet, J., Gajurel, A.P., Guilmette, C., Rahman, M., Singh, S.K., Sinha, R., 2012b. Predominant floodplain over mountain weathering of Himalayan sediments (Ganga basin). Geochimica et Cosmochimica Acta 84, 410-432. https://doi.org/10.1016/j.gca.2012.02.001

Lupker, M., France-Lanord, C., Galy, V., Lavé, J., Kudrass, H. (2013). Increasing chemical weathering in the Himalayan system since the Last Glacial Maximum. Earth and Planetary Science Letters 365, 243-252. https://doi.org/10.1016/j.epsl.2013.01.038

Lyon-Caen, H., Molnar, P. (1985). Gravity anomalies, flexure of the Indian Plate, and the structure, support and evolution of the Himalaya and Ganga Basin. Tectonics 4, 513-538. https://doi.org/10.1029/TC004i006p00513

Mandal, S. K., Scherler, D., & Wittmann, H. (2021). Tectonic accretion controls erosional cyclicity in the Himalaya. AGU Advances, 2(3), e2021AV000487.

Marc, O., Behling, R., Andermann, C., Turowski, J. M., Illien, L., Roessner, S., & Hovius, N. (2019). Long-term erosion of the Nepal Himalayas by bedrock landsliding: the role of monsoons, earthquakes and giant landslides. Earth Surface Dynamics, 7(1), 107-128. https://doi.org/10.5194/esurf-7-107-2019

Mariotti, A., Blard, P. H., Charreau, J., Toucanne, S., Jorry, S. J., Molliex, S., Bourlès, D. L., Aumaître, G., Keddadouche, K., 2021. Nonlinear forcing of climate on mountain denudation during glaciations. Nature Geoscience, 14(1), 16-22. https://doi.org/10.1038/s41561-020-00672-2

Martin, L.C.P., Blard, P.-H., Balco, G., Lavé, J., Delunel, R., Lifton, N., Laurent, V. (2017). The CREp program and the ICE-D production rate calibration database: A fully parameterizable and updated online tool to compute cosmic-ray exposure ages. Quaternary Geochronology 38, 25-49. https://doi.org/10.1016/j.quageo.2016.11.006

Métivier, F., Gaudemer, Y., Tapponnier, P., Klein, M. (1999). Mass accumulation rates in Asia during the Cenozoic. Geophys. J. Int. 137, 280-318. https://doi.org/10.1046/j.1365-246X.1999.00802.x

Milliman, J. D., Farnsworth, K. L. (2011). River discharge to the coastal ocean: a global synthesis. Cambridge University. https://doi.org/10.1017/CBO9780511781247

Molnar, P. (2004). Late Cenozoic increase in accumulation rates of terrestrial sediment: How might climate change have affected erosion rates?. Annual Review of Earth and Planetary Sciences, 32, 67-89. https://doi.org/10.1146/annurev.earth.32.091003.143456

Morin, G.P., Lavé, J., France-Lanord, C., Rigaudier, T., Gajurel, A.P., Sinha, R. (2018). Annual Sediment Transport Dynamics in the Narayani Basin, Central Nepal: Assessing the Impacts of Erosion Processes in the Annual Sediment Budget. Journal of Geophysical Research: Earth Surface 123, 2341-2376. https://doi.org/10.1029/2017JF004460

Morin, G. (2015). L'Érosion Et L'Alteration Et Leur Évolution Depuis Le Tardi-Pleistocene : Analyse Des Processus D'Érosion A Partir De Sediments De Riviere Actuels Et Passes Au Nepal Central. Université de Lorraine, Nancy, France. https://www.theses.fr/2015LORR0258

Nadin, E.S., Martin, A.J. (2012). Apatite thermochronometry within a knickzone near the Higher Himalaya front, central Nepal: No resolvable fault motion in the past one million years. Tectonics 31. https://doi.org/10.1029/2011TC003000

Najman, Y., Bracciali, L., Parrish, R.R., Chisty, E., Copley, A. (2016). Evolving strain partitioning in the Eastern Himalaya: The growth of the Shillong Plateau. Earth and Planetary Science Letters 433, 1-9. https://doi.org/10.1016/j.epsl.2015.10.017

Niemi, N.A., Oskin, M., Burbank, D.W., Heimsath, A.M., Gabet, E.J. (2005). Effects of bedrock landslides on cosmogenically determined erosion rates. Earth and Planetary Science Letters 237, 480-498. https://doi.org/10.1016/j.epsl.2005.07.009

Ogg, J. G. (2012). Geomagnetic Polarity Time Scale. In F. Gradstein, J. Ogg, M. Schmitz, G. Ogg (Eds.), The Geological Time Scale, p. 1176. Oxford: Elsevier.

Ojha, T.P., Butler, R.F., DeCelles, P.G., Quade, J. (2009). Magnetic polarity stratigraphy of the Neogene foreland basin deposits of Nepal. Basin Research 21, 61-90. https://doi.org/10.1111/j.1365-2117.2008.00374.x

Oskin, M. E., Longinotti, N. E., Peryam, T. C., Dorsey, R. J., DeBoer, C. J., Housen, B. A., Blisniuk, K. D. (2017). Steady 10Be-derived paleoerosion rates across the Plio-Pleistocene climate transition, Fish Creek-Vallecito basin, California. Journal of Geophysical Research: Earth Surface, 122(9), 1653-1677. https://doi.org/10.1002/2016jf004113

Pati, P., Parkash, B., Awasthi, A. K., Acharya, V. (2011). Holocene tectono-geomorphic evolution of parts of the Upper and Middle Gangetic plains, India. Geomorphology, 128(3-4), 148-170. https://doi.org/10.1016/j.geomorph.2011.01.001

Pati, P., Verma, A. K., Dash, C., Patel, N. K., Gupta, A., Sharma, V., Jakhmola, R. P., Parkash, B., Awasthi, A. K., Saraf, A. K. (2019). Influence of neotectonism on geomorphology and depositional architecture of the Gandak megafan, middle Ganga plain, India. Geomorphology, 327, 489-503. https://doi.org/10.1016/j.geomorph.2018.11.029

Pedersen, V. K., Egholm, D. L. (2013). Glaciations in response to climate variations preconditioned by evolving topography. Nature, 493(7431), 206-210. https://doi.org/10.1038/nature11786

Puchol, N., Lavé, J., Lupker, M., Blard, P. H., Gallo, F., France-Lanord, C., ASTER Team (2014). Grain-size dependent concentration of cosmogenic 10Be and erosion dynamics in a landslide-dominated Himalayan watershed. Geomorphology, 224, 55-68. https://doi.org/10.1016/j.geomorph.2014.06.019

Puchol, N., Charreau, J., Blard, P. H., Lavé, J., Dominguez, S., Pik, R., Saint-Carlier, D., ASTER Team (2017). Limited impact of Quaternary glaciations on denudation rates in Central Asia. Bulletin, 129(3-4), 479-499. https://doi.org/10.1130/b31475.1

Putkonen, J. K. (2004). Continuous snow and rain data at 500 to 4400 m altitude near Annapurna, Nepal, 1999-2001. Arctic, Antarctic, and Alpine Research, 36(2), 244-248. https://doi.org/10.1657/1523-0430(2004)036[0244:csarda]2.0.co;2

Quade, J., Cerling, T.E., Bowman, J.R. (1989). Development of Asian monsoon revealed by marked ecological shift during the latest Miocene in northern Pakistan. Nature 342, 163-166. https://doi.org/10.1038/342163a0

Raup, B., Racoviteanu, A., Khalsa, S.J.S., Helm, C., Armstrong, R., Arnaud, Y. (2007). The GLIMS geospatial glacier database: A new tool for studying glacier change. Global and Planetary Change, Climate Change Impacts on Mountain Glaciers and Permafrost 56, 101-110. https://doi.org/10.1016/j.gloplacha.2006.07.018

Rempel, A. W., Marshall, J. A., Roering, J. J. (2016). Modeling relative frost weathering rates at geomorphic scales. Earth and Planetary Science Letters, 453, 87-95. https://doi.org/10.1016/j.epsl.2016.08.019

Robert, X., Van Der Beek, P., Braun, J., Perry, C., Dubille, M., Mugnier, J. L. (2009). Assessing Quaternary reactivation of the Main Central thrust zone (central Nepal Himalaya): New thermochronologic data and numerical modeling. Geology, 37(8), 731-734. https://doi.org/10.1130/g25736a.1

Schaller, M., von Blanckenburg, F., Veldkamp, A., Tebbens, L. A., Hovius, N., Kubik, P. W. (2002). A 30 000 yr record of erosion rates from cosmogenic 10Be in Middle European river terraces. Earth and Planetary Science Letters, 204(1-2), 307-320. https://doi.org/10.1016/s0012-821x(02)00951-2

Scherler, D., Bookhagen, B., Strecker, M.R. (2014). Tectonic control on 10Be-derived erosion rates in the Garhwal Himalaya, India. Journal of Geophysical Research: Earth Surface 119, 83-105. https://doi.org/10.1002/2013JF002955

Schildgen, T.F., van der Beek, P.A., Sinclair, H.D., Thiede, R.C. (2018). Spatial correlation bias in late-Cenozoic erosion histories derived from thermochronology. Nature 559, 89-93. https://doi.org/10.1038/s41586-018-0260-6

Schimmelpfennig, I., Williams, A., Pik, R., Burnard, P., Niedermann, S., Finkel, R., Schneider, B., Benedetti, L. (2011). Inter-comparison of cosmogenic in-situ 3He, 21Ne and 36Cl at low latitude along an altitude transect on the SE slope of Kilimanjaro volcano (3°S, Tanzania). Quaternary Geochronology 6, 425-436. https://doi.org/10.1016/j.quageo.2011.05.002

Schimmelpfennig, I., Blard, P. H., Tesson, J., Zakari, M., Benedetti, L., Balco, G., ... & Lavé, J. (2022). The CREp 36Cl exposure age calculator: development version "dev", https://hal.science/hal-03659255/file/CREp%2036Cl%20dev_final.pdf Sharma, P., Kubik, P.W., Fehn, U., Gove, H.E., Nishiizumi, K., Elmore, D. (1990). Development of 36Cl standards for AMS. Nuclear Instruments and Methods in Physics Research Section B: Beam Interactions with Materials and Atoms 52, 410-415. https://doi.org/10.1016/0168-583X(90)90447-3

Schumer, R., Jerolmack, D. J. (2009). Real and apparent changes in sediment deposition rates through time. Journal of Geophysical Research: Earth Surface, 114(F3). https://doi.org/10.1029/2009jf001266

Shi, Y. (2002). Characteristics of late Quaternary monsoonal glaciation on the Tibetan Plateau and in East Asia. Quaternary International, 97, 79-91. https://doi.org/10.1016/s1040-6182(02)00053-8

Singh, S.K., Rai, S.K., Krishnaswami, S. (2008). Sr and Nd isotopes in river sediments from the Ganga Basin: Sediment provenance and spatial variability in physical erosion. Journal of Geophysical Research 113, F03006. https://doi.org/10.1029/2007JF000909

Sinha, R., Friend, P. F. (1994). River systems and their sediment flux, Indo-Gangetic plains, Northern Bihar, India. Sedimentology, 41(4), 825-845. https://doi.org/10.1111/j.1365-3091.1994.tb01426.x

Stone, J.O. (2000). Air pressure and cosmogenic isotope production. Journal of Geophysical Research: Solid Earth 105, 23753-23759. https://doi.org/10.1029/2000JB900181

Thiede, R.C., Ehlers, T.A. (2013). Large spatial and temporal variations in Himalayan denudation. Earth and Planetary Science Letters 371-372, 278-293. https://doi.org/10.1016/j.epsl.2013.03.004

Tokuoka, T., Takayasu, K., Hisatomi, K. (1990). Stratigraphy and Geologic structures of the Churia (Siwalik) Group in the Tinau Khola#Binai Khola Area, West Central Nepal. Memoirs of the Faculty of Science, Shimane University 71-88.

van der Beek, P., Robert, X., Mugnier, J.-L., Bernet, M., Huyghe, P., Labrin, E. (2006). Late Miocene-recent exhumation of the central Himalaya and recycling in the foreland basin assessed by apatite fission-track thermochronology of Siwalik sediments, Nepal. Basin Research 18, 413-434. https://doi.org/10.1111/j.1365-2117.2006.00305.x

Wang, W., Godard, V., Liu-Zeng, J., Scherler, D., Xu, C., Zhang, J., Xie, K., Bellier, O., Ansberque, C., de Sigoyer, J., ASTER Team (2017). Perturbation of fluvial sediment fluxes following the 2008 Wenchuan earthquake. Earth Surface Processes and Landforms, 42(15), 2611-2622. https://doi.org/10.1002/esp.4210

Weidinger, J. T., Korup, O. (2009). Frictionite as evidence for a large Late Quaternary rockslide near Kanchenjunga, Sikkim Himalayas, India—Implications for extreme events in mountain relief destruction. Geomorphology, 103(1), 57-65. https://doi.org/10.1016/j.geomorph.2007.10.021

Whipp, D.M., Ehlers, T.A., Blythe, A.E., Huntington, K.W., Hodges, K.V., Burbank, D.W. (2007). Plio-Quaternary exhumation history of the central Nepalese Himalaya: 2. Thermokinematic and thermochronometer ####age prediction model. Tectonics 26. https://doi.org/10.1029/2006TC001991

Willenbring, J.K., von Blanckenburg, F. (2010). Long-term stability of global erosion rates and weathering during late-Cenozoic cooling. Nature 465, 211-214. https://doi.org/10.1038/nature09044

Wobus, C.W., Hodges, K.V., Whipple, K.X. (2003). Has focused denudation sustained active thrusting at the Himalayan topographic front? Geology 31, 861-864. https://doi.org/10.1130/g19730.1

Yang, Y., Galy, A., Fang, X., Yang, R., Zhang, W., Zan, J. (2017). Eolian dust forcing of river chemistry on the northeastern Tibetan Plateau since 8 Ma. Earth and Planetary Science Letters 464, 200-210. https://doi.org/10.1016/j.epsl.2017.02.009

Yanites, B.J., Tucker, G.E., Anderson, R.S. (2009). Numerical and analytical models of cosmogenic radionuclide dynamics in landslide-dominated drainage basins. Journal of Geophysical Research: Earth Surface 114. https://doi.org/10.1029/2008JF001088

Zhang, P.Z., Molnar, P., Downs, W.R. (2001). Increased sedimentation rates and grain sizes 2-4 Myr ago due to the influence of climate change on erosion rates. Nature 410, 891-897. https://doi.org/10.1038/35073504

Zijderveld, J. D. A. (1967). A.C. demagnetization of rocks: Analysis of results. In D. W. Collinson, K. M. Creer, S. K. Runcorn (Eds.), Methods in paleomagnetism (pp. 254-286).